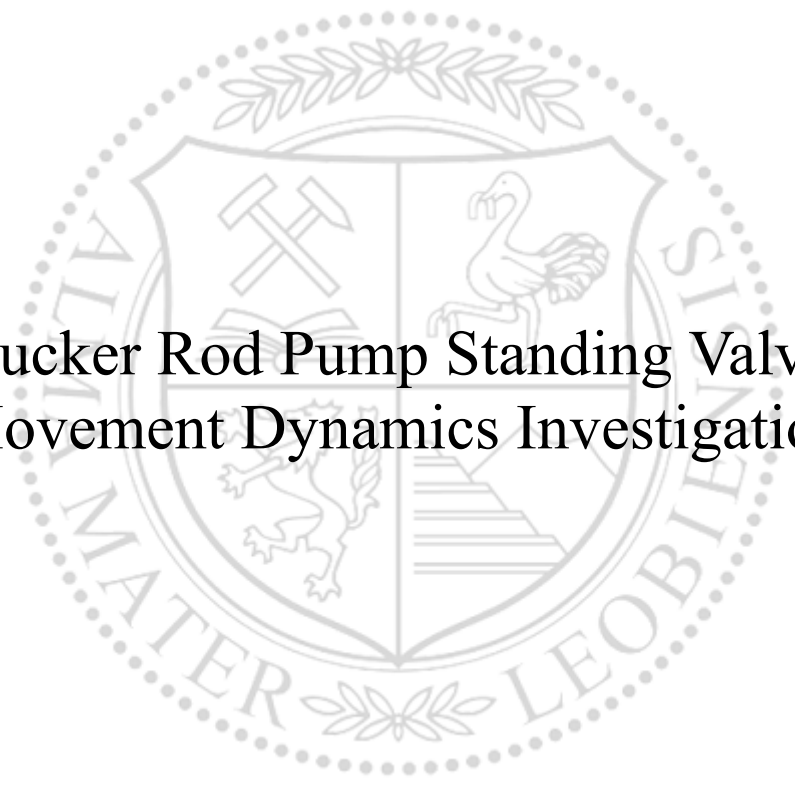




Chair of Petroleum and Geothermal Energy Recovery

Master's Thesis



Sucker Rod Pump Standing Valve
Movement Dynamics Investigation

Jörg Peroutka, BSc

May 2022



EIDESSTÄTLICHE ERKLÄRUNG

Ich erkläre an Eides statt, dass ich diese Arbeit selbständig verfasst, andere als die angegebenen Quellen und Hilfsmittel nicht benutzt, und mich auch sonst keiner unerlaubten Hilfsmittel bedient habe.

Ich erkläre, dass ich die Richtlinien des Senats der Montanuniversität Leoben zu "Gute wissenschaftliche Praxis" gelesen, verstanden und befolgt habe.

Weiters erkläre ich, dass die elektronische und gedruckte Version der eingereichten wissenschaftlichen Abschlussarbeit formal und inhaltlich identisch sind.

Datum 12.05.2022

Unterschrift Verfasser/in
Jörg Peroutka

Jörg Peroutka, BSc
Master Thesis 2022
Petroleum Engineering

Sucker Rod Pump Standing Valve Movement Dynamics Investigation

Supervisor: Dipl.-Ing. Ramzy Albishini
Co-supervisor: Dipl.-Ing. Dipl.-Ing. Dr.mont.
Clemens Langbauer

Chair of Petroleum and Geothermal Energy
Recovery

Acknowledgements

I am very grateful to my supervisor, Dipl.-Ing. Ramzy Albishini, for his guidance, patience, and continued support throughout my thesis.

I would like to extend my thanks to Dipl.-Ing. Dipl.-Ing. Dr. mont. Clemens Langbauer for his valuable suggestions and advice.

Special thanks to Ing. Andreas Öfler for his technical support at the Pump Test Facility Leoben.

Lastly, I'd like to thank my family, especially my parents, Gerlinde and Roderich, and my brothers, Jochen and Martin, for their continued support, and for keeping me motivated during my studies.

Abstract

Sucker rod pumps are among the oldest and most widely used artificial lift systems. They are well understood by the field personnel and are relatively simple to operate. However, the exact behavior of the downhole components is hard to predict and mostly relies on approximations due to dynamometer data gathered at the surface. The surface data is then converted in such matter that it's applicable in predicting the component's downhole movement. The difference between surface and downhole movement is due to the elongation of the sucker rod string. This can lead to misinterpretations and ultimately, decreases the efficiency of such an artificial lift system, resulting in high operating costs or early technical failure. Technical failures necessitate a workover which is time-consuming and expensive.

This thesis aims to improve the knowledge of the actual downhole behavior of the sucker rod pump standing valve in particular, by utilizing a specially designed transparent Plexiglass valve cage. All tests are conducted at the Pump Test Facility at the University of Leoben. The test setup enables the visual depiction of the ball movement of the check valve, and the utilization of a pair of inductive sensors to measure the exact position of the ball during pumping cycles at any time. This setup also enables the observation of phenomena associated with a sucker rod pump standing valve. One of the main findings is mid-cycle valve closing which can lead to fast deterioration of the valve ball and seat.

The data gathered from the experiments are then used to verify a Coupled-Valve Sucker Rod Pump simulation model provided by the company AC2T research GmbH. The model is capable of capturing the behavior of the test rig by using a correction or calibration factor. In addition, the simulation model can easily be adjusted to different valve cage geometries and can verify the square-root dependency of the critical plunger speed on the ball density.

Zusammenfassung

Gestängetiefpumpen gehören zu den ältesten und am häufigsten verwendeten künstlichen Fördersystem für Erdöl- und Erdgasbohrungen. Sie werden von den Mitarbeitern vor Ort gut verstanden und sind relativ einfach zu bedienen. Das genaue Verhalten der Komponenten im Bohrloch lässt sich jedoch nur schwer vorhersagen und beruht meist auf Näherungswerten, die anhand von an der Oberfläche erfassten Dynamometerdaten ermittelt werden. Die Oberflächendaten werden dann so umgewandelt, dass sie für die Vorhersage der Bewegung der Komponente im Bohrloch geeignet sind. Der Unterschied zwischen der Bewegung an der Oberfläche und der Bewegung im Bohrloch ist auf die Dehnung des Pumpgestänges zurückzuführen. Dies kann zu Fehlinterpretationen führen und letztlich die Effizienz eines solchen künstlichen Fördersystems verringern, was zu hohen Betriebskosten oder frühzeitigem technischen Versagen führt. Technische Ausfälle machen eine zeitaufwändige und teure Aufwältigung erforderlich.

Ziel dieser Arbeit ist es, die Kenntnisse über das tatsächliche Verhalten des Ventils der Pumpe im Bohrloch zu verbessern, indem ein speziell entwickelter transparenter Plexiglas-Ventilkäfig verwendet wird. Alle Versuche werden in der Pumpentestanlage der Montanuniversität Leoben durchgeführt. Der Versuchsaufbau ermöglicht die visuelle Darstellung der Kugelbewegung des Ventils und die Verwendung eines Paares von induktiven Sensoren, um die exakte Position der Kugel während der Pumpzyklen zu jeder Zeit zu messen. Dieser Aufbau ermöglicht auch die Beobachtung von Phänomenen, die mit dem Ventil einer Gestängetiefpumpe zusammenhängen, zu untersuchen. Eine der wichtigsten Erkenntnisse ist das Schließen des Ventils in der Mitte des Pumpzyklus, was zu schnellem und hohem Verschleiß von Ventilkugel und -sitz führen kann.

Die aus den Experimenten gewonnenen Daten werden dann als Referenz für ein von der Firma AC2T research GmbH bereitgestelltes Simulationsmodell für eine Gestängetiefpumpe, welches das Verhalten der Ventile koppelt, verwendet. Das Modell ist in der Lage, das Verhalten des Pumpenteststandes mit Hilfe eines Korrektur- oder Kalibrierungsfaktors zu simulieren. Darüber hinaus lässt sich das Simulationsmodell leicht an unterschiedliche Ventilkäfiggeometrien anpassen und kann die Quadratwurzelabhängigkeit der kritischen Förderkolbengeschwindigkeit von der Kugeldichte verifizieren.

Table of Contents

Chapter 1	11
1.1 Scope and Objectives.....	12
1.2 Technical Issues	12
1.3 Overview of Dissertation	12
Chapter 2.....	13
2.1 Gas Lifting	13
2.2 Pumping.....	14
2.3 Oilfield Fluids	17
2.4 Sucker Rod Pumps.....	17
2.5 Surface Equipment	19
2.6 Rod String Component/ Sucker Rods.....	22
2.7 Subsurface System.....	23
2.8 Classification of SRPs	32
2.9 Problems with SRPs	34
2.10 Dynamometer Cards (Measurements)	35
2.11 Dynamometer Cards (Interpretation).....	37
2.12 Early Calculation Models.....	38
2.13 API RP 11L.....	40
2.14 Wave Equation	43
2.15 Computational Fluid Dynamics.....	47
Chapter 3	63
3.1 Pump Test Facility.....	63
3.2 Simulation	64
3.3 Test Methodology.....	67
3.4 Problems and Technical Difficulties.....	70
Chapter 4.....	73
4.1 Results Section	73
4.2 Discussion.....	91
Chapter 5.....	99
5.1 Summary.....	99
5.2 Future Work	100
References.....	101

Chapter 1

Introduction

The global need for energy is continually rising. Renewable energy is gaining traction, and stricter pollution laws are making the viability and justification for fossil fuels increasingly difficult. These factors necessitate the oil and gas business becoming more efficient in terms of finding potential resources and, most crucially, increasing the profitability of production. Sucker Rod Pumps and other artificial lift technologies are employed to get the most out of every oil and gas well. Even though SRPs are among the oldest ALS, there is still potential for advancement for them to compete with other ALS methods such as ESPs and PCPs. The main reason for implementing SRPs is that they are well-known among personnel and are relatively simple to operate. Many of the SRP characteristics are still unknown, owing to the difficulty in predicting their actual behavior downhole. However, it is common practice to use so-called dynamometer cards to monitor their downhole behavior from the surface, allowing for good approximations. Interpreting dynamometer cards is often difficult and can lead to incorrect conclusions. Due to high temperatures and spatial constraints, downhole monitoring is complex and expensive to carry out. As a result, investigating the behavior of each component on a test rig is essential and can provide a multitude of new information and possibilities. Furthermore, simulations provide a rather cheap and robust possibility of investigating different phenomena associated with SRPs. To verify the simulation, measurement data from a test rig can be used. The actual behavior of each downhole component can be investigated in detail using a combination of test rig data and simulation results. This information can be used to further optimize the production of hydrocarbons. Increasing the efficiency of existing infrastructures, developing new production methods, and minimizing the environmental footprint are among the main goals. These initiatives will ensure that the oil and gas industry remains competitive in the future when compared to renewable energy.

1.1 Scope and Objectives

This thesis aims to investigate the sucker rod pump standing valve movement. The information gathered from the test rig experiments is then further used to verify a Coupled Valve Sucker Rod Pump simulation. The simulation model is provided by AC2T research GmbH. A special standing valve cage, made of transparent Plexiglass, is utilized to visually depict the actual movement of the standing valve ball. The damage mechanisms of the downhole components are still not very clearly understood. The simulation model tries to predict an optimum operating range for a given plunger velocity and standing valve ball weight combination to investigate the root cause of valve seat damage.

1.2 Technical Issues

Several technical issues are present during the experiments in the PTF. These include positioning of both inductive sensors, accuracy issues during calibration of the sensors, noise in the data, and fluid flow measurement inaccuracies. All problems are explained in more detail in Chapter 3.

1.3 Overview of Dissertation

The second chapter is a literature review and covers the background of sucker rod pumps, their efficiency in comparison to other artificial lift methods, advantages and disadvantages, necessary surface and downhole equipment, dynamometer measurement and interpretation, as well as three different calculation models that are capable of converting surface data gathered from dynamometer measurements, into appropriate downhole data. In addition, the second chapter gives an overview of computational fluid dynamics and inductive sensors. Chapter three explains the test setup and the equipment utilized during the test rig measurements, the setup of the Coupled Valve Sucker Rod Pump simulation model, and the problems and technical difficulties encountered. Chapter four discusses the results of the test rig measurements and simulation along with a comparison between both. Chapter five summarizes and evaluates the findings of both, the test rig measurements and simulation, and gives an outlook on how to improve measurement accuracy and reduce the discrepancy between the test rig results and the CV-SRP simulation model.

Chapter 2

Literature Review

An Artificial Lift System (ALS) is a system that adds energy to the reservoir. ALS systems are implemented when the reservoir's own energy is not sufficient enough to lift the hydrocarbons to the surface by itself. Furthermore, artificial lift systems are also implemented into matured oil and gas fields that face depletion. The pressure at the well bottom must be sufficient enough to overcome the total pressure losses occurring throughout the flow path to the surface to ensure production. The well stops flowing naturally and dies if this criterion is not satisfied. In addition, surface conditions like separator pressure, flowline size, and other factors also have a direct influence on the total pressure losses and can potentially prohibit a well from flowing. There are several different ALS, such as Gas Lift, Electric Submersible Pump (ESP), Hydraulic Pump, Progressive Cavity Pump (PCP), and Sucker Rod Pump (SRP). The importance of artificial lifting can be seen in the sheer quantity of installations. There are more than two million oil wells worldwide of which about half are using some form of artificial lift method. The above-mentioned methods can be separated into two major groups, gas lifting, and pumping. [1, pp. 1-2]

2.1 Gas Lifting

These methods reduce the resistance to flow by injecting gas into the well-stream at some point downhole. In most cases, natural gas is used, but other gases like N₂ or CO₂ are also in use. This enables the well to flow again since the well's original bottom hole pressure is now sufficient enough to move the gas/liquid mixture to the surface. For continuous-flow gas lift, the gas is injected into the well tubing at a steady rate in comparison to intermittent gas lift. For intermittent gas lift, the gas is injected in a periodic manner. This happens after the fluid column accumulates to a sufficient enough height at the bottom of the well. A high volume of gas is then injected below the liquid column and pushes it to the surface resulting in slug production.

The injection of gas is interrupted until a new slug is formed downhole of sufficient enough height. This procedure is repeated resulting in a cyclic production. There is a special form of intermittent slug production available, plunger lift. A plunger is inserted below the accumulated liquid column, gets pressurized from below, and pushes the liquid column to the surface. [1, pp. 2]

2.2 Pumping

Pumping is the process of increasing the pressure in a well to overcome the total of flowing pressure losses that occur throughout the flow path up to the surface. Pumping can be further classified based on a variety of factors, such as the pump's operating principle. However, the most widely recognized categorization distinguishes between rod- and rodless-pumping based on how the downhole pump is driven.

Rod pumping systems use a string of metal rods to connect the downhole pump to the surface drive mechanism, which allows the pump to oscillate or rotate depending on the type of pump employed. Positive-displacement pumps, which need an alternating vertical movement to work, were the first kind of pumps used in water and oil wells. Walking-beam pumping, also known as sucker-rod pumping, is the most common and oldest type of rod pumping (SRP). It has a positive-displacement plunger pump, and the pumping unit has a pivoted walking beam, which is its most well-known surface feature. Long-stroke pumping units were developed because wells got deeper and deeper. The pump stroke lengths are much longer compared to conventional SRPs, but they use the same rods and downhole pumps. Long-stroke pumping units have different driving mechanisms than conventional SRPs. The most prominent ones used are pneumatic drive, hydraulic drive, or mechanical drive. Progressive Cavity Pumps also use a rod to drive the downhole pump, but the rod is not reciprocating but rotating.

Hydraulic pumping is another type of rodless pumping. It utilizes a high-pressure power fluid pumped downhole from the surface. The engine drives a positive displacement pump. Other types, that also use high-pressure

Rod-less pumping, as the name implies, does not utilize a rod string to drive the downhole pumps. These pumps are driven electrically or hydraulically. Examples are centrifugal, positive displacement, or hydraulic pumps.

Electric submersible pumps are the most prominent type of rodless pumping units. They employ a multistage centrifugal pump with an electric motor that is set below the fluid level. An electric cable connects the surface with the downhole motor providing power.

Hydraulic pumping is another type of rodless pumping. It utilizes a high-pressure power fluid pumped downhole from the surface. The engine drives a positive displacement pump.

Jet pumping is another type of hydraulic pumping. A nozzle in its downhole equipment creates a high-velocity jet stream from the power fluid injected at the surface. The jet pump converts the kinetic energy of this jet into useful work, lifting the combined stream of power fluid and well-produced liquids to the surface. A jet pump installation's downhole unit is the only oil-well pumping equipment on the market today that has no moving parts. [1, pp. 2-3]

SRPs are one of the most used artificial lifting methods worldwide, but this results in just 7% of the global production share (Figure 1).

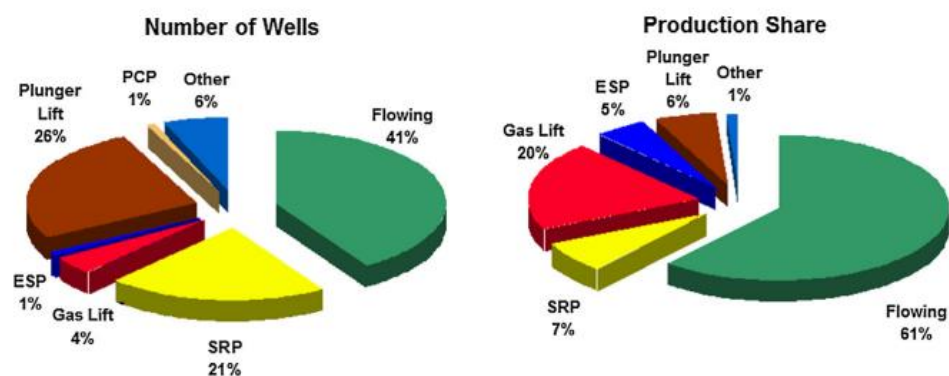


Figure 1: Number of Oil Well Installations and Total World's Share in Oil Production [1, pp. 4]

2.2.1 Lifting Capacity of SRPs

SRPs can only produce a moderate amount of liquid. Hydraulic pumping, progressive cavity pumping, and plunger lifting are other techniques with a moderate lifting capacity. In terms of liquid volume lifting capacity, SRPs and PCP are relatively similar at depths between 3000 and 6000 ft. PCPs have much lower investment and production costs than SRPs. As a result, PCPs have surpassed SRPs in popularity in recent years (Figure 2). [1, pp. 4]

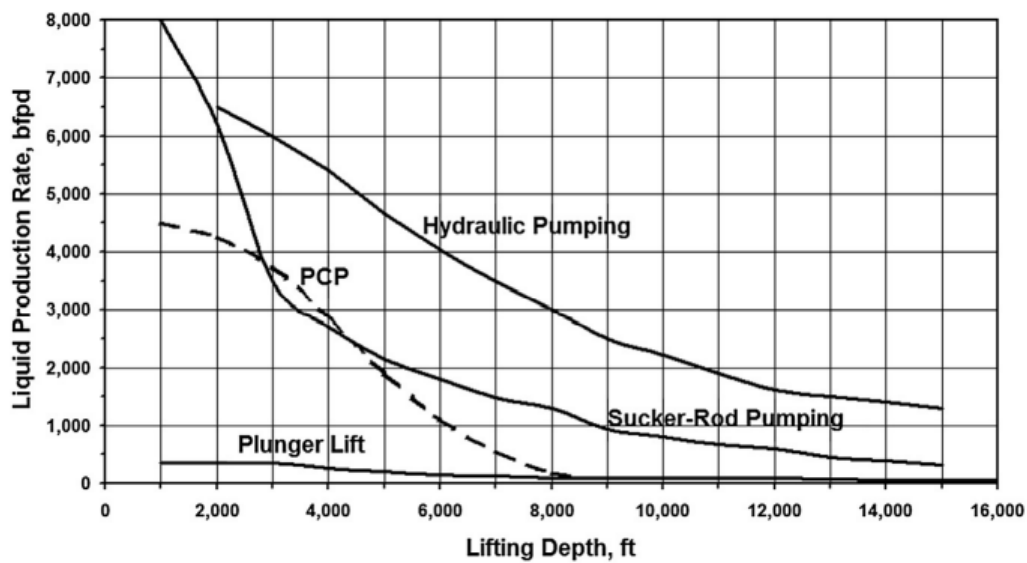


Figure 2: Moderat-Capacity ALS Maximum Liquid Capacities [1, pp. 5]

2.2.2 Efficiency of SRPs

The energy efficiency of the various artificial lift systems available today varies considerably. The total energy necessary to run the system and the hydraulic power spent moving the fluids to the surface are used to calculate the total efficiency of an artificial lift installation. The individual efficiencies of the system's components combine to provide this efficiency. The efficiency of the lifting mechanism, such as the energy efficiency of the pump utilized, accounts for the majority of the total efficiency, although power losses in the well and on the surface can also have a significant impact on the final result. Therefore, the use of a highly efficient lifting mechanism is a requirement for high total energy efficiency.

Positive displacement pumps used in hydraulic pumping systems typically have power efficiencies of approximately 50%. Artificial lift methods such as jet pumping and continuous-flow gas lifting have very poor efficiency, with maximums of roughly 30%. Among the numerous lift methods, intermittent gas lift has the lowest energy efficiency.

The maximum system efficiencies for sucker-rod pumping and ESP systems are around 60%. Although sucker-rod and ESP pumps can have great energy efficiency on their own, both lifting methods suffer from large downhole losses in their power transmission systems. In addition to these losses, having free gas in the pumps reduces their hydraulic output and, as a result, the overall system efficiency.

The PCP pump, which can convert mechanical energy to hydraulic work at a rate of more than 70%, is the best device available for artificial lifting. PCP systems require relatively simple surface and downhole installations and their components have low energy losses. Therefore,

PCP systems are the most efficient artificial lift technologies available. It's no surprise that the number of PCP pumping systems is rapidly increasing whenever well conditions fall within their application ranges (Figure 3). [1, pp. 5-6]

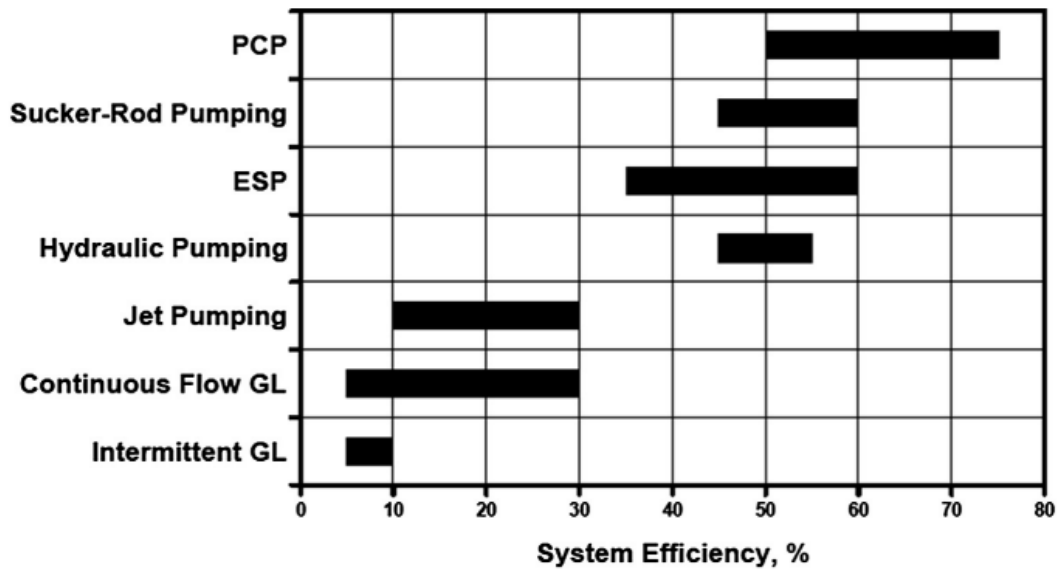


Figure 3: Different ALS Approximate Efficiencies [1, pp. 6]

2.3 Oilfield Fluids

Hydrocarbons and water are the most common fluids encountered in oil well production operations. Depending on the conditions, they can be in a liquid or gaseous state. Phase relations and physical parameters of flowing fluids change when conditions such as pressure and temperature change along the flow path (as fluids move from the well bottom to the surface). As a result, describing the fluid parameters that affect the fluid lifting process is critical for determining operating conditions or designing production equipment. However, all tests were carried out with water, since the simulation of Newtonian fluids is much easier. This is sufficient enough to verify the simulation model.

2.4 Sucker Rod Pumps

SRPs are the oldest and most widely used ALS method. More than 80% of all ALS implementations worldwide are SRPs. The development of the first beam-pumping installations goes back to the early history of mankind. In former times rod pumps were used to lift drinking water from rock formations close to the surface. These pumps used valves made out of stone, wooden rods for operating the pump from the surface, plunger pumps made of bamboo, and steam-powered prime movers. The first oil well was drilled and produced by Edwin Drake in 1859. The SRP's structural elements were made of wood with just the bearings made of iron

since the loads were small enough. Since there was a demand for deeper wells, different materials for the sucker rods were used, steel and later composites. Nowadays SRP's use the same basic working principle but were adapted to the needs of modern oil production. [1, pp. 14]

As mentioned above, sucker rod pumping is the world's oldest and most commonly utilized method of oil well production. The application range of sucker rod pumping became more defined with the introduction of several other lifting methods. SRPs are often employed to lift moderate to low liquid production rates from shallow to medium well depths because of the depth restrictions imposed by the limited strength of rod materials.

The main advantages and disadvantages of sucker rod pumping are listed below

Advantages

- simple to operate and analyze, and well-known to field personnel
- simple installation
- easy implementation of scale and corrosion treatments through the annulus
- production with very low pump intake pressure, up to abandonment

Disadvantages

- limited depth due to the mechanical strength of sucker rods
- corrosion protection of rod string is necessary
- limited in deviated or crooked holes
- sand or abrasive fluids can lead to pump failures
- free gas reduces liquid production significantly

[1, pp. 11-12]

SRP can be divided into three basic sub-systems. First, surface equipment consists of all installations on the surface including the major power source, the subsurface system that consists of the downhole pump and the actual lifting system, and the rod string component which is the connection between the surface and subsurface installations. The next chapter focuses on the different components and their explanation. [1, pp. 59-61]

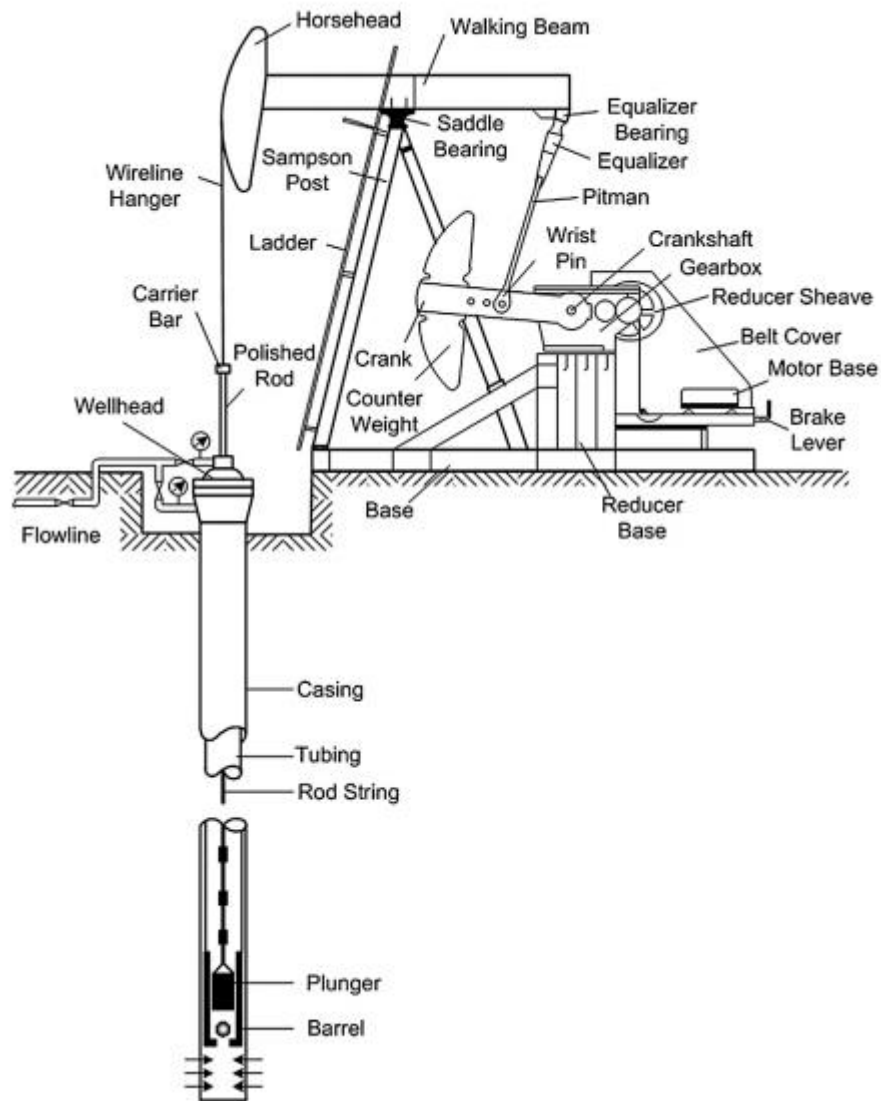


Figure 4: SRP Basic Components [1, pp. 60]

2.5 Surface Equipment

2.5.1 Prime Mover

Steam engines have been used to power early pumping units, and later slow-speed gas engines became the standard. During the late 1940s, electric motors achieved widespread acceptance, and today, electric motors power the majority of pumping units. Initially, the key advantages of electric power were its low cost, lower investment costs due to the low cost of electric motors, and the ease with which motors could be adapted to intermittent pumping. Some of these benefits are still present, even though the cost of power has risen significantly over time. Several factors contribute to whether a gasoline engine or an electric motor is used. The most important one is the availability of gas or electricity at the well site, but the decision cannot be made

without a thorough examination of the associated operational costs. The initial investment of a gas engine is substantially higher than that of an electric motor, but gas engines have a far longer service life. Due to increasing power costs, the energy expenses for an electric motor have continuously climbed in recent years. If gas is available at the well site, especially due to venting, gas engines can be more economical. [1, pp. 233-237, 2, pp. 4-6]

2.5.2 Gear Reducer

The gear reducer transforms the prime mover's high speed and low torque into the pumping unit's low speed and high torque requirements. The gear train is housed in a container. The gears are kept lubricated at all times by an oil reservoir integrated into the unit. They are considered the heart of the pumping unit and make up about 50% of the total investment of the pumping unit. The gear reduction ratio is usually 30:1 and the resulting output speed is around 20SPM maximum. [1, pp. 226-228, 2, pp. 7]

2.5.3 V-Belt Drives

A sheave and belt drive, also known as V-belt drive, connects the pumping unit's gearbox to the prime mover. The goal of this drive is to lower the prime mover's rather high rotating speed even more. The usual motor speed of a NEMA D electric motor is around 1,170 RPM; this speed is lowered to $1,170/30 = 39$ SPM by a typical gearbox with a reduction ratio of 30:1. The V-belt drives further reduction is needed to achieve practical pumping speeds for any sucker rod pumping unit. [1, pp. 230]

2.5.4 Counter Weight

The counterweights are attached either to the crankarm or to the walking beam. When they are attached to the crankarm it's called crank-balanced or conventional unit, and when they are attached to the walking beam it's called beam-balanced unit. Crank-balanced is the most widely used pumping unit type due to its simple operation and wide range of applications. Beam-balanced units are mostly used for shallow wells with low strokes per minute required. The counterweights act as a storage for energy during the downstroke, release this stored energy, and support the system during the upstroke. This results in a more balanced movement of the SRP. [1, pp. 236, 2, pp. 8-11]

2.5.5 Wellhead Assembly

A typical sucker rod-pump wellhead assembly consists of the following components (Figure 5).

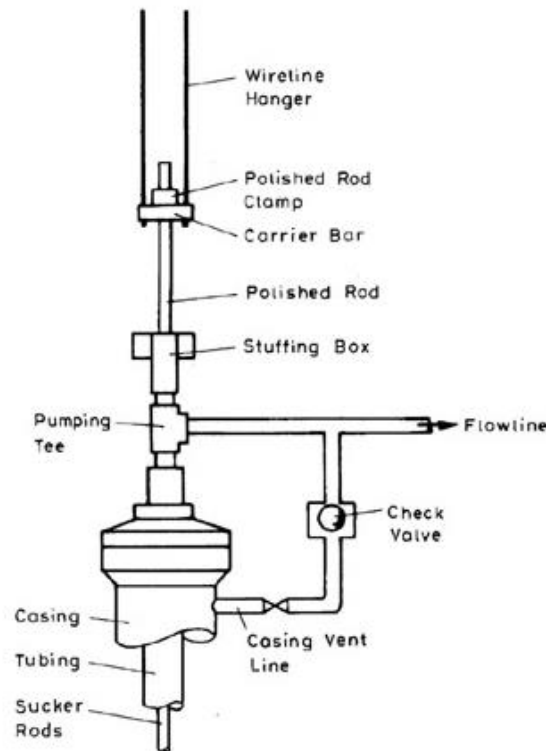


Figure 5: SRP Typical Wellhead Assembly [1, pp. 195]

The rod string's polished rod is the uppermost component. It follows a reciprocating motion with the movement of the walking beam. The wireline hanger transmits this reciprocating motion to the rods through the carrier bar. The polished rod moves inside the tubing head, which is topped with a pumping tee that directs the produced fluids into the flowline. The flowline and the casing vent line are usually connected by a short pipe segment, which allows the gas that separates in the casing–tubing annulus to be directed to the flowline. On this line, a check valve is installed to prevent the already produced fluids from flowing back to the well. A stuffing box is installed above the pumping tee to prevent well fluids from leaking into the atmosphere.

2.5.6 Pumping Unit

The prime mover is connected to the gear reducer via a belt. The whole unit is driven by a crankshaft which is connected to the gear reducer. The gear reducer is also connected to the walking beam with the pitman via the equalizer and equalizer bearing. The counterweights can be attached to the crank arm or the walking beam, called a crank-balanced unit or beam-balanced unit, respectively. The walking beam is connected to the Samson post, which is the

supporting structure of the whole system, through the equalizer bearing. The combination of pitman and walking beam transforms the rotational motion of the prime mover and gearbox into a reciprocating motion of the polished rod and sucker rods. The polished rod is attached to the horsehead with a carrier bar. The polished rod enters the stuffing box, which acts as a seal, goes through the tee, and is connected to the sucker rods. The sucker rods are then attached to the subsurface equipment, the downhole pump. [1, pp. 199-201, 2, pp. 7-12, 3, pp. 1167]

The pumping unit can be classified according to its geometry, the position of the counterweights, and the basic arrangement of components. The usual classification is based on whether the walking beam is a double-arm lever or a single-arm lever. They can further be distinguished according to their geometry and kinematic parameters, such as the direction of rotation. The most prominent types are conventional, air balanced, Mark II, and TorqueMaster or Reverse Mark.

2.6 Rod String Component/ Sucker Rods

The rod strings connect the surface pumping unit with the subsurface pump. The rod strings are typically 25 – 30 feet long and are made of steel or fiberglass. Sucker rods are connected with couplings. To avoid damage to the rod strings and tubing due to friction, so-called rod guides are installed. These rod guides consist of polymer elements and keep the rod string in a central position.

Continues sucker rods are an unconventional design with different advantages. They only require couplings at the top and the bottom of the string. They have less weight and are better suited for deviated wells. Sucker rods are made of steel, available in different grades, or fiberglass. Fiberglass rods can better withstand corrosive environments. However, they face several disadvantages. They may lose strength as a result of being exposed to high well-temperatures or hot-oiling procedures. And they are more prone to fatigue failures caused by repetitive loading or unloading throughout the pumping cycle. [1, pp. 126, 135-137, 141, 2, pp. 14-15]

2.7 Subsurface System

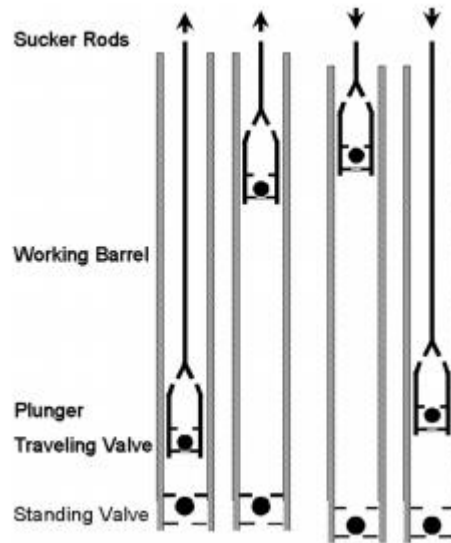


Figure 6: Schematic Description of the Pumping Cycle

The subsurface system consists of the downhole pump and various other components and installations.

Sucker rod pumps are also called plunger pumps. They consist of a cylinder called the barrel. In the case of a tubing pump, the barrel is connected to the tubing, and in the case of an insert or rod pump, the barrel is connected to the sucker rods. The next component is a plunger. It is connected to the sucker rods and acts as a piston. The standing valve is attached to the bottom of the working barrel, whereas the traveling valve is attached to the plunger. The last component is an anchor to hold the pump in place. If two-phase flow is present, the formation fluids have to be separated before entering the pump. Therefore, a perforated gas anchor is usually located at the bottom of the pump attached to the barrel. It increases the pump efficiency by redirecting most of the free gas into the casing-tubing annulus. [1, pp. 61-63]

2.7.1 Plunger and Barrel

A sucker rod pumps barrel and plunger are both tubes that have been manufactured and polished to the smallest tolerances possible. The nominal size of a sucker rod pump equals exactly the inside diameter of the barrel. In the case of metal plungers, the outside diameter of the plungers is only slightly smaller than the barrels inside diameter. The distance between the plunger outside diameter and the barrel inside diameter is called plunger fit. This clearance is very small, in the order of a few thousand of an inch.

2.7.2 Barrel

The inside wall of the barrels is very smooth. This is achieved with honing. Barrels are the largest and most expensive component of downhole pumps. There are several types of barrels available. Pin-end or box-end, representing the threads applied on the barrel at both sides, as well as heavy-wall and thin-wall. Heavy-wall and thin-wall barrels can be distinguished according to their wall thickness, about 3/16 in and 1/8 in, respectively (Figure 7). The standard length for barrels is 24 ft. In case of abrasive or corrosive environment chrome or nickel-carbide plating is applied. [1, pp. 72, 73]

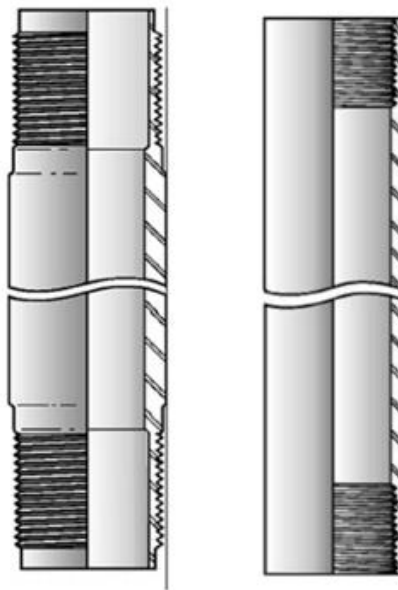


Figure 7: Heavy Wall Barrel with Pin End (left) and Thin Wall Barrel with Box End (right)

2.7.3 Plunger

For deep wells, an effective seal can only be achieved with metal plungers. They provide a close fit between barrel and plunger. Depending on the downhole environment plungers with plain or grooved outside surfaces are used (Figure 8). The first one is used when facing sand production since the sand particles can accumulate and are trapped in the grooves. Therefore, damage to the plunger and barrel is reduced. The second one is not a good choice for sand production because small grooves can develop on the polished surfaces resulting in high liquid slippage due to the pressure differential across the plunger. Plungers are also available in pin-end or box-end types. There are different materials available with sprayed metal plungers being the most common ones since they are economical and provide resistance against moderately abrasive fluids. [1, pp. 73-76]

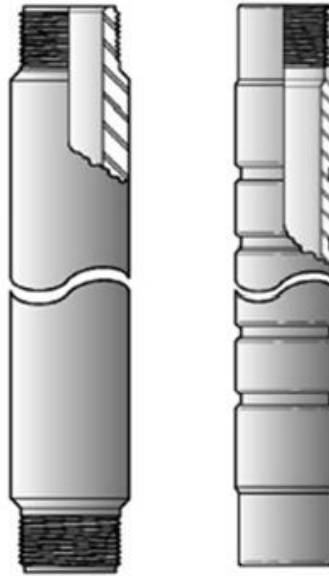


Figure 8: Pin End Plain Metal Plunger (left) and Box End Grooved Metal Plunger (right)

2.7.4 Pump Types

There are two main types of sucker rod pumps, the tubing, and the insert or rod pump. The main difference shows in the way the working barrel is installed in the well.

Tubing pumps provide a simple and robust design and are the oldest type of sucker rod pumps (Figure 9). A tubing pump's working barrel is an essential component of the tubing string. It is attached to the bottom of the tubing string and both, the tubing and the barrel, are run to the appropriate depth together. This design provides for a barrel diameter that is just slightly smaller than the inside diameter of the tubing. The primary disadvantage is that servicing the working barrel requires pulling the entire tubing string. The standing valve is locked into a seating nipple that is placed below the barrel. [1, pp. 63]

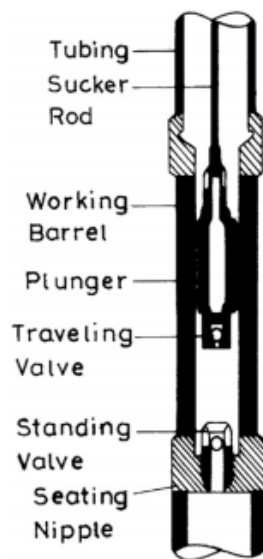


Figure 9: Tubing Pump Basic Components [1, pp. 64]

In contrast to a tubing pump, the rod or insert pump is a complete pumping system that is run into the well on the sucker rod string (Figure 10). The assembly consists of the working barrel, the plunger that is located inside the barrel, and the standing and traveling valve. The only part that has to be run with the tubing string is the seating nipple. [1, pp. 64]

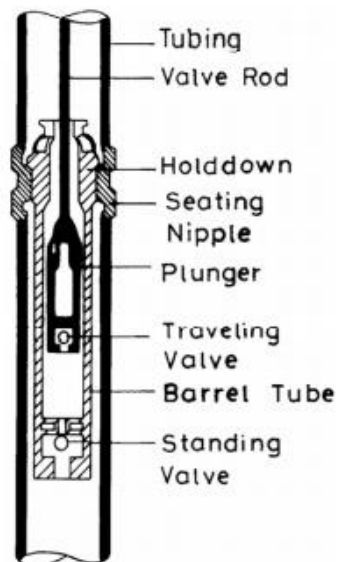


Figure 10: Rod Pump Basic Components [1, pp. 64]

Several factors influence the type of pump that should be utilized in a specific installation. Tubing pumps, in general, can transport higher quantities of liquid than rod pumps. The most significant drawback of tubing pumps is that if the working barrel fails, the entire tubing string

must be pulled. Before making a final decision, several operational issues such as gas production, sand, and the presence of corrosive media should be considered.

2.7.5 Valve and Cage

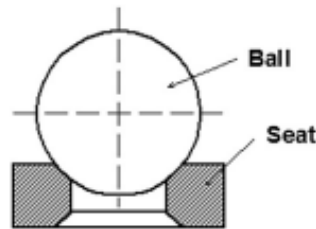


Figure 11: Valve Seat and Ball

The proper operation of the standing and traveling valve is critical to a successful sucker-rod pumping operation. The ball-and-seat concept is used to operate these simple check valves. Seats are made of corrosion-resistant metals that have been machined, precision ground and finished. They usually can be operated on both sides. To ensure a tight seal, the metal balls are precision polished, and each ball and seat combination is lapped together. Finally, the matched sets are vacuum tested. Due to the extremely high differential pressure across the valve during pumping, even minor initial defects on the sealing surfaces, as well as later abrasion or corrosion damage, generate significant liquid slippage and quick degradation of the valves. Therefore, a highly accurate sealing action between the ball and the seat is necessary. During valve operation, the ball is seated and unseated on the valve seat regularly. The ball hits the seat with strong impact forces due to the high pressures at pump depth. When the ball is elevated and its movement is not limited, it may wander off the centerline of the seat bore. The ball thus only touches one side of the seat during the closing, causing excessive wear on both the seat and the ball. Valve cages, which guide and restrict the ball's movement, are intended to reduce valve damage and improve performance. [1, pp. 77]

Check valves are flow-sensitive, therefore, it's critical to size them appropriately. They only allow one direction of flow. They gradually close as the fluid flow decreases. One of the most common issues is oversizing. A too-large valve will lead to pressure loss and will, therefore, not fully open during operation. This will cause the valve to chatter. Chatter means a constant movement of the ball resulting in uncontrolled collisions between the ball and the seat. This reduces the lifespan of the valve substantially by producing wear on the metal internals. To properly size a ball check valve, pressure, temperature, flow rate, and viscosity of the fluid have to be known. Valves are the core component of a sucker-rod pump. Balls and seats are made of various metals; when abrasion and corrosion are not an issue, stainless steel or alloy materials

are used. Tungsten carbide is another reliable material, however, it cannot be used in wells with H₂S or CO₂; in these conditions, nickel carbide balls and seats are preferable. Exotic ceramics are also becoming increasingly popular. For example, zirconia ceramic balls and seats are chemically inert, completely corrosion and abrasion-resistant, and have a longer life than metal valve components. [1, pp. 77-78, 4]

Valve cages, which guide and restrict the ball's movement, are intended to reduce valve damage and increase performance. When the ball's movement is unrestricted, it may rattle, or move away from the centerline of the seat bore, when lifted. The ball may therefore only hit one side of the seat during closure, causing excessive wear on both the seat and the ball. Valve cages restrict the lateral and vertical motion of valve balls while providing the least amount of flow restriction possible across the valve assembly. Valve cages can either be open or closed for both, the standing valve and traveling valve. Both types of valves are specified by the API. These conventional valve cages have two main problems. The liquid flow through the valve is restricted, and the dead space is relatively large. The dead space is the space between the standing valve and traveling valve at their bottom-most position. [1, pp. 80]



Figure 12: Standing Valve Open API Cage [1, pp. 80]

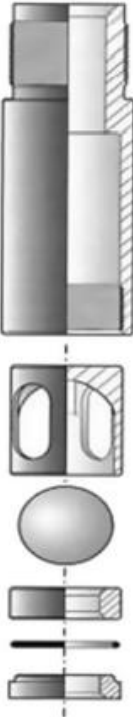


Figure 13: Standing Valve Closed API Cage [1, pp. 81]

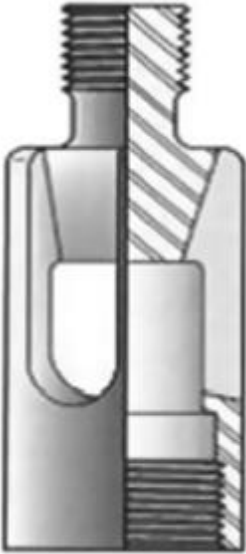


Figure 14: Traveling Valve Open API Cage [1, pp. 81]

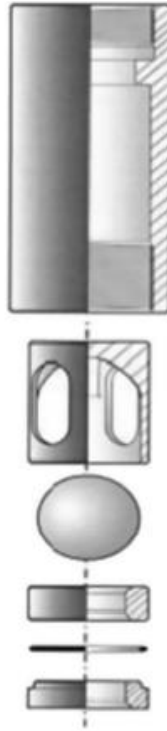


Figure 15: Traveling Valve Closed API Cage [1, pp. 82]

To overcome these problems the HIVAC (high volume and compression) valve cage can be used. The dead space is much shorter than for conventional API cages, and the liquid flow capacity is substantially higher, up to five times. Another advantage is that the fluid flows in a circular motion through the valve, due to the helically twisted guides, and therefore, keeps solids suspended longer in the fluid. This valve cage is not as sensitive to gas locking as the conventional API ones. [1, pp. 82, 83]

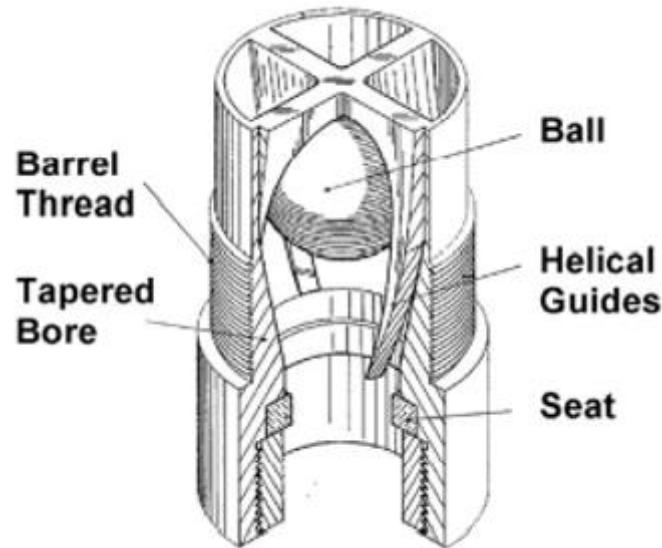


Figure 16: Valve Cage HIVAC [1, pp. 82]

2.7.6 Anchor

The stationary element of a rod pump, whether it's the barrel or the plunger, is attached to the tubing string via hold-downs or anchors. The hold-down is put through a seating nipple in the tubing, where it is mechanically secured or kept in place by friction forces. The pump's operation exerts vertical forces on the pump assembly's stationary component, which are immediately transmitted to the hold-down. Otherwise, the pump will dislodge and cease producing if the anchoring mechanism cannot withstand these forces. By isolating fluid column pressure from bottom-hole pressure, the hold-down also prevents well fluids from leaking back into the tubing. [1, pp. 83, 107, 3, pp. 1174, 1175]

Throughout the pumping process, the pump should be submerged in fluid and therefore, placed below the fluid level. The pumping cycle begins with the plunger and traveling valve being pulled up through the barrel by an upward stroke of the sucker rods. The traveling valve closes, and the standing valve opens. Fluid can now enter the barrel filling the void space. This is governed by the plunger moving upwards. The fluid on top of the plunger is then pulled upward in the tubing towards the surface during this motion. This marks the end of the upward stroke. In the next step, the traveling valve opens and the standing valve closes on the plunger's downward stroke, trapping the fluid above it. The confined fluid is forced to flow through the open traveling valve to the top of the plunger by the plunger's downward motion. With each pump stroke, more fluid is transferred to the tubing until the column of fluid reaches the surface and flows into the flow lines. This working principle results in periodic production. [1, pp. 61-63, 5]

2.8 Classification of SRPs

The American Petroleum Institute's requirements apply to the vast majority of sucker-rod pumps in use across the world (API). API has categorized and assigned a letter designation to the pumps defined in API Spec 11AX. Tubing pumps are identified by a two-letter code, while rod pumps are identified by a three-letter code. The following is an explanation of the letter codes.

- The first letter identifies the basic type of pump:
 - R, rod pumps
 - T, tubing pumps
- The second letter indicates whether the barrel is heavy- or thin-walled. Tubing pumps are only available in heavy-walled barrels. Pumps with metal plungers and pumps with soft-packed plungers have different code letters:
 - Metal Plungers
 - X, heavy wall, internally-threaded
 - H, heavy wall
 - W, thin wall
 - Soft-Packed Plungers
 - S, thin wall
 - P, heavy wall
- The third letter is used to indicate the location of the seating assembly, only used for rod pumps. For a traveling barrel pump the seating assembly or hold down is always at the bottom. Other rod pumps can be seated at both locations, top and bottom:
 - T, traveling barrel with bottom hold-down
 - A, anchor at the top
 - B, anchor at the bottom
- The specification also includes the nominal tubing size given by a two-figure code. The pump bore size is given by a three-figure code. Examples for both are listed in Table 1 and Table 2. [1, pp. 65]

Table 1: Nominal Tubing Size API Spec 11AX [1, pp. 70]

Nominal Tubing Size	
Code	Tubing Size [in]
15	1.9
25	2 3/8
25	2 7/8
30	3 1/2
40	4 1/2

Table 2: Pump Bore Size API Spec 11AX [1, pp. 71]

Pump Bore Size	
Code	Pump Size [in]
106	1 1/16
125	1 1/4
150	1 1/2
175	1 3/4
178	1 25/32
200	2
225	2 1/4
250	2 1/2
275	2 3/4
375	3 3/4

- Furthermore, the seating assembly is identified by a single letter, M for mechanical, and C for cup-type.
- The last numeric group designates the pump length in [ft]. The first number indicates the length of the barrel, the second number gives the length of the plunger, and the last two numbers indicate the lengths of the barrel extensions. [1, pp. 71]

2.9 Problems with SRPs

The sucker-rod pump functions similarly to any single-acting piston pump. The way the piston, or plunger, is driven is the most fundamental distinction between a surface pump and a sucker-rod pump. The rod connecting the drive mechanism to the piston in surface pumps, such as mud pumps, is relatively short and does not alter significantly during operation. As a result, the stroke length of the piston is equal to the stroke imposed by the driving mechanism. The plunger of a subsurface pump, on the other hand, is operated by a string of rods that can range thousands of feet. This long string constantly stretches and recoils due to its elastic behavior, making the plunger's action complicated to predict. As a result, the stroke length of a plunger cannot be easily determined from the stroke length measured at the surface. In real-world scenarios, ideal conditions are most likely never met. Ideal conditions are the production of single-phase liquids only, and a complete filling of the barrel with well-fluids during the upstroke. The pump's efficiency will be severely hindered if any of these two conditions is not fulfilled. The variations in valve action throughout the cycle are the source of all issues in such situations. Both valves are basic check valves that open or close based on the relation between the pressures above and below the valve seat. As a result, the valves do not always open and close exactly at the end of the plunger's upstroke and downstroke. Therefore, the effective plunger stroke length, or the portion of the stroke used to raise well fluids, is typically less than the entire plunger stroke length.

Another problem, as mentioned above, is the presence of free gas in the reservoir. If there is free gas present, the traveling valve remains closed throughout the downstroke until the free gas is entirely compressed and the pressure within the barrel exceeds the pressure in the liquid column above the traveling valve. Due to the compressible nature of gas, the effective stroke length of the plunger gets reduced. This problem can also be seen during the upstroke. First, the gas-liquid mixture inside the barrel starts to expand. Therefore, the standing valve does not open immediately. It opens when the pressure above the standing valve is the same as the wellbore pressure. This delayed movement of the plunger also reduces the effective stroke length and the barrel gets filled with fluids only partially. [1, pp. 101, 6]

Another problem is when the inflow performance of the well is lower than the pump capacity. This also leads to incomplete filling of the pump barrel. In this case, a so-called Pump-Off Controller (POC) can be used. The rod pump is monitored by this POC, which detects when the pump chamber is not full and allows the well to recharge before continuing pumping. An incomplete filling of the barrel over a longer period leads to a waste of energy, and puts a lot of strain on all components, like the rod string, tubing, pump, and gearbox. [1, pp. 405-408]

Buckling is another issue unique to sucker rod pumps. Buckling occurs when compressive forces acting during the downstroke exceed a critical level, causing the rod string to bend. This causes tube and rod string wear at contact points due to contact between the rod string and the tubing. A leaking tubing or damaged rods might indicate buckling. The mechanical structure of the rod strings is the cause of buckling. Their length to diameter ratio is very high. To detect buckling, the load status of the rod string must be assessed. Buckling does not occur during the upstroke, but can occur during the downstroke, and is highly impacted by the compressive nature of the buoyant forces acting on the bottom taper, as well as external forces such as mechanical friction between the rods and the tubing, drag in the plunger-barrel fit for high viscous fluids, and pressure drop across the traveling valve. Heavy rods, also called sinker bars, are one way to prevent buckling. The sinker bars' length must be sufficient enough to compensate for the compressive forces acting on the rod string's bottom. This shifts the critical point, where buckling starts, further to the top. Sinker bars that are inadequately designed, on the other hand, are also prone to buckling. To eliminate buckling, not only the static forces acting on the rod string must be considered, but also the dynamic forces. This can only be accomplished by employing the results of the wave equation. [1, pp. 107-109, 150-152, 192]

Sucker rod pumps can also be affected by operational failures such as high temperatures, corrosion, and sand or abrasives. Sucker rod pumps are often not used in very deep wells, therefore failure due to high temperatures is rarely an issue. Temperature-resistant materials can be used if the pump is subjected to high temperatures. Corrosion can be caused by the presence of brine, carbon dioxide, and hydrogen sulfide. Pump materials should be chosen carefully based on the environment to which the pump will be exposed during production to minimize corrosion problems. Sand production can result in two issues. Plugging of the internals of the pump such as the plunger and erosion which can further lead to corrosion. To mitigate sand production, the formation can be stabilized using chemical injections, gravel packs or sand screens can be installed downhole, the production can be altered to reduce the amount of produced sand, or cope with sand production by using materials that can withstand it. [7]

2.10 Dynamometer Cards (Measurements)

The most essential equipment for measuring the performance of the pumping system is the dynamometer, which records the loads that occur in the rod string. A polished rod dynamometer or special downhole measuring equipment, called downhole dynagraph, can be used to monitor these loads at the surface or at pump depth. Rod loads are measured vs. rod displacement or pumping time for one or more full pumping cycles in both cases. It is very important to analyze the changes in rod loads generated by all the forces acting along the rod string because this

properly reflects the pump's as well as the surface pumping unit's function, and reveals important information regarding downhole and surface conditions.

The dynamometers can be separated into polished rod dynamometers that are used on the surface, and downhole dynagraphs that are attached to the equipment downhole. The main advantage of downhole dynagraphs is that they can measure the rod loads immediately above the pump and are not affected by the forces that act on the string from the pump to the surface. Nevertheless, the disadvantage of having to run the instrument in the well considerably outweighs the benefits of direct measurement.

Therefore, only the polished rod dynamometer will be explained. Polished rod dynamometers measure the loads that act on the rod string during a pumping cycle on the surface at the polished rod. There are three types available, mechanical, hydraulic, and electronic. Both, the mechanical and hydraulic dynamometers generate a continuous plot of polished rod load vs. polished rod displacement, compared to the electronic dynamometer which records the loads and displacements as a function of time. Since the point of interest is downhole, a damped wave equation is used to derive the information from downhole taking into account the elastic nature of the rod string. This is by no means accurate and therefore, subject to interpretation by experts. A different approach is the use of AI-assisted programs utilizing shape recognition. [1, pp. 448-454, 3, pp. 1191-1193]

2.11 Dynamometer Cards (Interpretation)

The interpretation of dynamometer cards can give information about the whole system, such as a leaking tubing, a defective pump, inadequate position of the counterweights, under- or oversized pumping unit, gas locking of the pump, or fluid pound. [8]

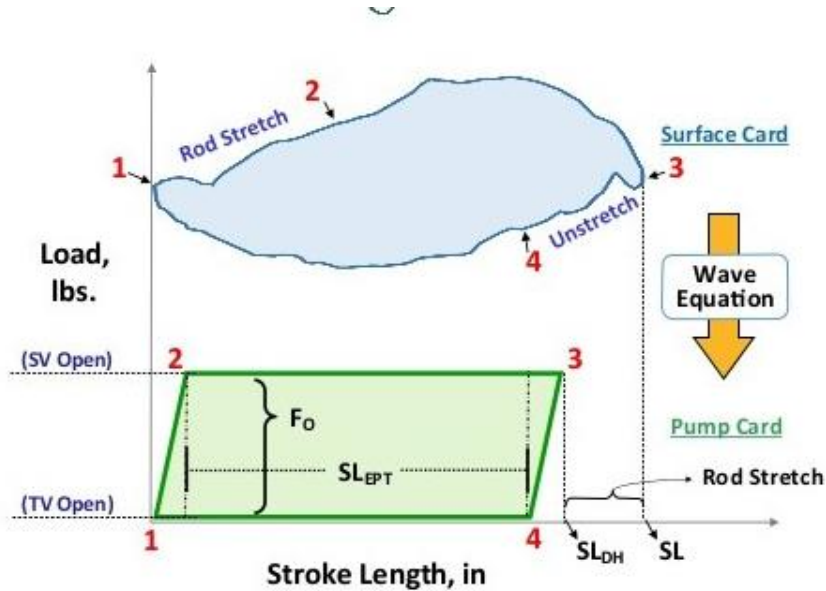


Figure 17: Dynamometer Card Explanation [8]

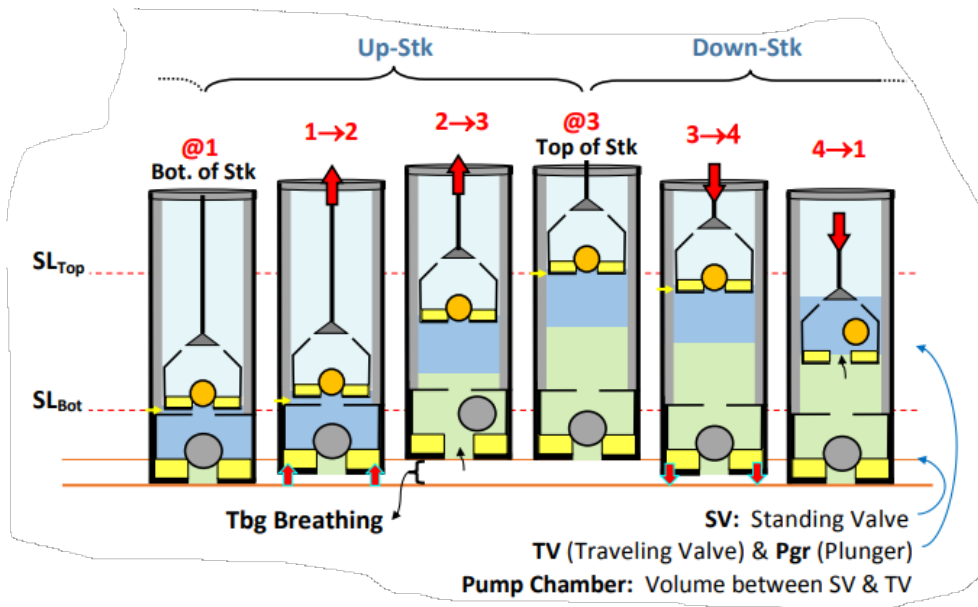


Figure 18: Cycles of Pump Card [8]

Figure 17 shows a simplified surface card. 1-2-3-4 represents the ideal case, inelastic rigid rod string, completely filled pump, incompressible fluid. Position 1 represents the beginning of the upstroke. No load is applied to the rod string. 1-2 represents the stretching of the rod string until it reaches its maximum value at point 2. From positions 2-3 the actual lifting of the fluid takes

place. Position 3 indicates the end of the upstroke. Position 3-4 represents the contraction of the rod string to its initial length, reached at position 4. From position 4-1 the plunger moves through the fluid indicating the downstroke and a new cycle starts. [8]

Measuring the downhole conditions directly is complicated and expensive, as mentioned above. Therefore, the actual downhole conditions have to be calculated from the measured surface data. The most essential aspect of the sucker-rod string is its elasticity, which accounts for the difficulty in estimating downhole conditions from surface data. All impulses created by the pumping unit's motion at the surface are quickly conveyed downhole due to the rod string's highly elastic nature. Similar signals are sent to the surface by the operation of the subsurface pump. All of these impulses travel along the string at the speed of sound in the form of elastic force or stress waves. These waves interferences and reflections have a significant impact on the displacements and loads observed at various locations along the string.

2.12 Early Calculation Models

With the early models, the elastic behavior of the rod string was predicted by using simplified mechanical models to determine the pumping parameters. The complexity of describing the real behavior of the pumping system necessitates the use of basic models. Most of the approximate equations underlay the assumption that the rod string is a concentrated mass driven by the polished rod. The performance of the pumping system is modeled using this method by comparing it to a spring moving a concentrated mass. With these models, the main parameters of the pumping unit can be calculated by using easy mathematical solutions resulting in simple formulas.

Furthermore, several other simplifications were assumed, although they introduce some errors in the model. The movement of the polished rod is approximated by a simple harmonic motion and the pumping geometry is assumed to be conventional.

The "wet weight" of the rods is commonly stated as the sum of the rod string weight and the buoyant force, which is rather simple to calculate. Because friction forces are difficult or impossible to estimate, they are not included in most calculation procedures. If the concentrated mass model is utilized, dynamic forces at the polished rod are also straightforward to find. By multiplying the mass being pushed by the acceleration at the polished rod, the inertial forces are determined. It is common practice to use Mills' "acceleration factor" formula:

$$\delta = \mp \frac{S * N^2}{70,500} \quad (1)$$

where:

δ = acceleration factor

S = polished rod stroke length, *in*

N = pumping speed, *SPM*

The inertia of the moving masses, the rod string, and the fluid column generate dynamic forces. They add to the static loads during the upstroke and must be subtracted from the static rod weight during the downstroke. When calculating dynamic loads, the effects of stress waves in the rod string are ignored. They are just the forces required to accelerate the rods and fluid column, which are both assumed to be concentrated, inelastic masses. As a result, this simple formula (1) can give sufficient calculation accuracy as long as the following assumptions are true: shallow to medium-depth wells with small pumping loads.

The total of the fluid load on the plunger, as well as the static + dynamic loads, can now be used to approximate the peak polished rod load (PPRL). To account for friction forces, Mills' formula ignores the rods' buoyancy:

$$PPRL = F_0 + W_r(1 + \delta) \quad (2)$$

where:

$PPRL$ = peak polished rod load, *lb*

F_0 = fluid load on plunger, *lb*

W_r = total rod string weight in air, *lb*

δ = acceleration factor

The plunger's fluid load can be calculated with:

$$F_0 = 0.433HA_pSpGr \quad (3)$$

where:

F_0 = fluid load on plunger, *lb*

H = depth of dynamic fluid level, *ft*

A_p = plunger area, *in²*

$SpGr$ = specific gravity of fluid produced.

During the downstroke the buoyant weight of the rod string and the dynamic force act in opposite directions. Therefore, the buoyant weight of the rod string gets decreased by the dynamic force resulting in the minimum polished rod load (MPRL).

$$MPRL = W_{rf} - W_r \delta \quad (4)$$

W_{rf} = buoyant rod weight, *lb*, can be expressed as:

$$W_{rf} = W_r(1 - 0.128SpGr) \quad (5)$$

Substituting W_{rf} into the above formula results in the MPRL:

$$MPRL = W_r(1 - 0.128SpGr - \delta) \quad (6)$$

where:

$MPRL$ = minimum polished rod load

W_r = total rod string weight in air, *lb*

$SpGr$ = specific gravity of the produced fluid

δ = acceleration factor.

[1, pp. 250-257]

2.13 API RP 11L

The early models led to unsatisfactory results and therefore, the Sucker Rod Pumping Research Inc., founded in 1954, introduced a more reliable model. This model also relies on several simplifications. The pumping unit is perfectly counterbalanced, only steel rods are used, the slip of the prime mover is low, the tubing is assumed to be vertical and anchored, and the polished rod is driven by a conventional pumping unit.

The final correlations' results were plotted on a series of charts first published by the American Petroleum Institute. Therefore, thousands of experimental runs were conducted with different stroke lengths, pumping speeds, and plunger sizes. The results could only be correlated by using nondimensional parameter groups due to their complexity.

When compared to the results obtained from the solutions of the wave equation, this approach has become the standard method for determining the operational parameters of sucker rod pumps. The main problem with this method is that hand calculations and visual read-offs are still required, which might affect the accuracy.

The rod strings' elastic behavior is correctly accounted for in the API RP 11L. At both ends, top and bottom, the rod string gets excited, due to the polished rod and by the motion of the downhole pump, respectively. The elastic rod string transmits the surface motion, determined by the kinematic of the pumping unit, throughout its length in form of elastic force waves and vibrations. Similarly, the pumping unit also forms elastic force waves and vibrations. These

force waves and vibrations of both sources interact with each other and get reflected. This substantially influences the forces and displacements that occur at various points along the rod string. The undamped natural frequency of the rod string is calculated by:

$$N_0 = \frac{v_s}{4L} 60 = \frac{15v_s}{L} \quad (7)$$

where:

N_0 = undamped natural frequency, $\frac{\text{strokes}}{\text{min}}$

v_s = velocity of sound in the rod material, $\frac{ft}{s}$

L = length of the rod string, ft

The wave propagation through the rod string happens with the speed of sound. Therefore, the formula can be rewritten with a typical value of $16300 \frac{ft}{s}$ for steel rods:

$$N_0 = \frac{245000}{L} \quad (8)$$

This formula is true for straight rod strings and has to be adapted for tapered rod strings. In general, the natural frequency of the waves is considerably higher for tapered rod strings.

In the next step, a group of dimensionless parameters is determined using the simulation results of an analog model. These dimensionless parameters can be used as reliable input parameters for widely different pumping conditions.

In the next step, these dimensionless parameters are used to plot dependent parameters, also processed with the introduction of dimensionless groups. The resulting charts are used to calculate operational parameters.

The procedure looks as follows:

First, the plunger stroke length for an anchored tubing is calculated:

$$S_p = S \frac{S_p}{S} \quad (9)$$

where:

S_p = downhole stroke length of the plunger, in

$\frac{S_p}{S}$ = dependent variable

S = stroke length of the polished rod, in

Second, the plunger displacement is calculated, assuming 100% filling efficiency:

$$PD = 0.1166d^2S_pN \quad (10)$$

where:

PD = displacement of the pump, *bpd*

S_p = stroke length of the plunger, *in*

N = pumping speed, $\frac{\text{strokes}}{\text{min}}$

d = size of the plunger, *in*

Third, the polished rod power is calculated:

$$PRHP = 2.53E - 6 \frac{F_3}{Sk_r} S^2 N k_r \quad (11)$$

where:

$PRHP$ = horsepower of the polished rod, *HP*

$\frac{F_3}{Sk_r}$ = dependent variable

S = stroke length of the polished rod, *in*

N = pumping speed, $\frac{\text{strokes}}{\text{min}}$

k_r = rod string spring constant, $\frac{\text{lb}}{\text{in}}$

In the last step, the peak net torque is calculated. A perfectly balanced pumping unit is assumed.

$$PT = \frac{2T}{S^2 k_r} \frac{S^2}{2} k_r \left(1 + 10 \left(\frac{W_{rf}}{Sk_r} - 0.3 \right) T_a \right) \quad (12)$$

where:

PT = speed reducers peak net torque, *in – lb*

$\frac{2T}{S^2 k_r}$ = dependent variable

S = stroke length of the polished rod, *in*

k_r = spring constant of the rod string, $\frac{\text{lb}}{\text{in}}$

$\frac{W_{rf}}{Sk_r}$ = dimensionless independent variable

T_a = adjustment factor for the torque

To accurately represent and simulate the rod strings' complex behavior a better model is needed. [1, pp. 258-273]

2.14 Wave Equation

The wave equation is the only way to reach this level of precision. After Gibbs is the most common form of this equation. The rod string can be calculated using a one-dimensional damped wave equation since it meets all physical conditions for a perfect slender bar.

Taking the forces that act on the rod string into account and using Newton's second law, leads to:

$$m \frac{\partial^2 u}{\partial t^2} = F_x - F_{x+\Delta x} + W - F_d \quad (13)$$

where:

F_x = tension force representing the upward pull of the rod element

$F_{x+\Delta x}$ = tension force representing the downward pull of the rod element

W = buoyant weight of the rod element

F_d = dampening force in opposite direction to the rod elements movement

The axial distance and displacement are represented by x and u , respectively. The buoyant weight of the rod element doesn't change and can therefore be neglected.

Since mechanical stresses are present in the rod sections, tension forces can be expressed with them:

$$F_x = S_x A \quad (14)$$

$$F_{x+\Delta x} = S_{x+\Delta x} A \quad (15)$$

Substituting both of these expressions into equation (13) results in:

$$m \frac{\partial^2 u}{\partial t^2} = (S_{x+\Delta x} - S_x) A - F_d \quad (16)$$

Hooke's law gets applied since sucker rods are exposed to elastic deformation in normal operation. The stress at any cross-section is proportional to the deformation of the actual rod element:

$$S = E \frac{\partial u}{\partial x} \quad (17)$$

where:

S = mechanical stress, *psi*

E = Young's modulus of elasticity of the rod material, *psi*

$\frac{\partial u}{\partial x}$ = rod strain

The equation of elastic deformation gets substituted into equation (16). The mass m gets expressed with the volume and density of the rod element. This leads to the final form of the wave equation:

$$\frac{\Delta x A \rho}{144 g_c} \frac{\partial^2 u}{\partial t^2} = E A \Delta x \frac{\partial^2 u}{\partial x^2} - F_d \quad (18)$$

where:

ρ = rod material density, $\frac{lb}{ft^3}$

g_c = gravitational constant, 32.2

In the next step the dampening force, F_d , has to be determined. As shown by DaCunha-Gibbs, a perfect description of the downhole pump's operating conditions is only achievable if dampening forces or friction forces are accurately simulated. The dampening forces, in general, have the effect of removing energy from the system along the rod string. According to energy balance, the difference between the power provided at the polished rod and the power available at the pump is equal to the power lost due to dampening forces.

The entirely different nature of the two types of friction occurring in sucker rod pumps makes accurate modeling of dampening forces difficult. The two types are fluid friction and Coulomb friction. Fluid friction is proportional to the relative velocity, or shear velocity between the fluid and rods. It is caused by the viscous forces in the annular space throughout the whole length of the rod string. Coulomb friction, on the other hand, occurs when stationary and moving system components collide; its magnitude is determined by the normal forces pushing against each other, as well as the friction factors particular to the surfaces in contact. Due to the different behavior of its two main components, the net friction force cannot be explained by a single formula. As a result, if there is a significant Coulomb (mechanical) friction (particularly in deviated wells), the wave equation must be changed to incorporate two damping forces.

Coulomb friction typically occurs in three different areas on a sucker rod, friction between the rods and the tubing, friction in the stuffing box, and friction in the downhole pump. All three friction forces are small and the friction between the rods and the tubing is negligible in the case of a vertical wellbore. To simplify the equation for the damping force it is common practice

to account for the Coulomb friction with some kind of a viscous force. In the presence of viscous dampening only, energy is continuously lost along the rod string. This is due to the viscous forces imposed on the outer surface of the rods from the fluids. Furthermore, Gibbs assumed the dampening force to be proportional to the mass of the rod, resulting in:

$$F_d = c \frac{\Delta x}{144} \frac{\rho A}{g_c} \frac{\partial u}{\partial t} \quad (19)$$

where:

F_d = damping force, lb

c = damping coefficient, $\frac{1}{s}$

Δx = increment of rod length, ft

ρ = rod material's density, $\frac{lb}{ft^3}$

g_c = gravitational constant, 32.2

A = cross-sectional area of the rod, in^2

$\frac{\partial u}{\partial t}$ = shear velocity between fluid and rods, $\frac{ft}{s}$

The final version of the conventional one-dimensional wave equation for describing the propagation of force waves in sucker rod strings is obtained when the dampening force is substituted into equation (18):

$$\frac{\rho A}{144 g_c} \frac{\partial^2 u}{\partial t^2} = EA \frac{\partial^2 u}{\partial x^2} - c \frac{\rho A}{144 g_c} \frac{\partial u}{\partial t} \quad (20)$$

This formula is valid for variable rod diameters.

The more familiar form of the one-dimensional wave equation is valid for a uniform rod section and viscous damping only. According to [1, pp. 278]: "It is a linear, second-order hyperbolic partial differential equation":

$$\frac{\partial^2 u(x, t)}{\partial t^2} = v_s^2 \frac{\partial^2 u(x, t)}{\partial x^2} - c \frac{\partial u(x, t)}{\partial t} \quad (21)$$

where:

$u(x, t)$ = rod displacement, ft

c = viscous damping factor, $\frac{1}{s}$

$v_s = \sqrt{\frac{144 g_c E}{\rho}}$ = velocity of sound in the rod materials, $\frac{ft}{s}$

x = rod position, ft

t = time, s

[1, pp. 274-278]

Because solving second-order partial differential equations is challenging, other researchers devised a version of the wave equations that resulted in a pair of first-order differential equations. Norton was the first to propose it, followed by Bastian et al.

The wave equation can be solved in two different ways, the diagnostic and the predictive one. The diagnostic approach uses surface measurements to calculate the downhole displacement and forces, whereas the predictive approach makes use of the operation of the sucker rod pump to predict surface conditions.

For both approaches, diagnostic and predictive, boundary conditions must be used and they must represent the physical phenomena at each end of the rod string.

For the predictive approach, two boundary and initial conditions are needed because the conventional wave equation contains second-order derivatives, in time and space. The initial conditions, rod displacements, and velocities are zero.

2.14.1 Diagnostic Analysis

Calculating displacement throughout the length of the rod string for the same values of time is part of the diagnostic analysis. There are no initial conditions necessary in this form of analysis because only steady-state solutions are needed. As a result, the time derivatives of force and displacement do not vary from one pumping cycle to the next. The surface dynamometer card, which provides time histories of the dynamic forces and polished rod movement at $x = 0$, gives the boundary conditions that must be employed. To apply this method the rod string gets divided into several segments Δx . The accuracy increases with an increasing number of segments. Furthermore, time increments, Δt , are also needed. Both of these increments are interrelated and act as a stability criterion:

$$\Delta x \leq \Delta t v_s \quad (22)$$

where:

Δx = length increment, ft

Δt = time increment, s

v_s = velocity of sound in the rod material, $\frac{ft}{s}$

2.14.2 Predictive Analysis

In contrast to the diagnostic model, the predictive analysis also takes into account time. It employs a calculation model that predicts rod displacement. A sufficient number of pumping cycles must be simulated to reach a stable solution since transient solutions also exist. Typically three to five pumping cycles are required to reach a steady-state solution. The rod string is divided into several segments, Δx , just as in the diagnostic method. The time increment, Δt , must meet the criterion specified below for the solution to be stable:

$$\Delta t \leq \frac{\Delta x}{v_s} \quad (23)$$

where:

Δx = length increment, *ft*

Δt = time increment, *s*

v_s = velocity of sound in the rod materials, $\frac{ft}{s}$

Boundary and initial conditions

The boundary and initial conditions at any point(s) along the string must be known to solve any variant of the wave equation. Various input data are required depending on the type of analysis desired:

- Surface displacements and loads versus time provide the required boundary conditions for the diagnostic analysis.
- The boundary conditions for the predictive analysis are given by the polished rod's movement over time and a description of the subsurface pump's operating conditions.

[1, pp. 278, 279, 284-288]

2.15 Computational Fluid Dynamics

The computer-based simulation of systems involving fluid flow, heat transfer, and associated phenomena such as chemical reactions is known as computational fluid dynamics or CFD. The method is quite effective, and it can be applied in both industrial and non-industrial applications.

The numerical methods that can solve fluid flow problems are organized into CFD programs. All commercial CFD software includes sophisticated user interfaces. This provides easy input of parameters as well as simple access to the results. All CFD codes contain three main elements, a pre-processor, a solver, and a post-processor. Figure 19 shows the main steps

necessary to perform a CFD simulation. The pre-processing can be further divided into geometry modeling, grid generation, defining models, set properties, and set boundary and inlet conditions. [9, 10]

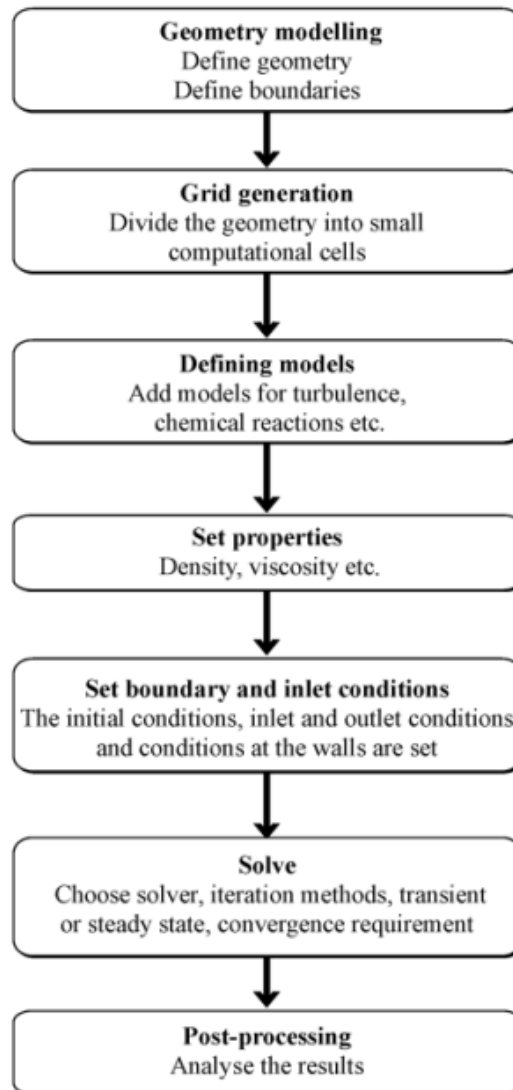


Figure 19: Steps of CFD Simulation [9, pp. 5]

2.15.1 Pre-Processor

The flow problems are put into a CFD program with a user-friendly interface. The input parameters are automatically transformed into a form suitable for the solver. These input parameters are, for example, the definition of the geometry, generation of the grid, implementation of chemical and physical phenomena, different fluid properties, and boundary conditions for cells that are in contact with the domain boundary. The accuracy of the CFD model strongly depends on the mesh, specifically the resolution of the mesh. In general, a finer mesh leads to more accurate solutions but requires more solving power. To reduce the solving

power, non-uniform meshes are preferred. Non-uniform meshes are coarser in areas with little changes and get finer in areas where more variations occur. The implementation of the grid is done by the user and takes more than 50% time of the whole CFD project. To reduce this workload and to make this process more efficient and accurate, CFD codes with self-adapting meshing capabilities are in development. [11, pp. 33-36]

2.15.1.1 Geometry Modeling

The definition and creation of a two-dimensional (2D) or three-dimensional (3D) sketch of the system's geometry is the first step in solving a CFD problem. All commercial CFD packages contain CAD software, although the system geometry can generally be created in any CAD program and then imported into the grid-generation program. [11, pp. 37,38]

2.15.1.2 Grid Generation

The accuracy with which the computational domain is meshed is just as important as the accuracy with which the physical models are defined. Meshing describes the subdivision of the domain into several smaller, non-overlapping, subdomains. Since the equations for momentum transport are nonlinear, the computational volume must be discretized properly to achieve an accurate numerical solution. To avoid errors the mesh's quality must be assessed before the actual simulation begins. The number of cells in the mesh inside the computational domain has a significant impact on the accuracy of a CFD solution. In general, when the number of cells increases, also the accuracy of the results gets enhanced. Furthermore, the accuracy is also affected by other parameters. These include the mesh type and the order of accuracy of the numerical method. The majority of time spent on a CFD project is generally spent developing a mesh for the domain geometry. [11, pp. 39,40]

2.15.1.3 Defining Models

The definition of the model depends on how complex it is. The Navier-Stokes equation can be solved directly for single-phase laminar flow, but for turbulent and multiphase flow a more complex and appropriate model must be chosen.

2.15.1.4 Set Properties

In this step, all fluid properties, physical and chemical, are defined.

2.15.1.5 Set Boundary and Initial Conditions

All boundary conditions are defined in this step. The behavior of fluid flow is complex and has a significant impact on which boundary conditions are relevant.

2.15.1.6 Solver

Due to the complexity and nonlinearity of the underlying physical processes, an iterative solution approach is required. Before a solution for an iterative procedure can be calculated, all discrete values of flow properties must be initialized. The discrete values are velocity, pressure, temperature, and other transport-related parameters. Initial conditions can be purely arbitrary. However, this can lead to problems. If the initial conditions are too far away from the final steady-state solution the iteration process will take longer. Improper initial conditions may also cause the iterative procedure to misbehave, leading to wrong solutions. There are three numerical solution techniques for CFD discretization of the grid and the governing equations, finite difference, finite volume, and finite element. [9, pp. 6,7, 11, pp. 41-46]

2.15.1.7 Finite Difference Method

The finite difference method is the earliest attempt to solve partial differential equations numerically. This method is applied at the grid points and directly to the differential form of the governing equations. The discretization of the derivatives of the flow variables is done by using a Taylor series expansion. The Finite difference method can be applied to any type of grid. However, this approach necessitates a mesh with a high degree of regularity. Therefore, it is typically used on structured grids. Although the grid spacing between the nodal points does not have to be uniform, the amount of grid stretching or distortion applied is limited. Another disadvantage is that the governing equations have to be transformed from the physical to the computational space. [10, pp. 75, 11, pp. 158-162]

2.15.1.8 Finite Volume Method

The most common numerical solution technique for CFD is based on the finite volume method. This method directly discretizes the integral form of the conservation equations in the physical space. The entire computational domain is divided into small contiguous sub-volumes, called cells, to solve the equations numerically. For each control volume, their variable values are determined at their center. Variable values at the control volume surface are expressed in terms of the center values using interpolation, and suitable quadrature equations are employed to estimate the surface and volume integrals. For each of the control volumes, an algebraic equation can be found. The finite-volume method can handle any form of grid since it works with control volumes rather than grid intersection points. Unstructured grids, rather than structured grids, can be used to define the shape and location of the control volumes, allowing for a wide range of possibilities. In two dimensions, the mesh can be constructed with a combination of triangles or quadrilaterals, while in three dimensions, tetrahedra and hexahedra combinations are used. This type of unstructured mesh provides more versatility when it comes to dealing with complicated geometries. Since these equations are solved numerically in an

iterative manner, a numerical error is introduced. After a solution has been obtained, it is critical to control the magnitude of the error. The error can be diminished by substantially reducing the cell size. Reducing the cell size too much, on the other hand, yields an excessively huge number of cells, resulting in increasing computing effort and simulation time. [9, pp. 25-29, 11, pp. 163-168, 12, pp. 103, 104]

2.15.1.9 Finite Element Method

In many aspects, the finite element approach and the finite volume method are similar. The finite element method was first developed as an engineering procedure for obtaining stress and strain displacement solutions in structural analysis. Both methods, finite volume, and finite element are suited for irregular computational domains.

The finite element method starts with subdividing the physical space into discrete elements. This is called discretization. The flow problem's solution can be discovered on specified points at the element's boundaries and/or inside it. The number of points governs the accuracy of the model. To interpolate between the discrete values obtained at the mesh nodes, so-called shape functions have to be defined. The value of the shape-functions outside its corresponding element is zero, and are linear or higher-order distributed inside the element. The differential form of the governing equations must be transformed into an equivalent integral form. This makes it possible to simulate discontinuities such as shock waves. The approach of weighted residuals or weak formulation can be used to achieve this task. The residuals represent an error and it is required that their weighted average is zero over the domain. The integral formulation of the finite-element method, as well as the usage of unstructured grids, make it appealing for flows in or around complex geometries. The method is especially well suited to the treatment of non-Newtonian fluids. The finite element method, particularly for elliptic and parabolic problems, has a fairly accurate mathematical foundation. Although the method may be proven to be mathematically equivalent to finite-volume discretization in some cases, the numerical effort is significantly higher. [11, pp. 168, 13, pp. 29, 30, 14, 15, pp. 43-50]

2.15.2 Post-Processor

The primary goal of post-processing is to determine the solution's quality. Validation of the CFD code is inevitable. Are the grid size, convergence criterion, and numerical methods all independent of the solution? The final simulation results will then be analyzed to provide local information on flow, concentrations, temperatures, and reaction rates, among other things. Although the results are not particularly precise for highly complicated systems, CFD is a powerful problem-solving tool and time-saving addition to laboratory experiments. [9, pp. 7]

2.15.3 Arbitrary Lagrangian-Eulerian Formulation (ALE)

The model simulates the downhole pump by focusing on the dynamic coupling between the standing valve and the traveling valve, both are ball check valves. The computational domain of the model equals the two valves and the chamber between these valves. Due to the plunger movement, this volume expands or contracts. Any preset kinematics of the TV, as well as the hydrodynamic pressure at the domain's inlet and outlet, representing the pump intake pressure and tubing pressure, may be imposed as inputs. The balls in the valve cages have a certain amount of freedom to move up and down within the valve cage. The weight of the balls and the hydrodynamic forces acting on them governs their movement. The model assumes laminar and incompressible flow. The fluid is supposed to be a single phase with homogeneous physical properties and Newtonian. The pump materials' elastic deformations are assumed to be negligible. The model uses a moving/adapting mesh to account for the change in the size of the chamber. This is done by using the ALE method.

The Lagrangian formulation is suited for structural dynamics whereas the Eulerian formulation is suited for fluid dynamics.

The equation of motion is expressed in a material domain in the Lagrangian formulation. A grid tracks the motion of the system. The grid deforms as the system moves. This formulation is used for structures that are enduring considerable displacements as long as the grid deformation is limited.

Compared to the Lagrangian formulation, the equation of motion is expressed in a spatial domain in the Eulerian formulation. The system moves through a fixed grid. Therefore, this formulation is especially well suited to describing fluid flows.

The ALE formulation combines the benefits of both, the Lagrangian and the Eulerian method, to couple fluid-structure interactions (Figure 20). It allows the mesh geometry to be controlled independently of the material geometry. Large fluid-structure interface deformations can be easily handled. The structural motion is adjusted using a Lagrangian dominated approach, while the fluid flow physics is handled using an Eulerian dominated approach.

For only small transformations, the Lagrangian and Eulerian formulations, both lead to the same result. [16, pp. 1, 2]

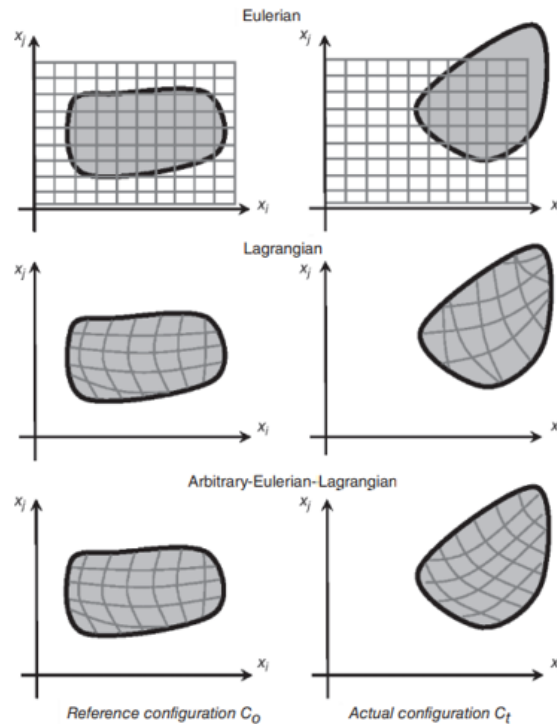


Figure 20: Eulerian, Lagrangian and Arbitrary Lagrangian-Eulerian Formulations [17, pp. 16]

2.15.4 Inductive Sensor

The most extensively used sensors are resistive, capacitive, inductive, and magnetic (RCIM) sensors, which account for more than 70% of the sensor industry today. They are the first option in many sensor designs and applications due to their simple concepts, robust properties, simple electrical circuits, low cost, and mature design and production capabilities. RCIM sensors are used in a variety of applications, including environmental protection, home automation, health care, aviation, as well as the food, chemical, and medical industries, to measure pressure, humidity, acceleration, flow rate, radiation, electrical current, electric and magnetic fields, or chemical and biological substances. When a physical, chemical, or biological stimulus is applied to an RCIM sensor, it causes a change in electrical resistance, capacitance, inductance, electrical field, or magnetic field. To represent these changes, the output can be a voltage, current, electrical charge, time, or frequency.

The working principle and characteristics of an inductor are used to construct inductive sensors. They're mostly used to measure electric and magnetic fields, as well as other physical properties (such as displacement and pressure) that may be converted to an electric or magnetic response. Inductive sensors do not require physical contact, making them noncontact sensors that are especially beneficial in applications where access is a problem. Only metals can be detected by inductive sensors. Distinct metallic materials, such as steel, copper, and aluminum, have

different responses. As a result, they may be utilized to distinguish between various metals. Inductive sensors, unlike capacitive sensors, are unaffected by nonmetallic media components between the probe and the target, making them well-suited to harsh environments including oil, dust, dirt, or other contaminants.

The main advantages of inductive sensors are listed below:

- fast response
- robustness
- easy handling
- high reliability
- nearly infinite resolution
- large operating temperature range

An inductor is a type of electromagnetic component that links electrical and magnetic fields. Inductive, magnetic, and electromagnetic sensors are all designed using a variety of electromagnetic principles. Although there is no clear distinction between inductive, magnetic, and electromagnetic sensors, inductive sensors include air coils, eddy-current sensors, and variable reluctance sensors, which are generally comprised of simple inductive coils. [18, pp. 1,2]

2.15.4.1 Inductors

A passive electrical or electronic component that resists current changes is known as an inductor. The voltage-current relationship of an inductor is governed by:

$$V = L \frac{dI}{dt} \quad (24)$$

where:

V = voltage across the inductor, V

L = inductance, typical range $1\mu\text{H} - 0.1\text{H}$, H

I = current, A

An inductor can store energy as well. In or around the inductor, energy is stored as a magnetic field. An inductor's stored energy (measured in joules, J) is equal to:

$$U = \frac{1}{2} LI^2 \quad (25)$$

Inductor in parallel:

$$L_{eq} \sum L_i \quad (26)$$

Inductor in series:

$$\frac{1}{L_{eq}} \sum \frac{1}{L_i} \quad (27)$$

where:

L_{eq} = resultant (equivalent) inductance, H

Wire-wound (air) inductors, radial inductors, chip inductors, and power inductors are the different types of inductors (Figure 21).

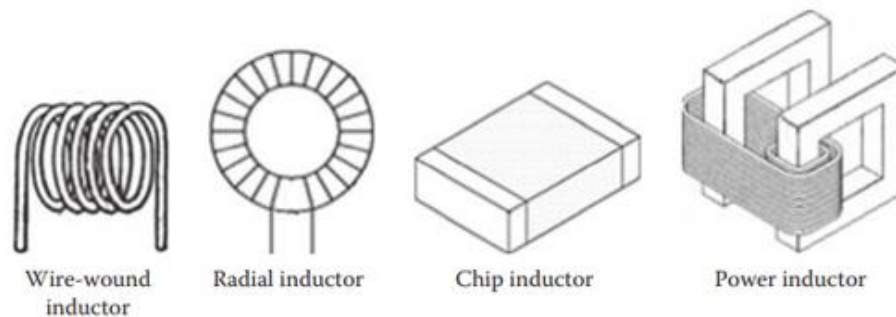


Figure 21: Inductor Types

Magnetic energy storage, electric motors, transformers, and sensors are among their most common uses. Fixed, variable, and adjustable inductors are all types of inductors. The coil turns in fixed inductors stay constant. Variable inductors allow for a change in effective inductance by moving an iron or ferrite core inside the coil (Figure 22).

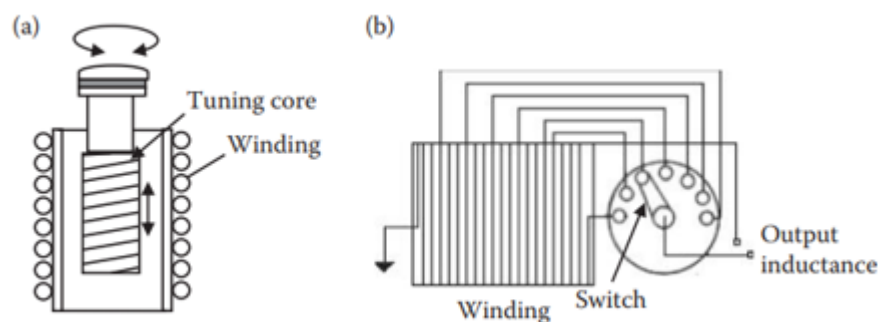


Figure 22: Adjustable Inductor (a) and Variable Inductor (b)

The inductance increases or decreases in proportion to how far the core has moved into the coil shape. These types of inductors are called slug-tuned inductors. Adjustable conductors can be constructed in two different ways. One is that they consist of multiple fixed conductors that can

switch into different serial or parallel combinations. And the second one is that they are made of several fixed inductors, allowing for adjustment of the required turns [18, pp. 153-155]

2.15.4.2 Inductance and Magnetic Field

A magnetic field, and therefore, magnetic flux around the circuit is created when current travels through a conductor. The magnetic flux to current ratio equals the inductance:

$$L = \frac{\Phi}{I} \quad (28)$$

where:

Φ = magnetic flux, *Wb*

The magnetic field can be described in two ways, by the magnetic flux density of the magnetic field strength:

$$B = \mu H = \mu_0 \mu_r H \quad (29)$$

where:

B = magnetic flux density, *T* or $\frac{Wb}{m^2}$

H = magnetic field strength, $\frac{A}{m}$

μ_0 = permeability in a vacuum, $\frac{H}{m}$

μ_r = relative permeability

The permeability of a material is its ability to form a magnetic field within itself. [18, pp. 155, 156]

2.15.4.3 Physical Laws and Effects governing Inductive Sensors

2.15.4.3.1 Lorentz Force

The so-called Lorentz force acts on an electron, or electric current, when it moves or flows, through a magnetic field, respectively:

$$\vec{F} = q\vec{v} \times \vec{B} \quad (30)$$

where:

\vec{F} = Lorentz force, *N*

q = charge of an electron ($1.602 \cdot 10^{-19}$), *C*

\vec{v} = velocity of the electron, $\frac{m}{s}$

\vec{B} = magnetic field flux density, T

The origin of the Lorentz force comes from the interaction, which can either be attraction or repulsion, between the magnetic field and the external magnetic field \vec{B} . The magnetic field is generated by a moving charge, for example, an electron. The right-hand rule can be used to determine the direction of the Lorentz force for a given current and magnetic field.

2.15.4.3.2 Faraday's Law of Electromagnetic Induction

A voltage or current can be induced in a conductor when a changing magnetic field passes through this conductor. This does only work for a closed loop. This induced voltage is then called electromotive force (EMF).

The induced voltage, for a straight wire or a one-loop wire, is:

$$V_L = -\frac{d\Phi}{dt} \quad (31)$$

where:

V_L = induced voltage, V

Φ = magnetic flux, Wb

$\frac{d\Phi}{dt}$ = rate of change in the magnetic flux, $\frac{Wb}{s}$

The induced EMF produces a current that goes in the opposite direction to the original flux change, indicated by the negative sign.

The induced voltage, for an N-loop coil, is:

$$V_L = -N\frac{d\Phi}{dt} = -NA\frac{dB}{dt} = -\mu NA\frac{dH}{dt} \quad (32)$$

where:

A = area of the coil

N = number of turns

The motional EMF, where the EMF is generated by a moving wire in a magnetic field, is:

$$V_L = -\frac{d\Phi}{dt} = -\frac{BdA}{dt} = -\frac{Blvdt}{dt} = -Blv \quad (33)$$

where:

l = wire length, m

v = velocity of the moving wire, $\frac{m}{s}$

$lvdt$ = area that is swept out by the wire in the time interval dt

2.15.4.3.3 Biot-Savart Law

The Biot-Savart law relates the generated magnetic field with a steady current that flows through a closed loop:

$$\vec{B} = \frac{\mu I}{4\pi} \oint \frac{d\vec{l} \times \vec{r}}{r^2} \quad (34)$$

where:

\vec{B} = magnetic field generated

$d\vec{l}$ = integration element of length l along the current path

\vec{r} = position vector,

It points from the element $d\vec{l}$ to the field point at which the magnetic field \vec{B} is calculated.

2.15.4.3.4 Ampere's Law

Ampere's law, one of the four Maxwell equations, relates the magnetic field to an electric current:

$$\oint \vec{B} * d\vec{l} = \mu I \quad (35)$$

where:

\vec{B} = magnetic field

I = electric current

$\oint \vec{B}$ = integration along a closed path

$d\vec{l}$ = infinitesimal element along the integration path

By utilizing Ampere's law, a current can be determined with a given magnetic field or vice versa.

2.15.4.3.5 Magnetomotive Force

When current flows through a coil of wire, the magnetomotive force generates a magnetic field. The magnetomotive force is equivalent to the number of turns of wire carrying an electric current. The magnetomotive force increases with an increasing number of turns of wire in the coil or with increasing current through the coil and is calculated by:

$$\mathfrak{F} = \oint H dl = NI \quad (36)$$

Magnetomotive force is measured in ampere-turns, $A - t$.

According to [19], “One Ampere-turn is the amount of magnetic force or flux produced when one ampere flows through a single turn of an electrical conductor.”

2.15.4.3.6 Eddy Current

An Eddy current is an electromagnetic phenomenon that leads to energy losses that appear as an increase in the electrical resistance of the coil. This increase in electrical resistance happens because eddy currents take energy from the coil. Furthermore, they generate their magnetic field opposing the coil’s magnetic field. The loss due to eddy currents is calculated by:

$$P_E = K_E B_{max}^2 f^2 t_h^2 V_{vol} \quad (37)$$

where:

K_E = constant that depends on the electrical resistance of the conductor

B_{max} = maximum flux density, $\frac{Wb}{m^2}$

f = frequency of magnetic reversals, Hz

t_h = thickness of laminations, m

V_{vol} = conductor volume, m^3

2.15.4.3.7 Skin Effect and Proximity Effect

The skin effect only occurs in the presence of a single conductor. Compared to the proximity effect, which is present when two or more conductors are at close distance to each other. Conductor resistance rises as a result of both of these phenomena, especially at high frequencies. These effects happen when current dispersion is unequal over a conductor's cross-section, or when two conductors are near to each other, resulting in a rise in flux density. When the current of two conductors faces in the same direction, the effect increases and the percentage

of current in distant areas also increases. The current density in close proximity is higher when the current flows in opposite direction. [18, pp. 159-168]

2.15.4.4 Inductive Sensor Materials

The coil and core materials, coil turns, coil form, and excitation frequency all have an impact on the characteristics of an inductive sensor.

2.15.4.4.1 Coil Materials

The most common material used is copper.

2.15.4.4.2 Core Materials

Core materials can be either ferromagnetic materials or nonmagnetic materials. Ferromagnetic materials, such as crystalline metals, alloys, and ferrites, provide an easy path for flux. Nonmagnetic materials act as a support for the wound metal wires by increasing the stiffness of the coil.

2.15.4.4.3 Housing Materials

Metals or plastics are used as housing materials for inductive sensors. The selection of the housing materials is important since they have to be compatible with the surroundings.

2.15.4.4.4 Target Materials

Two types of target materials are available, ferrous and non-ferrous. Non-ferrous metals are not detected by all inductive sensors. Each target material has a specific inductive effect, which is generally less than pure iron. Therefore, calibration is required before the measurement. Correction coefficients are utilized as a result. Cast iron, carbon steel, and stainless steel are examples of ferrous target materials. Aluminum, beryllium, copper, magnesium, and zinc are examples of non-ferrous target materials. [18, pp. 168-173]

2.15.4.5 Inductive Sensor Operating Principle

Inductive sensors are available in a variety of shapes and sizes, but they all share the same operating principle. An alternating magnetic field is created by a coil (inductor) carrying an alternating current (AC). The secondary magnetic field can be formed in different ways. A permanent magnet connected to a moving item, eddy currents induced by the inductor in a nearby conductive target, or current flowing in the secondary coil caused by the inductor. In

addition, the induced secondary magnetic field always has to fulfill one additional criteria, pointing in the opposite direction than the magnetic field of the source. An evaluating circuit can be used to measure changes in inductance or impedance.

An inductive sensor must meet certain requirements in order to function. A coil, an oscillator to generate and emit a high-frequency alternating current, and an electrically conductive or magnetically permeable item are all required components of an inductive sensor. Further requirements are an output circuit and a sensing or measuring circuit. The output circuit must have the ability to amplify, condition, interpret, or convert the detected signal to an appropriate output, and the sensing or measuring circuit is needed to measure the change in the magnetic field. When a conductive sensor meets all of the aforementioned requirements, it is referred to be a self-contained sensor (Figure 23).

By design, inductive sensors have a limited sensing range, the magnetic field is limited. The overall inductive sensors performance depends on proper mounting and good isolation of sensor-own conductive material. The sensor should not interact with any conductive materials other than the target material. [18, pp. 178, 179]

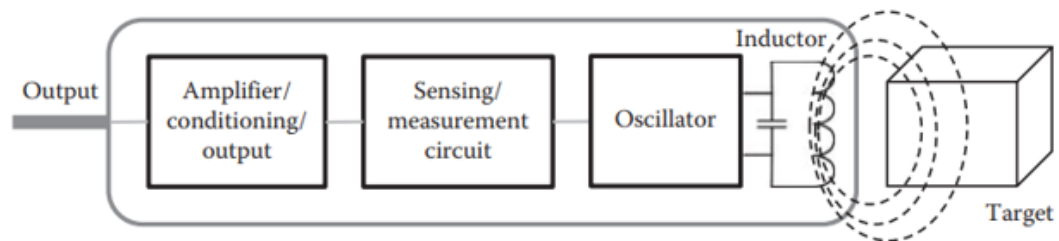


Figure 23: Self-Contained Inductive Sensor Basic Structure [18, pp. 179]

2.15.4.6 Inductive Sensors with Ferromagnetic Cores

In comparison to air coil sensors, coil sensors with a ferromagnetic core offer better sensitivity and permeability, but they are less stable, have more energy loss, and are nonlinear. These sensors are frequently employed in applications that require high sensitivity or have space constraints. These sensors consist of a magnetic core. A magnetic core is a magnetic material that offers high permeability. This high permeability enables that within the core material, magnetic fluxes can be confined, guided, and concentrated. The core is either made out of ferromagnetic compounds like ferrites, or ferromagnetic metals like iron. A current-carrying coil of wire creates a magnetic field around the core. When comparing the magnetic field of a coil with and without a magnetic core, it can be seen that the implementation of a magnetic core increases the magnetic field by a factor of thousands.

2.15.4.6.1 Ferromagnetic Core Design

There are several options for the design of ferromagnetic cores available with their own advantages and limitations. E-shaped cores offer the highest symmetry and provide a closed magnetic loop. C- and U-shaped cores are also closed-loop but have lower symmetry than E-shaped cores. The planar core is the most simple version, offering high-power, small-volume transformers at a low cost. In most applications, the magnetization of the core should decrease when the applied magnetic field is removed to reduce hysteresis, and therefore, energy loss. [18, pp. 184-186]

2.15.4.7 Inductive Proximity Sensor

This type of sensor is used to detect a conductive object in front of the sensor. An electromagnetic field is created by an oscillating current flowing through a coil wound around an iron core in this type of sensor. The inductive proximity sensor has a magnetic field. When a magnetic or conductive object, for example, a metal plate, is placed within this magnetic field, the inductance of the coil changes. The detection circuit of the sensor recognizes this change and generates an output voltage representing the result. [18, pp. 190]

2.15.4.8 Signal Processing of Inductive Sensors

To determine how far the target is away from the sensor, a trigger circuit measures the change in amplitude. The underlying principle is that currents are induced and circulated within the target when a metal target enters the sensor's magnetic field. The electromagnetic field's amplitude gets reduced due to a load put on the sensor. [18, pp. 190]

Chapter 3

Test Setup

3.1 Pump Test Facility

The experiments were conducted at the University of Leoben's Pump Test Facility (PTF). Field testing is both costly and time-consuming. The PTF allows for near-field testing, which saves money and time because different operational parameters can be changed quickly. As a result, the PTF serves as a vital link between laboratory measurements and real-world applications.

3.1.1 Pump Jack

A standard pump jack cannot be installed in the PTF due to space constraints. Therefore, several modifications are made to imitate real-world conditions. Instead of a standard pump jack, a spindle driven by a linear servo drive is employed. Attached to the spindle is a skid that can move upward and downward. It is controlled by an electronic velocity-, torque-, and position system.

The spindle is driven by an asynchronous motor with variable speed drive and moves the skid upwards and downwards. The polished rod is attached to the skid. Due to spatial limitations; the shaft is 10 [m] deep; the polished rod is directly connected to the plunger. With these components, linear servo drive, variable speed drive, spindle, skid, and polished rod the movement of a standard pump jack can be simulated. Within the range of 0 to 10 strokes per minute (SPM), the variable speed drive provides either linear or sinusoidal velocity profiles.

To reproduce a wider variety of real-life scenarios, the sucker rod pump in the PTF can be inclined up to 30°. The pump intake pressure is provided by a compressor, this simulates the reservoir pressure. The discharge pressure is controlled by a valve. The pump can output up to 13 [m³/h] and can handle a 9 [bar] intake pressure.

Simulating operational conditions up to 500 m pump setting depth is possible. The fluid temperature can also be changed to a maximum of 60 [°C]. The pump and fluid are operating at ambient temperatures, with a small but not substantial temperature increase seen during the experiments.

3.1.2 Pump Specification

The pump used is a rod insert pump, 30-225 RHAC. The pump designation reads as follows:

- 30 nominal tubing size, *in*
- 225 nominal pump bore size, *in*
- R type of pump, R stands for insert
- H type of barrel, H stands for heavy wall
- A location of seating assembly, A stands for top
- C type of seating assembly, C stands for cup

[20]

3.1.3 Valve Rod and Barrel Specification

The valve rod has a length of 3 [m], and the plunger measures 4 [m] in length. The valve rod is directly connected to the plunger due to space constraints.

3.2 Simulation

The goal of this thesis is to validate a sucker rod pump fluid simulation. All data related to the CV-SRP simulation model is provided by AC2T research GmbH. The relevant data for the validation is acquired in the PTF during tests under various conditions. The following chapter describes the setup, considerations, assumptions, and simplifications of the simulation.

The main aim of the simulator is to optimize the pump design of an SRP and its operation. This is done by verifying the simulation data with the data gathered from the PTF measurements. The simulation uses a coupled sucker rod pump (CV-SRP) model. This CV-SRP model can be used to identify the proper ball material and the geometry of the cage for the standing valve specific to the operating conditions. There is still a discrepancy between the simulation results and the measured data. This will be discussed later.

The output of the simulation can be described in one number, the Optimum Valve Number (OMV number). This is a dimensionless number depending on the material of the ball, ball density, and the plunger speed. Two different cases are examined, a 3D stationery and a 2D

transient. The 3D stationary case is used to study the impact of the valve cage geometry. A full 3D flow can be simulated. Geometrical parameters such as diameter, length, and the number of holes in the valve housing can easily be changed. With this, the behavior of new geometry can be predicted.

The 2D transient case is used to predict the Optimum Valve Number (OMV number), which is based on the square-root law, and to predict the phenomenon of mid-cycle valve closing. [21]

3.2.1 3D Stationery Case

Inductive sensor readings provide steady-state information. The critical plunger speed is the most crucial parameter. The critical plunger speed is the speed at which the standing valve opens entirely. The OMV number is validated using this information. As previously stated, there is a discrepancy between the measurements and the simulation results. Model enhancement studies are carried out to further analyze this deviation. This includes turbulence analysis, transverse oscillation analysis, swirl flow analysis, and slippage leakage analysis.

3.2.1.1 Turbulence

The presence of turbulent flow can be characterized by utilizing the Reynolds number. The flow gets unstable at increasing Reynolds numbers, reaching a transition zone before becoming turbulent. This transition zone is relatively small. For pipe flow, a typical Reynolds number is around 2000-2300. The main characteristics of turbulence are listed below.

3.2.1.1.1 Disorder

Turbulent flows are disorganized or irregular. Fluid particles appear to flow around in a chaotic, 'random' manner. This property of turbulence is so important to its definition that no matter how carefully the boundary conditions are reproduced, the flow will never repeat itself in the same way. To put it differently, turbulence is extremely sensitive to initial and boundary conditions, almost as if it had a memory. The nature of turbulence led to the conclusion that it is a random phenomenon and that turbulence can only be analyzed by using statistical methods.

3.2.1.1.2 Diffusive

Turbulent flows are diffusive. The molecular diffusion effect causes diffusion in a stationary fluid. Turbulence accelerates the diffusion or mixing of quantities by making any inhomogeneity existing in a flow more susceptible to the effects of molecular diffusion. Turbulence diffusion helps a fluid flow's momentum, mass, energy, and any other inhomogeneity to mix better.

3.2.1.1.3 Dissipative

Turbulent flows dissipate energy, which implies they 'transform' energy. The Reynolds number governs whether or not a flow is turbulent, but when turbulence occurs, the Reynolds number has minimal impact on large-scale motion or the motion of large eddies. In other words, the small-scale eddies get finer with increasing Reynolds number. The formation of large eddies or vortices in a turbulent flow converts some of the energy in the main flow to turbulent energy. Large eddies break into smaller and smaller ones, carrying the turbulent energy with them. Large eddies also carry small eddies with them, causing them to overlap in space. The energy is dissipated through viscosity into heat as the break-down process continues. This is known as the concept of energy cascade.

3.2.1.1.4 Continuum

Turbulence is a three-dimensional, time-dependent continuum phenomenon. The Navier-Stokes equations govern turbulent flows at all points in the flow's domain. When time averages of flow quantities are taken into account, the turbulent flow can be considered two-dimensional. Regardless of how small the eddies become as a result of turbulent dissipation, they remain substantially larger than the fluid's molecular length scale.

3.2.1.1.5 Multiple Length- and Time-Scales

Turbulent flows have a wide range of length and time scales. Therefore, turbulent flows have many degrees of freedom. This makes turbulence problems hard to solve.

3.2.1.1.6 Source

Shear flow and/or buoyancy force can both cause turbulence. The flow becomes unstable and vortices form when shear stress is high. The velocity gradient is considered to be the most important source of flow instabilities and hence turbulence.

The turbulence model used in the simulation is the k-omega model. It is part of the Reynolds-averaged Navier-Stokes (RANS) family of turbulence models, which simulates all turbulence effects. It's a model with two equations. The k-omega model can simulate all turbulence effects and consists of two types of equations, two transport equations, and conservation equations. The conservation equations account for history effects such as convection and diffusion.

[22, pp. 7-12]

3.2.1.2 Transverse Oscillation

Transverse oscillation refers to the horizontal movement of the ball. This effect could not be seen in the test rig.

3.2.1.3 Swirl Flow

Swirl flow can be described using the Magnus Effect. When a rotating object moves through the air, part of the air is dragged along with it. As viewed from the object's point of view, air rushes by on all sides. The airflow gets reduced on the side of the object that is turning into the air, whereas the drag on the opposite side speeds the object up. This forces the object towards the location of the low-pressure region. On this side, the airflow is increased, by increasing pressure on the side where the airflow is reduced. [23]

3.2.1.4 Slippage Leakage

The sucker rod pump design requires careful consideration of pump clearance. The clearance is the space between the inside diameter of the pump barrel and the outside diameter of the plunger. Even when the traveling valve is closed, liquid slips through the clearance into the void space between the standing valve and the traveling valve. Pump slippage increases as pump speed increases. However, higher pump efficiency is achieved with higher pumping speeds since the pump displacement increases faster than the pump slippage. [24]

3.2.2 2D Transient Case

With this method, the mid-cycle valve closing can be predicted using an artificially generated pump card. This pump card is applied to both, the test rig and the simulation. The valve opening time agrees with the test rig measurements.

3.3 Test Methodology

3.3.1 Movement Measurement

The movement of the ball from the standing valve is tracked using two inductive sensors. Each inductive sensor can measure a certain distance. The data from both sensors are then combined to show the entire movement of the ball. For the inductive sensors to work properly, the standing valve's housing is made of Plexiglass, as they respond to metal or ferric materials. Any data divergence or inaccuracy caused by extraneous metal components is eliminated as a result. Since Plexiglass cannot withstand as much force as steel, the force with which the Plexiglass housing is screwed into the casing is restricted. Therefore, during assembly, a specific glue is used to ensure that no leaks occur. A small amount of leakage, however, is unavoidable (Figure 24).



Figure 24: Valve Housing Plexiglass

3.3.2 Flow Rate Measurement

A load cell is used to measure the flow rate. The load cell is mounted to an overhead crane. A tank with a capacity of 100 [l] is installed at the bottom of the load cell. Since water is produced directly into the tank, it must be emptied after a few pumping cycles. As the weight increases, the load sensor's force increases. Using this increase in force, the average flow rate for a particular pumping velocity is calculated (Figure 25).



Figure 25: Flow Rate Measurement Setup (left) and Load Cell with Tank (right)

The output of the load sensor is plotted over time to calculate the flow rate. A line equation is applied over a few pumping cycles for a specific pumping velocity. The slope of this line equation is generated using Excel. This gives the average flow rate for a specific pumping velocity. Figure 26 displays how the data is recorded. The left side shows the measurement of the load sensor in [N] and the right side displays the position of the plunger in [mm].

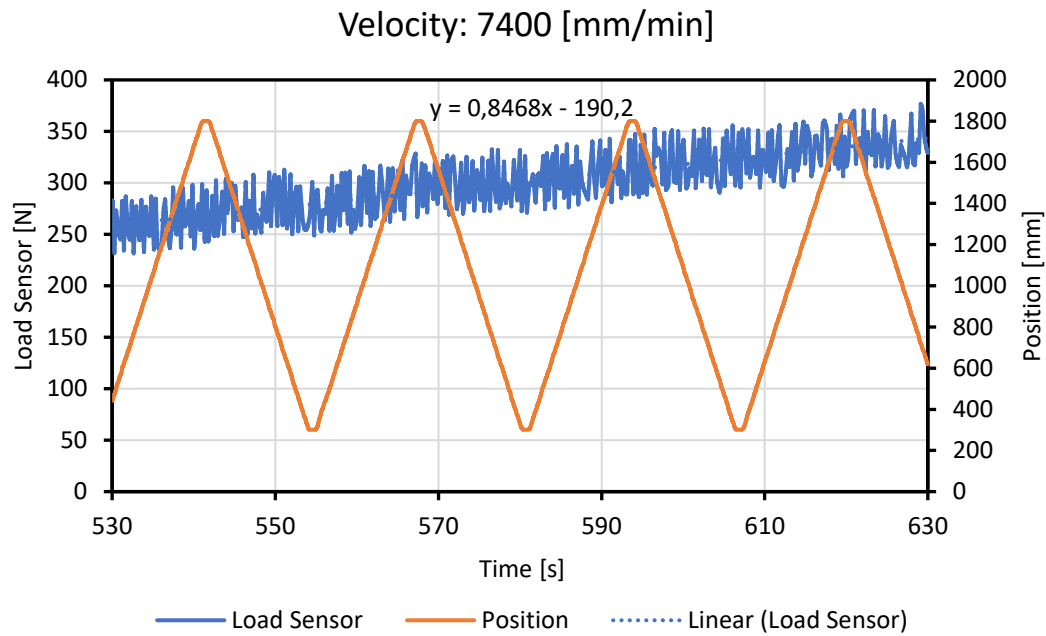


Figure 26: Flow Rate Measurement Example

3.3.3 Calibration

The plexiglass housing and both inductive sensors are calibrated before the experiments since both sensors output the signal in mA. The ball is pushed from the bottom of the housing up to the uppermost position gradually using a thread-rod with an M8 metric thread. One full rotation equals 1.25 [mm], used for distance conversion. Using zip ties, an angle plate is attached to the bottom of the housing to support the thread rod (Figure 27). Two different ball weights are used in each experiment. As a result, the standing valve is dismantled multiple times before the balls can be replaced. A new calibration is necessary after each disassembly to guarantee that the sensors give a proper reading and that the data is converted correctly.



Figure 27: Valve Housing Plexiglass Calibration

3.4 Problems and Technical Difficulties

Several technical issues and difficulties arise during the tests. These include concerns with the inductive sensor's positioning on the housing, minor deviations from the ball's "zero-position" during calibration, noise in the data, and fluid flow measurement inaccuracies.

3.4.1 Sensor Placement

Two inductive sensors are employed in the tests to cover the whole distance that the ball moves inside the housing. There is, however, a small area where neither of the inductive sensors receives a signal from the ball. This area is located between the two sensors, at the upper end of the lower sensor's detecting range and below the upper sensor's sensing range. This gap, however, is quite small, in the range of 1 [mm] to 2 [mm], and because the valve's typical opening behavior has a steep shape, it has little effect on the measurement. Furthermore, due to the sensors' placement, there is a divergence in the sensors' sensing range. The sensors can still be bent at a limited degree after being plugged in, altering the area the sensor covers.

3.4.2 Calibration

There are always some variances present due to the nature of how the calibration is done, namely manually. In terms of identifying the lowest and uppermost positions of the ball in the housing, the calibration isn't 100% precise. As a result, the majority of the data indicate a 1 [mm] divergence from the ball's initial position.

3.4.3 Noise

The data contains a lot of noise. This manifests itself in the form of unstable readouts with numerous spikes. The noise is mostly caused by the ball moving in a horizontal direction. In addition, the ball rotates in an arbitrary direction, and chattering sounds can also be observed.

3.4.4 Fluid Flow Measurement

A load cell is used to measure fluid flow, as previously stated. Because various factors influence its accuracy, this is a quantitative rather than qualitative measurement. First, the load sensor is mounted to an overhead crane, and small vibrations in the facility cause the tank hanging on the load cell to wobble slightly. The load cell's readout is affected by these small vibrations. Furthermore, the load cell's precision is restricted. Slight variations in pumping velocity, for example, do not show up in the results.

Chapter 4

Results and Discussion

4.1 Results Section

The first result after every measurement is from the calibration. An example of the recorded data is shown in Figure 28.

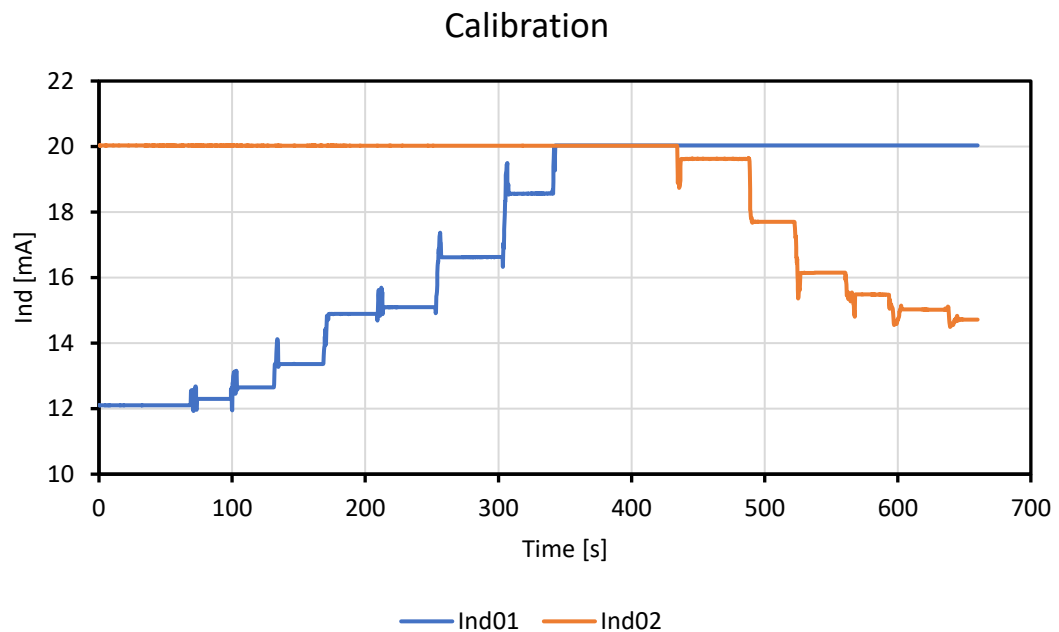


Figure 28: Calibration Result Example

The lower inductive sensor's output signal (Ind01) is represented by the blue line, while the upper sensor's output signal is shown by the orange line (Ind02). Both sensor outputs are recorded in [mA] and plotted over time. During the calibration, each step in the diagram represents a full rotation of the M8 metric thread rod. After several rotations, the lower sensor reaches its maximum reading distance, while the higher sensor continues. Although the ball is

pushed in the upward direction, the signal from the upper sensor decreases stepwise. This is due to the curvature of the ball. Inductive sensors measure the distance to a metal surface, in this case, in the horizontal direction.

In the next step, a polynomial match is applied to convert the output data in [mA] to the actual movement of the ball in [mm]. This gives two polynomial equations, one for the lower sensor and one for the upper sensor. The lower sensor output data is represented in blue and the upper sensor output data is represented in orange. The distance [mm], the ball travels, is plotted over the inductive sensor's output in [mA]. An example of the sensor output data is shown in Figure 29.

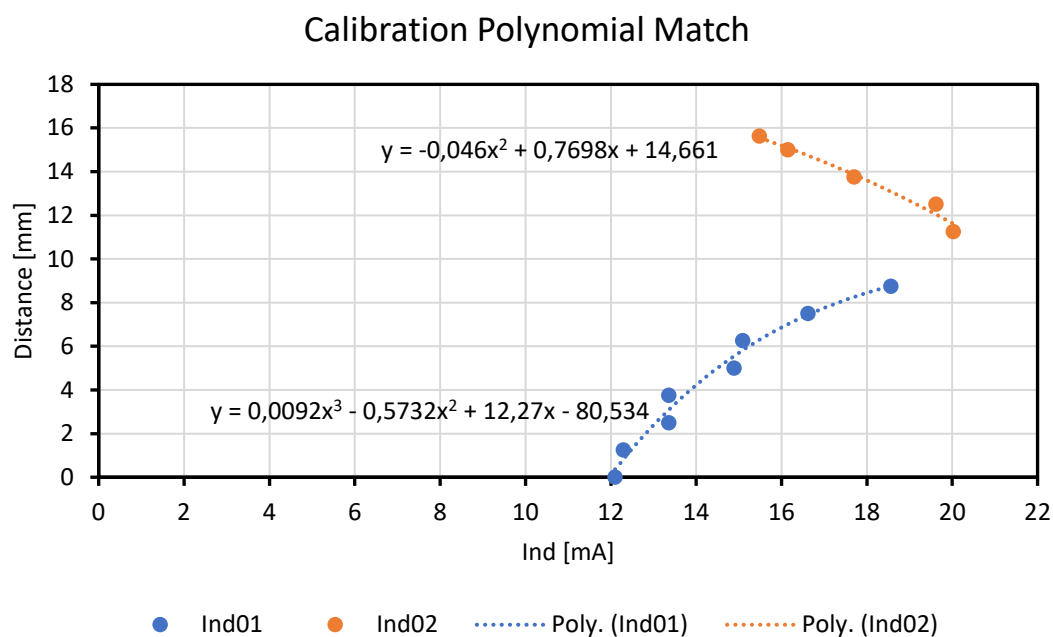


Figure 29: Calibration Polynomial Match Example

Figure 30 shows the unedited sensor output data. The electrical current measured by the inductive sensor in [mA] is plotted over time [s]. Since this does not give any indication of the true position of the ball the data is converted with the previously mentioned calibration. As one can see, there is a lot of noise in the data, this is due to the clearance between the ball and the housing resulting in horizontal movement of the ball. Therefore, an average of every stroke is taken as the sample value.

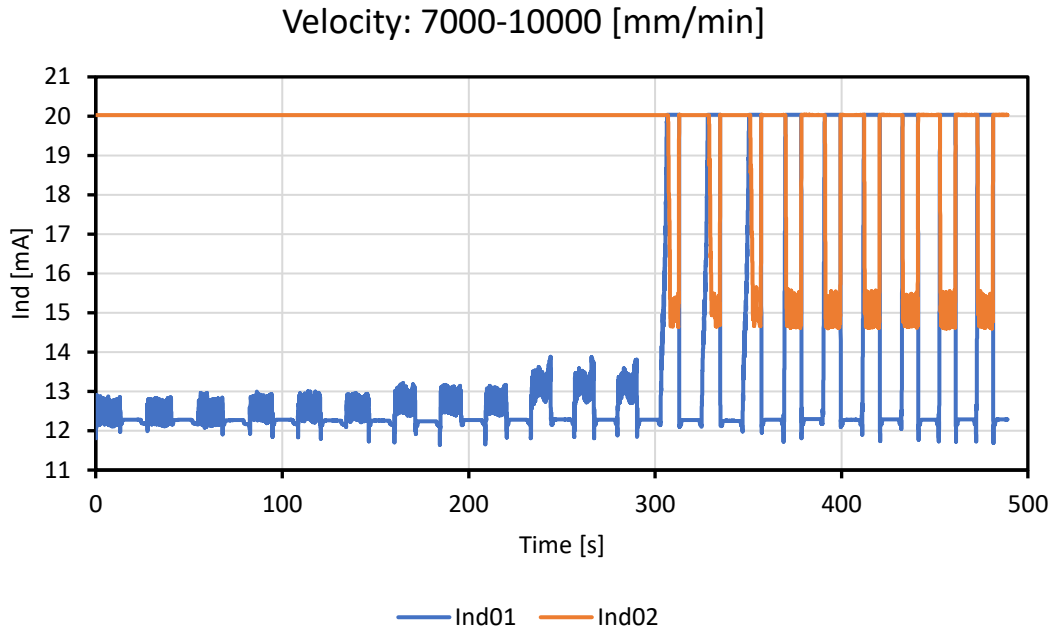


Figure 30: Sensor Output Unedited Example

This then results in the actual distance in [mm] the ball travels, displayed on the left side in Figure 31. On the right side, the velocity in [mm/min] is shown. Both are plotted over time [s]. The grey line, representing the plunger velocity profile, has a trapezoid shape. It also shows that the plunger maintains a constant velocity during the pump's up and down strokes. The plunger's velocity is zero at the top and bottom of each stroke, resulting in a velocity profile that is not constant. The data is recorded with a step size of 0.04 [s].

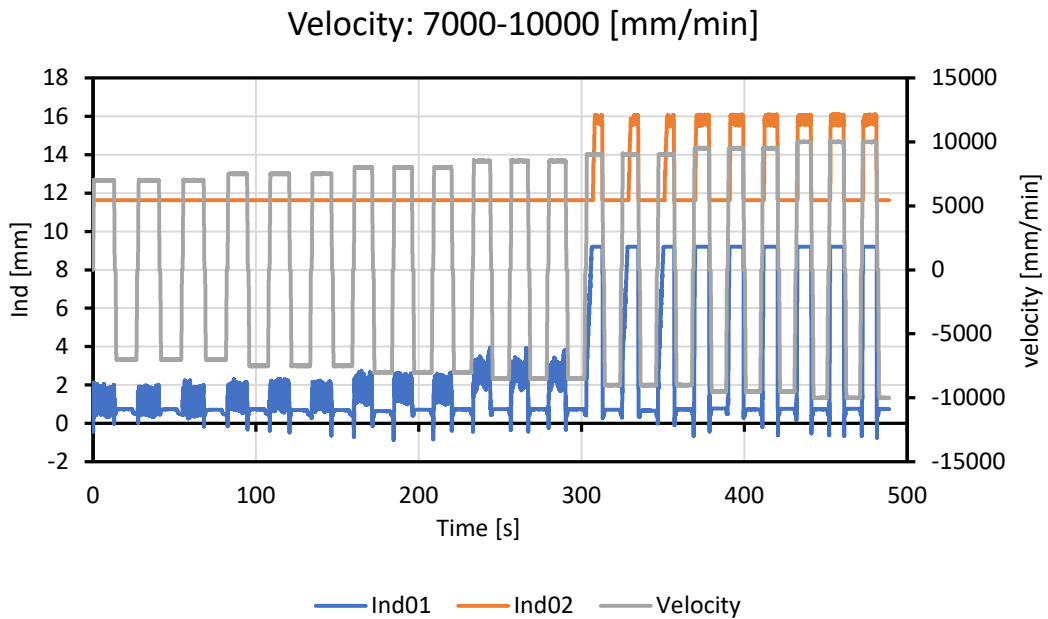


Figure 31: Sensor Output Converted Example

The tests are conducted with a wide variety of pumping velocities and discharge pressures. Furthermore, two different ball weights and velocity profiles are tested. A measurement of the flow rate is also conducted. The tests are done in a vertical position of the pump, there is no presence of gas, any temperature changes are neglected, and the only fluid tested is water. For each variety of pumping velocities and discharge pressures, several strokes are performed.

Both balls tested have the same diameter, 42,85 [mm]. The only difference is their weight. The light ball weighs 372,70 [g], and the heavy ball 576,93 [g]. The tests are conducted to examine the relationship between the opening state of the standing valve dependent on ball weight, plunger velocity, discharge pressure, and any combination of them.

4.1.1 Light Ball

The light ball is tested with two different cyclic velocity profiles, Trapezoid and Fourier Coefficient. Tests are done with discharge pressures ranging from 5.5 [bar] to 30 [bar]. Furthermore, the tested plunger velocities range from 1 [m/min] to 14 [m/min].

4.1.1.1 Cyclic Velocity Profile – Trapezoid

First, the results for a discharge pressure of 23.5 [bar] are discussed. Figure 32 shows the plunger velocity range from 7 [m/min] to 10 [m/min], with a stepwise increase of 0.5 [m/min]. Up to a velocity of 8.5 [m/min], the ball gets lifted just by a small amount. At 8.5 [m/min] the first meaningful opening of the valve happens. The valve fully opens at a velocity of 9 [m/min] indicated by the first spike of the orange line, representing the measured data of the inductive sensor 2 (Ind02). Any further increase in velocity does not affect the opening behavior of the standing valve anymore.

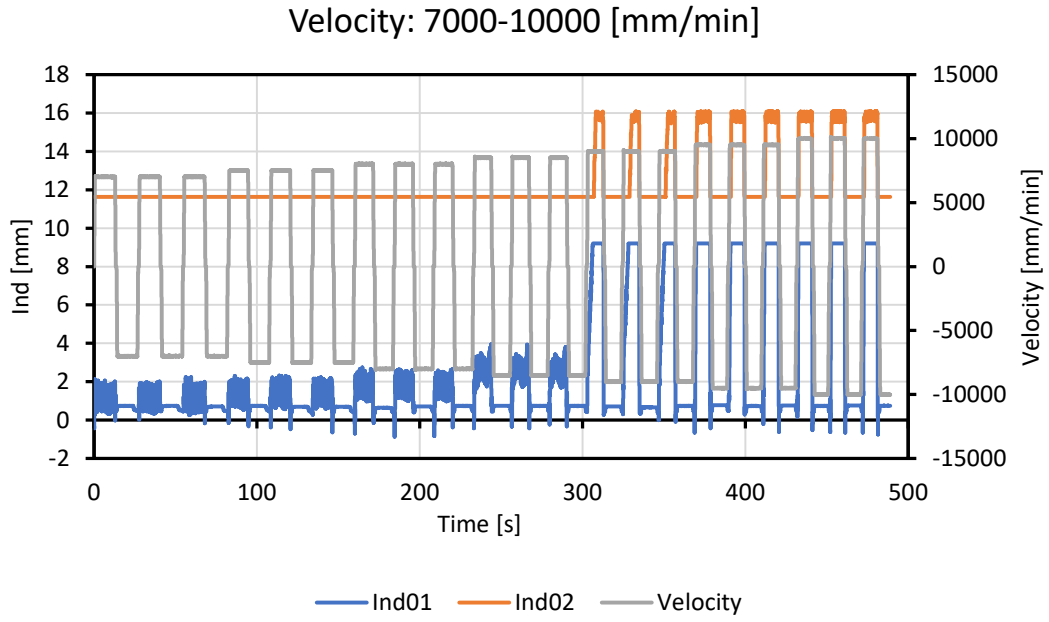


Figure 32: Light Ball Trapezoid, $p_{\text{discharge}}$ 23.5 [bar]

Figure 33 displays the valve's opening state. The percentage of ball movement is displayed against the plunger velocity [mm/min]. As previously stated, the ball lifts only a modest amount as the plunger velocity increases up to 8.5 [m/min]. The ball is then lifted rapidly until the valve is entirely open, the ball is at its highest position, at 9 [m/min].

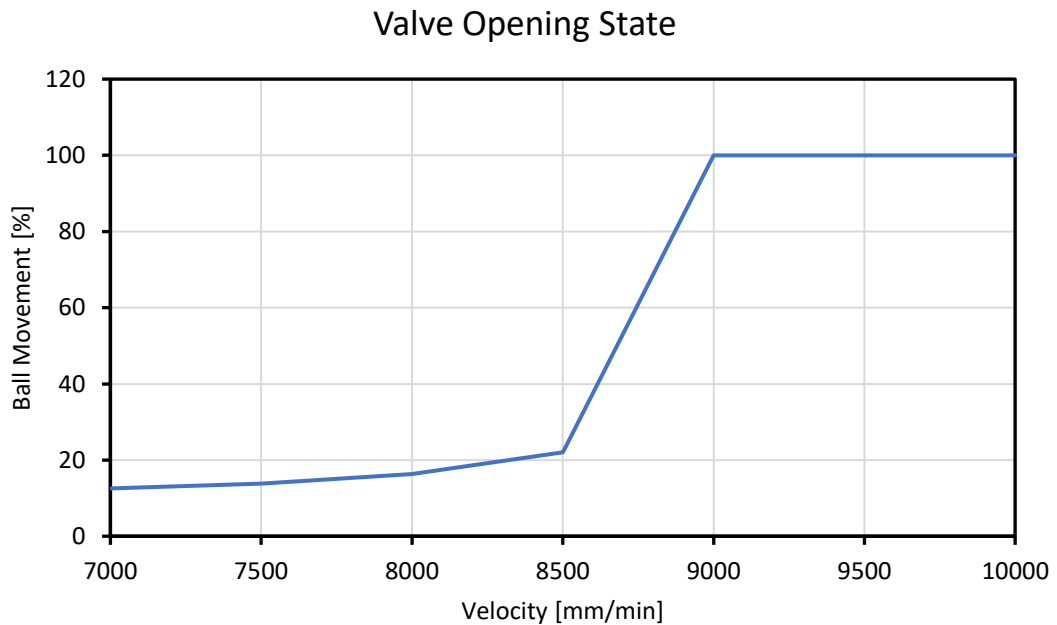


Figure 33: Light Ball Valve Opening State, Trapezoid, $p_{\text{discharge}}$ 23.5 [bar], Stepsize 0.5 [m/min]

A further experiment with the same discharge pressure is conducted. In this case, the step size increase of the plunger velocity is reduced to 0.2 [m/min] to capture more detail in the area where the valve changes its state from nearly closed to fully open (Figure 34).

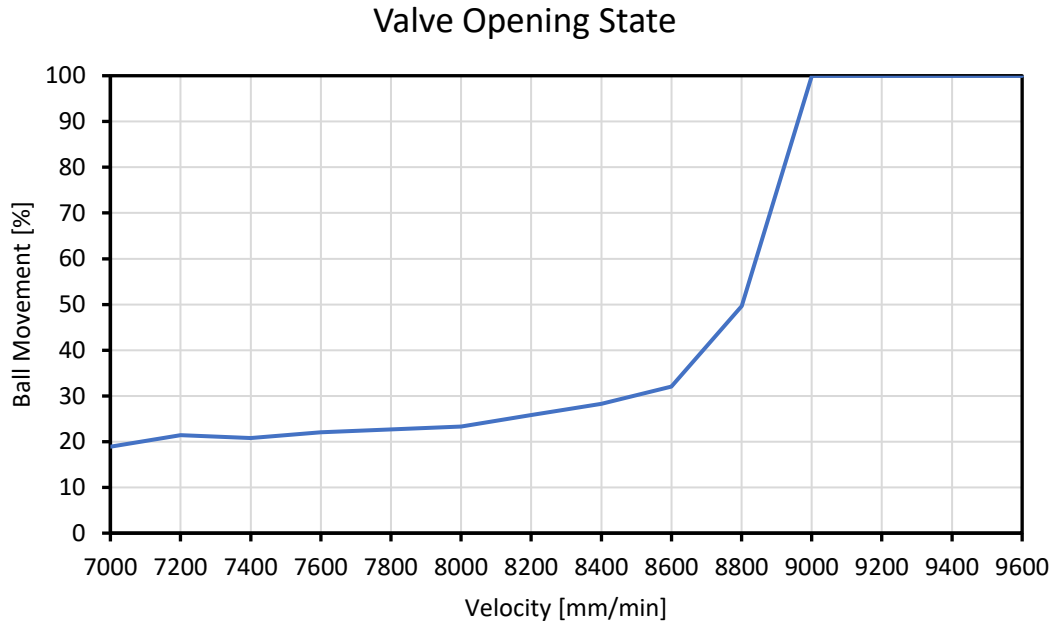


Figure 34: Light Ball Valve Opening State, Trapezoid, $p_{\text{discharge}}$ 23.5 [bar], Stepsize 0.2 [m/min]

It can be seen that the behavior of the valve opening is very similar in both measurements, the valve is fully open at a plunger velocity of 9 [m/min]. However, there is a slight discrepancy between the two curves below 9 [m/min]. This is due to the problems already mentioned before.

Second, the results for a discharge pressure of 5.5 [bar] are discussed. To capture additional information, the results are separated into two different plots. The results for a plunger velocity of 1 [m/min] to 6 [m/min] with a step size increase of 0.5 [m/min] are shown in Figure 35. Three pumping cycles with each velocity are conducted. The standing valve is almost closed up to a velocity of 6 [m/min], as shown. The spikes on the blue line primarily signify minor vertical and horizontal movements of the ball. The vertical orange lines are caused by bad signals from the upper inductive sensor (Ind02).

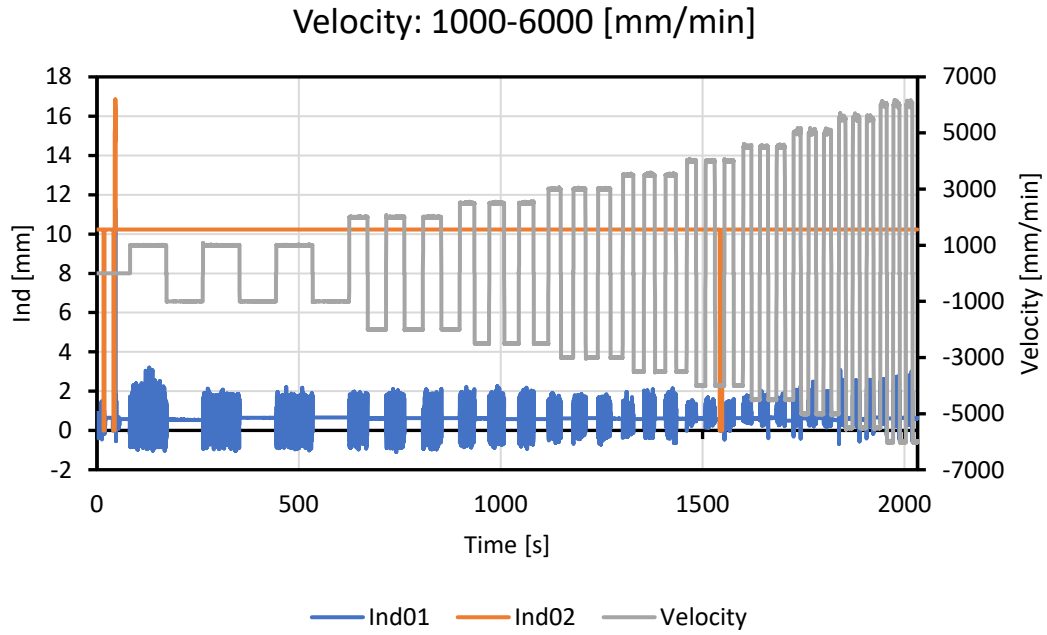


Figure 35: Light Ball Trapezoid, $p_{\text{discharge}} 5.5$ [bar], Part One

Figure 36 continues with a velocity ranging from 6.5 [m/min] up to 14 m/min] with a 0.5 [m/min] stepwise increase. The first meaningful lifting of the ball happens at a plunger velocity of 8 [m/min]. The valve fully opens at 8.5 [m/min], and remains open till 14 [m/min].

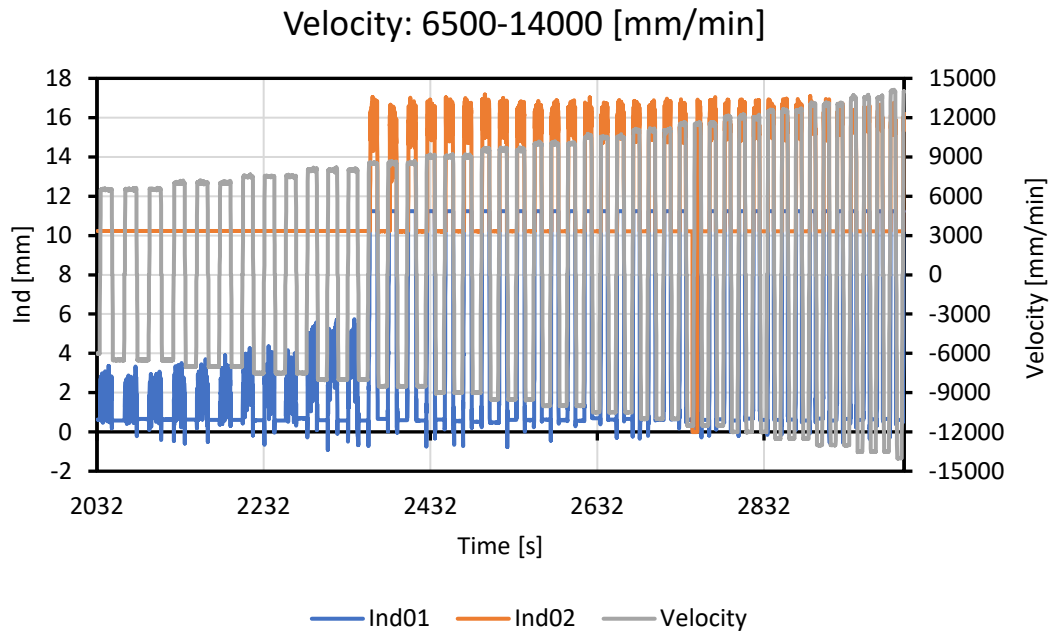


Figure 36: Light Ball Trapezoid, $p_{\text{discharge}} 5.5$ [bar], Part Two

The valve opening state with a discharge pressure of 5.5 [bar] is shown in Figure 37. As previously stated, the valve opens in a rather fast manner. The first visible lifting of the ball happens at a plunger velocity of 8 [m/min]. The valve fully opens at a velocity of 8.5 [m/min] and stays open till 14 [m/min].

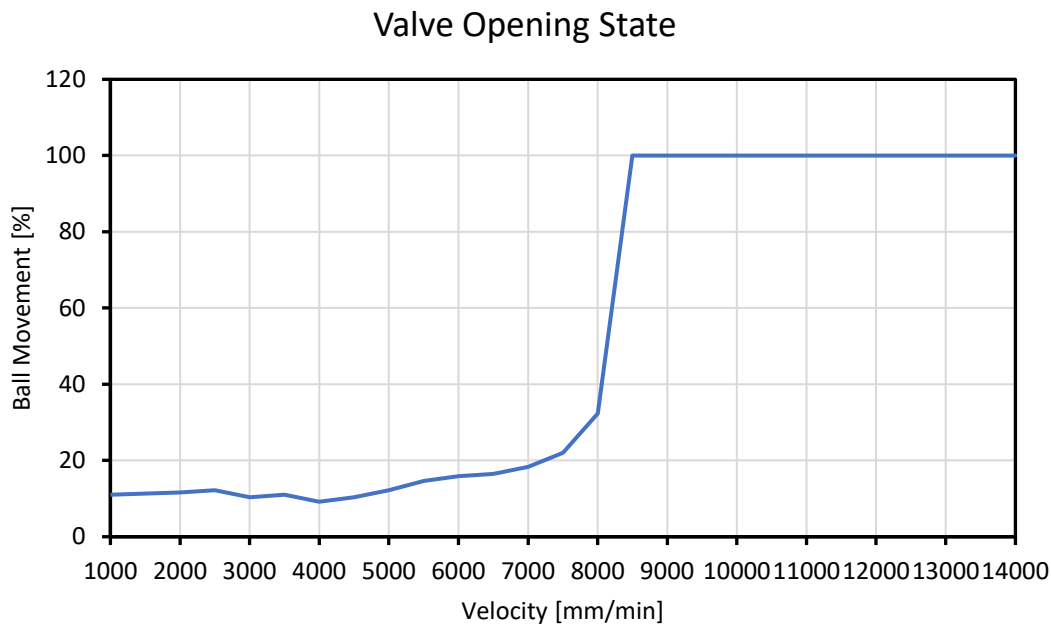


Figure 37: Light Ball Valve Opening State, Trapezoid, $p_{\text{discharge}} 5.5$ [bar]

The results at a discharge pressure of 30 [bar] are discussed in the third section. Since the plunger velocity at which the standing valve fully opens is the subject of this experiment, only a limited number of velocities are tested. Five pumping cycles are performed for each velocity. From left to right, Figure 38 displays a velocity of 9 [m/min], 8.8 [m/min], 9.2 [m/min], 9.4 [m/min], and 9.6 [m/min]. The valve opening is not the same for each of the five pumping cycles at a velocity of 8.8 [m/min]. This is due to a fluctuating pump intake pressure, that is provided in a discontinuous manner by a compressor. The valve fully opens at a plunger velocity of 9 [m/min].

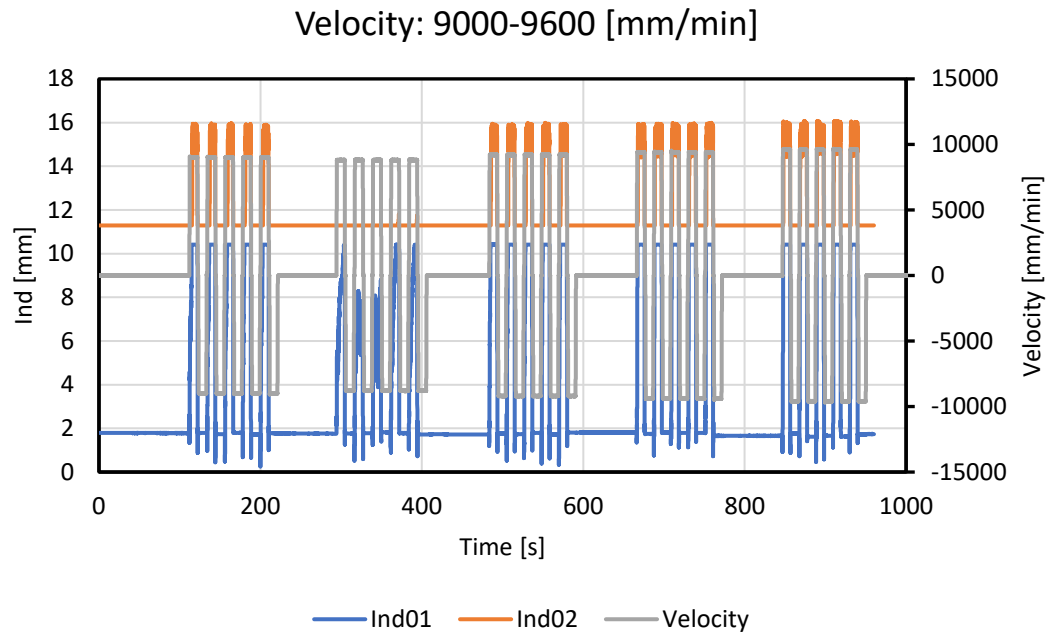


Figure 38: Light Ball Trapezoid, $p_{\text{discharge}}$ 30 [bar]

4.1.1.2 Cyclic Velocity Profile – Fourier Coefficient

The phenomenon of mid-cycle valve closing is investigated using a cyclic velocity profile with Fourier Coefficient. As previously mentioned, this can result in serious damage and a considerable reduction in the SRP's standing valve's lifetime. The blue line represents inductive sensor one (Ind01), the orange line represents inductive sensor two (Ind02), and the grey line represents plunger velocity (Figure 39). There is no signal of the ball of the standing valve in the sections where the blue or orange line stays horizontal.

With this velocity profile, the plunger is accelerated to 13.2 [m/min], then reduced to 7.5 [m/min] before returning to 13.2 [m/min]. The sharp dip in the blue line indicates that mid-cycle valve closing is present with these settings. This means the pressure is not sufficient enough to keep the valve open for the entire upstroke.

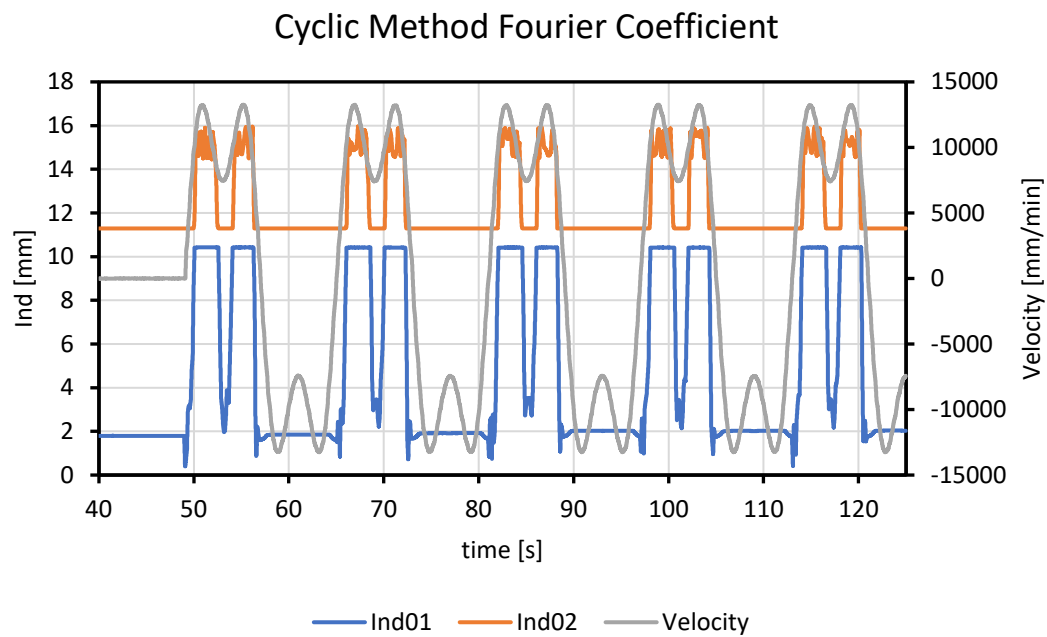


Figure 39: Light Ball Fourier Coefficient

4.1.2 Heavy Ball

Only one cyclic velocity profile, Trapezoid, is used to test the heavy ball. Plunger velocities range from 9 [m/min] to 13.5 [m/min]. The effect of discharge pressure on the valve's opening behavior is also investigated. Therefore, discharge pressures ranging from 15 [bar] to 30 [bar], at a constant velocity of 11.5 [m/min], are examined.

First, the results at a discharge pressure of 23.5 [bar] are discussed (Figure 40). At a plunger velocity of 11 [m/min], the ball is lifted for the first time considerably. The standing valve is fully open at a velocity of 11.5 [m/min]. However, this does not happen during the first pumping cycle. This is due to the previously mentioned variations in intake and discharge pressures.

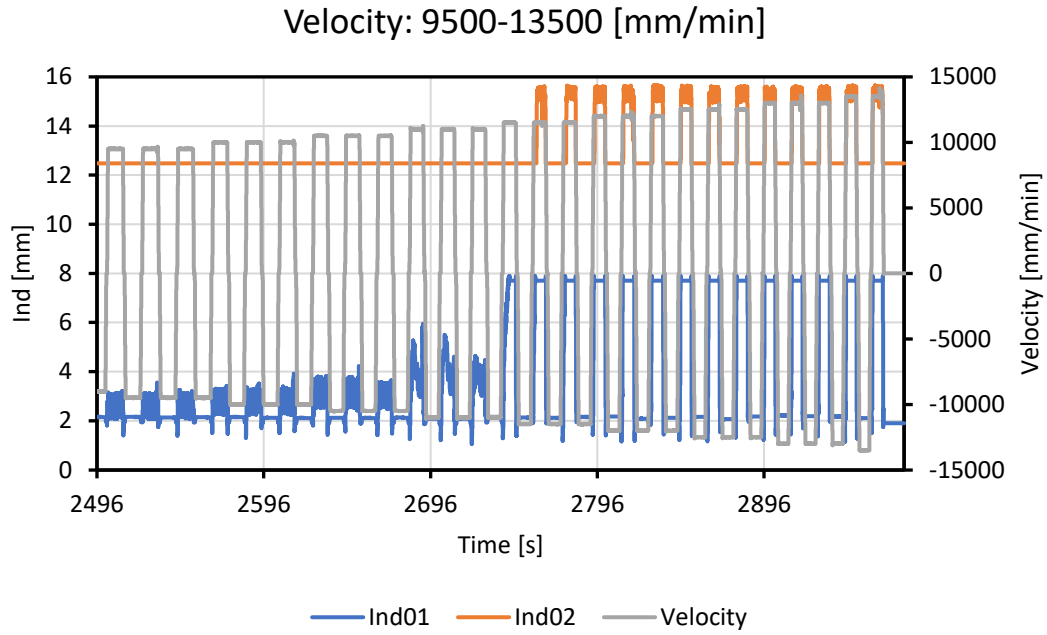


Figure 40: Heavy Ball Trapezoid, $p_{\text{discharge}}$ 23.5 [bar]

At a discharge pressure of 23.5 [bar], Figure 41 depicts the valve opening state for the heavy ball. The heavy ball's opening behavior is very similar to the light ball's. At a plunger velocity of 11 [m/min], the ball is lifted for the first time considerably. At 11.5 [m/min], the standing valve is fully open.

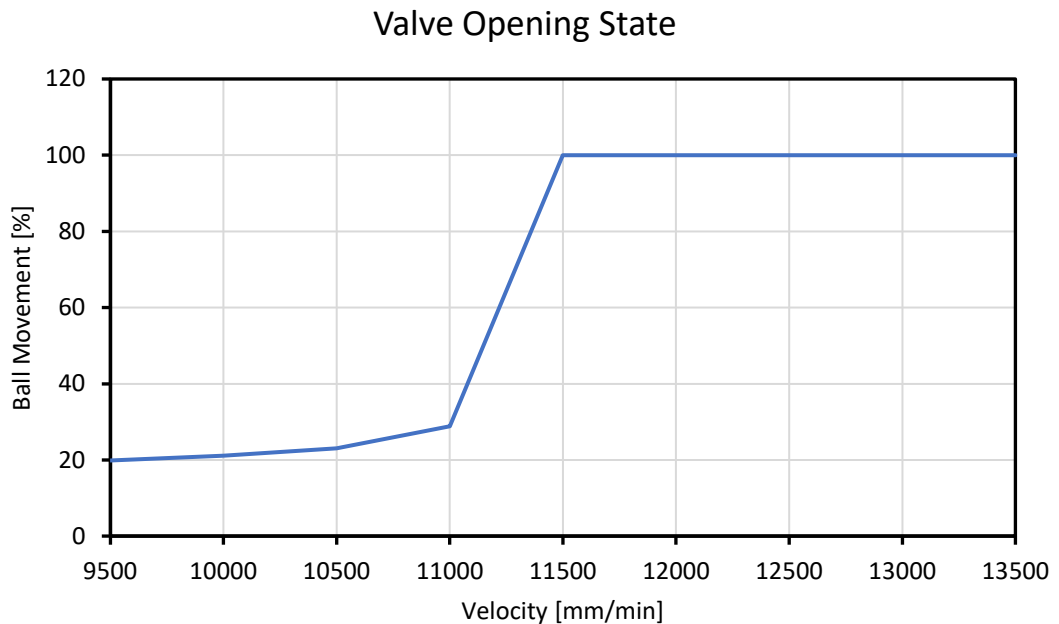


Figure 41: Heavy Ball Valve Opening State, Trapezoid, $p_{\text{discharge}}$ 23.5 [bar]

Next, the results for a discharge pressure of 5.5 [bar] are discussed (Figure 42). With increasing plunger velocity, the valve opens stepwise. The valve's critical velocity, or the velocity at which it fully opens, is 11 [m/min]. A further increase in velocity does not affect the valve's opening behavior.

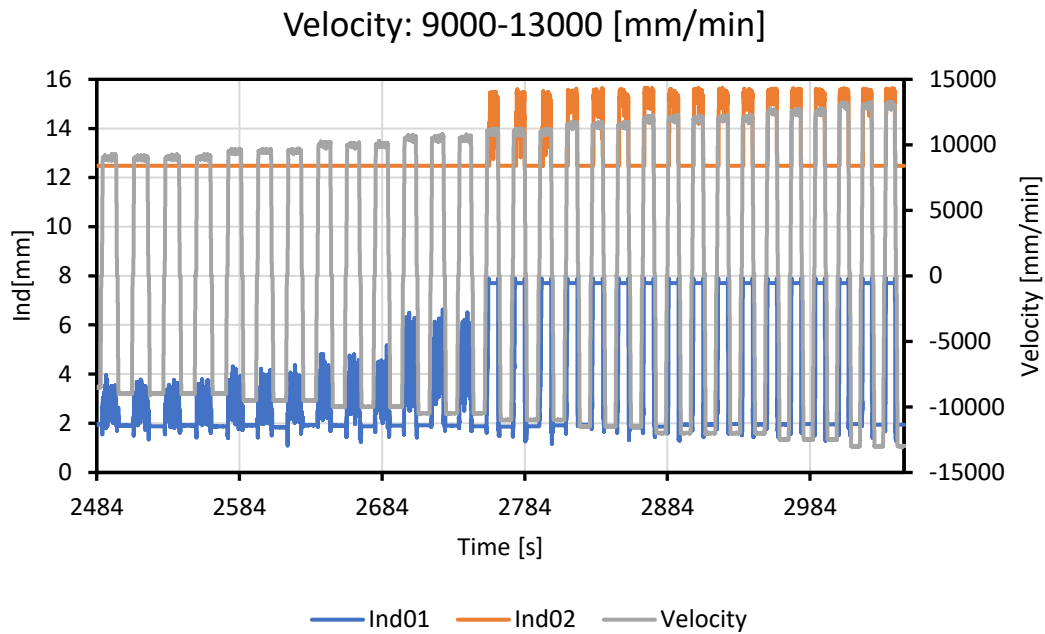


Figure 42: Heavy Ball Trapezoid, $p_{\text{discharge}} 5.5$ [bar]

Figure 43 shows the valve opening state. As seen before, the valve opens in a rather sharp manner.

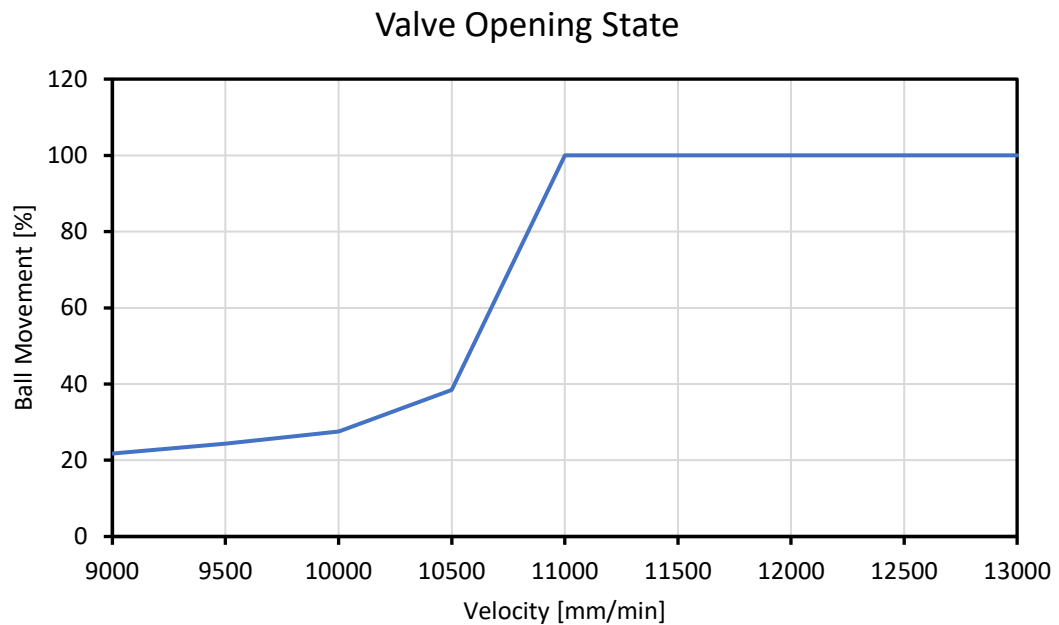


Figure 43: Heavy Ball Valve Opening State, Trapezoid, $p_{\text{discharge}} 5.5$ [bar]

The effect of discharge pressure at a constant plunger velocity is investigated in the last section. The valve's opening behavior is tested at 11.5 [m/min] plunger velocity and discharge pressures of 15 [bar], 20 [bar], 23.5 [bar], 25 [bar], 27 [bar], and 30 [bar]. A further increase in discharge pressure is not acceptable due to the plexiglass standing valve housing's structural limitations. The only thing that changes up to a discharge pressure of 27 [bar] is the duration the standing valve remains fully open. At 30 [bar] discharge pressure, the pressure is high enough to prevent the valve from fully opening at constant plunger velocity (Figures 44, 45, 46, 47, 48, 49).

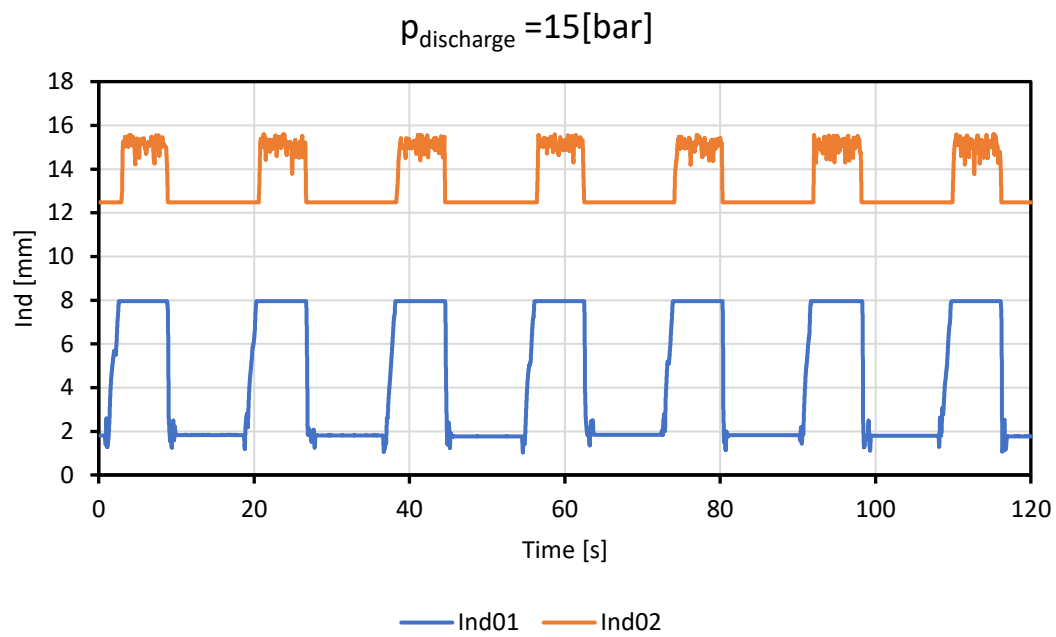


Figure 44: Effect of $p_{\text{discharge}}$, Heavy Ball Trapezoid, $p_{\text{discharge}} 15 [\text{bar}]$

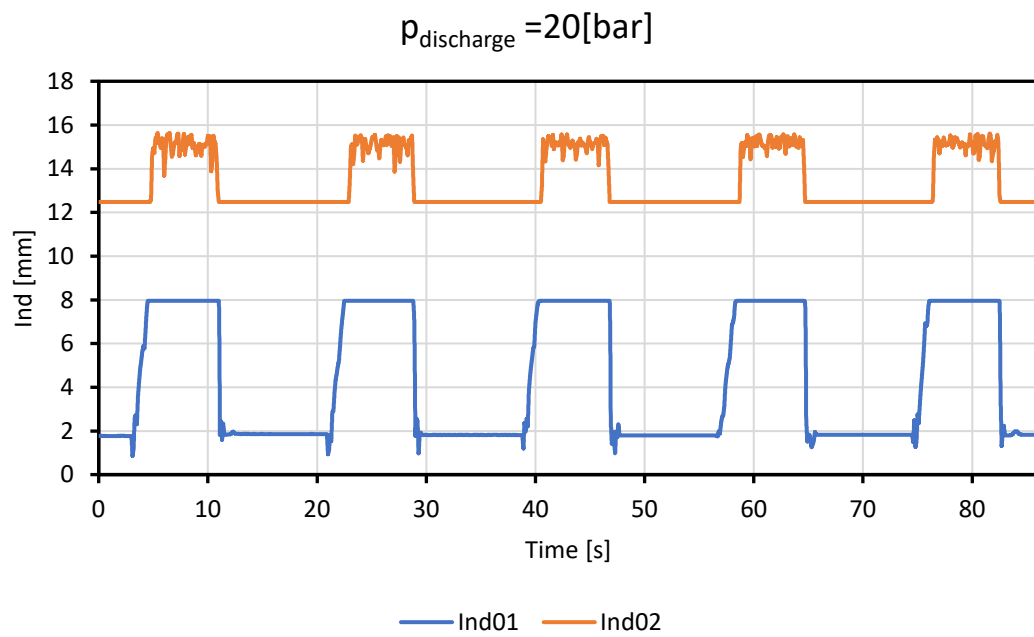


Figure 45: Effect of $p_{\text{discharge}}$, Heavy Ball Trapezoid, $p_{\text{discharge}} 20 [\text{bar}]$

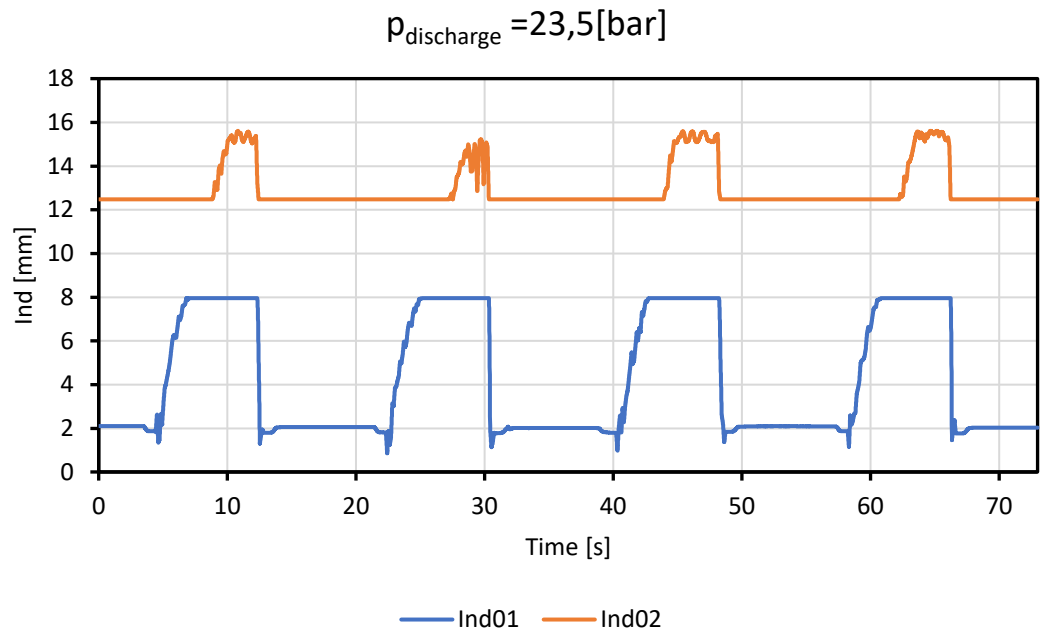


Figure 46: Effect of $p_{\text{discharge}}$, Heavy Ball Trapezoid, $p_{\text{discharge}} 23.5 [\text{bar}]$

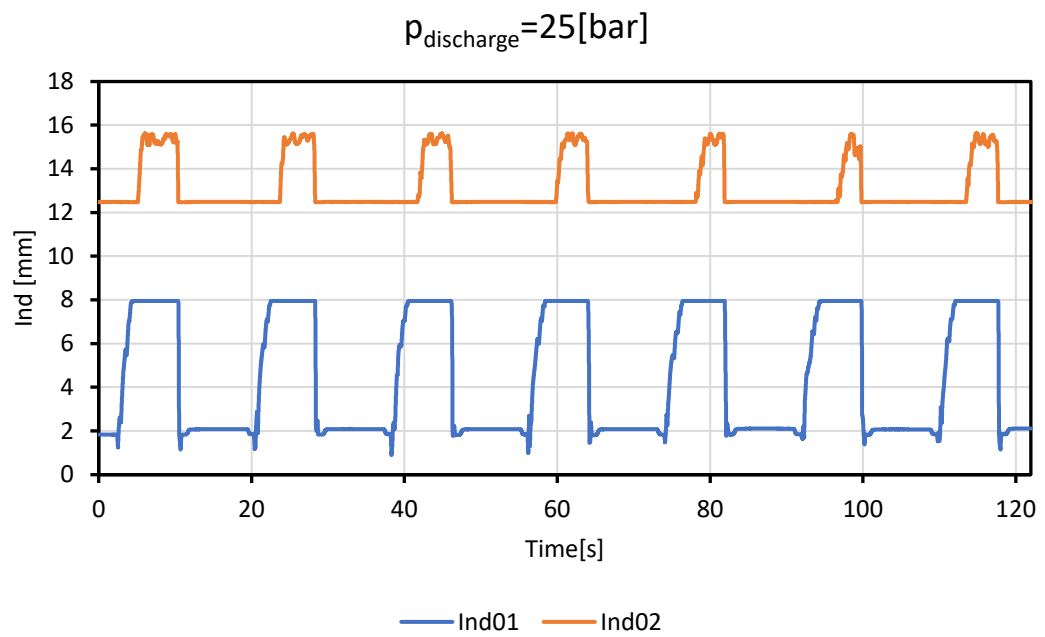


Figure 47: Effect of $p_{\text{discharge}}$, Heavy Ball Trapezoid, $p_{\text{discharge}} 23.5 [\text{bar}]$

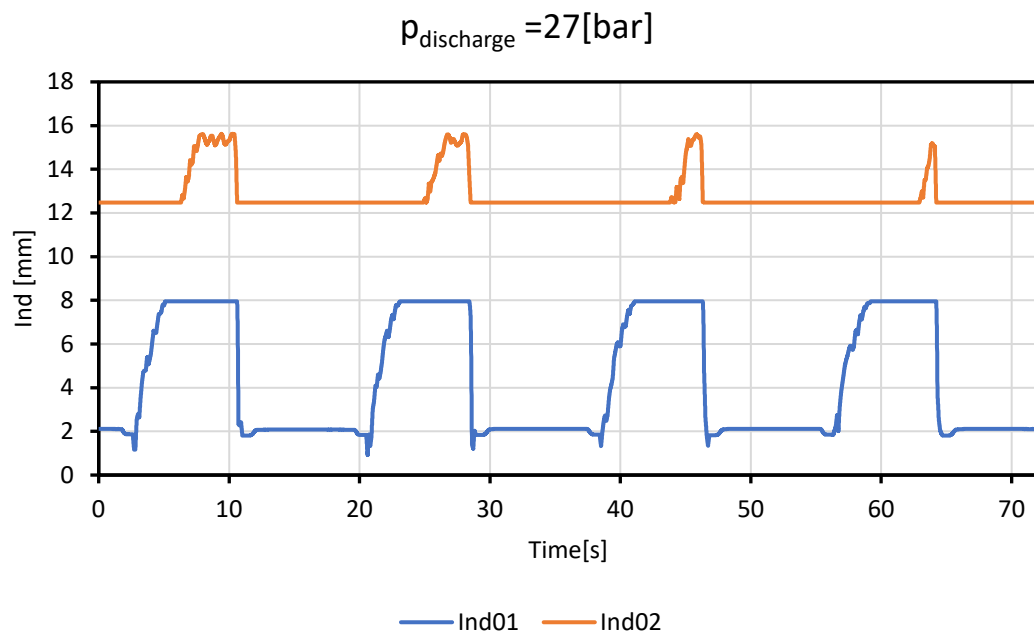


Figure 48: Effect of $p_{\text{discharge}}$, Heavy Ball Trapezoid, $p_{\text{discharge}} 27$ [bar]

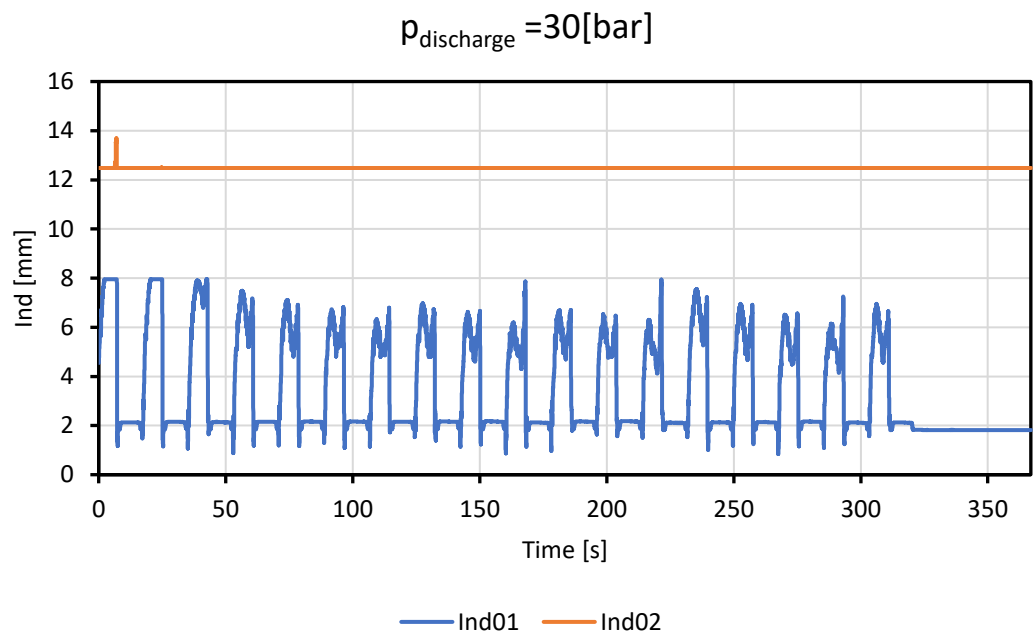


Figure 49: Effect of $p_{\text{discharge}}$, Heavy Ball Trapezoid, $p_{\text{discharge}} 30$ [bar]

4.1.3 Flow Rate Measurement

4.1.3.1 Light Ball

The flow rate for the light ball is measured at a discharge pressure of 23.5 [bar], with velocities ranging from 7 [m/min] to 9.6 [m/min] in 0.2 [m/min] increments. Furthermore, at a discharge pressure of 30 [bar], the flow rate is measured at plunger velocities ranging from 8.8 [m/min] to 9.6 [m/min] in 0.2 [m/min] increments.

Figure 50 depicts the increase in flow rate as the plunger velocity increases at a discharge pressure of 23.5 [bar]. The flow rate measurement is more quantitative rather than qualitative. This is due to the previously mentioned inaccuracies, such as fluctuating discharge and intake pressure and vibrations transmitted from the pump test facility to the load cell.

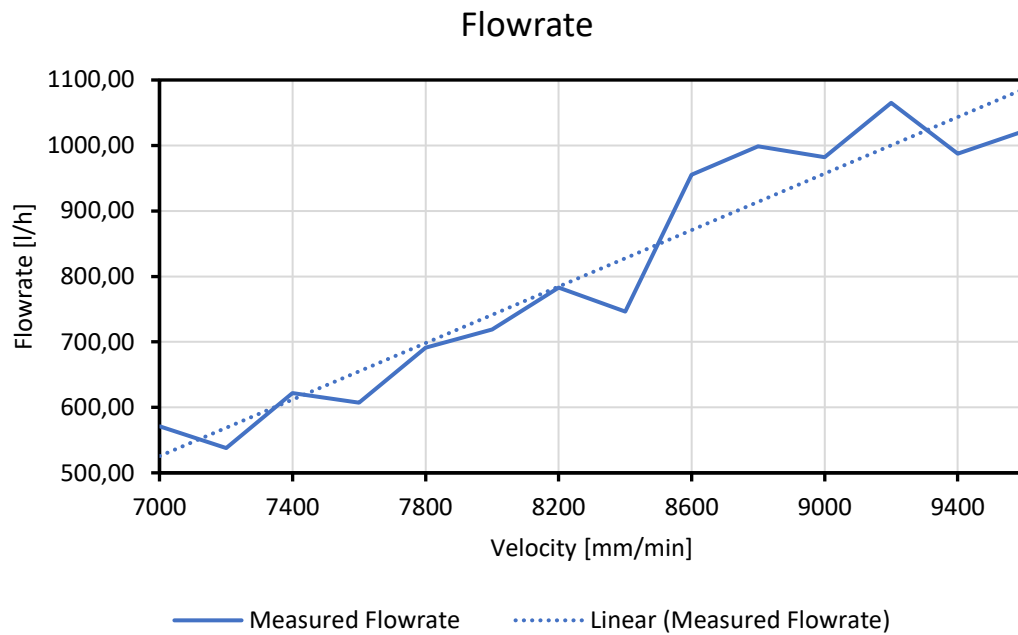


Figure 50: Light Ball Flow Rate Measurement, $p_{\text{discharge}} 23.5$ [bar]

Figure 51 shows the flow rate for a discharge pressure of 30 [bar] (). Although the flow rate tends to increase as plunger velocity increases, the measurement suffers from the previously mentioned problems.

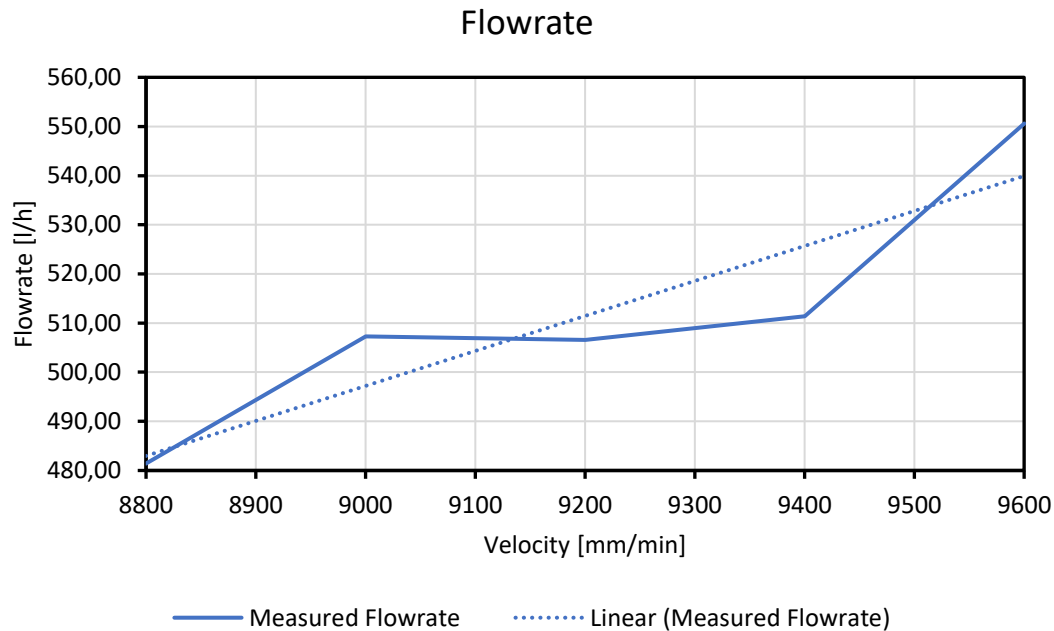


Figure 51: Light Ball Flow Rate Measurement, $p_{\text{discharge}} 30$ [bar]

4.1.3.2 Heavy Ball

The flow rate for the heavy ball is measured at discharge pressures of 8.5 [bar], 23.5 [bar], and 30 [bar] with plunger velocities of 11.5 [m/min] and 13 [m/min] each. The results are shown in Figure 52. In general, the flow rate decreases with increasing discharge pressure. However, there is a discrepancy with the flowrate measurement at a discharge pressure of 30 [bar]. The flow rate at a plunger velocity of 13 [m/min] for this discharge pressure is slightly too high, even higher than the respective flow rate for a discharge pressure of 23.5 [bar]. This is due to the previously mentioned problems and inaccuracies regarding the setup for the flow rate measurement.

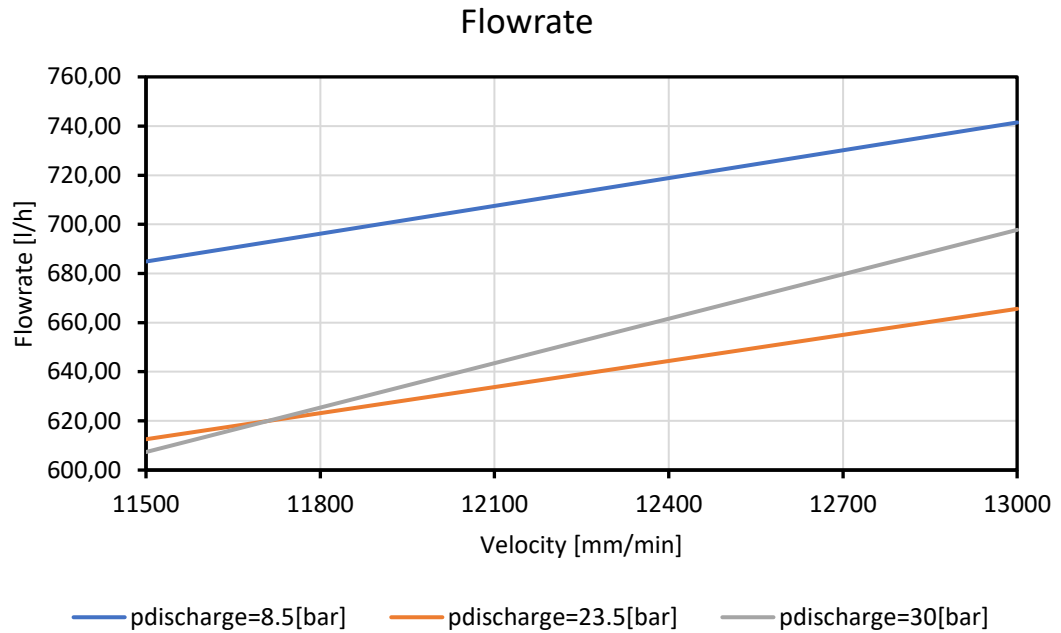


Figure 52: Heavy Ball Flow Rate Measurement, $p_{\text{discharge}}$ 8.5 [bar], 23.5 [bar], 30 [bar]

4.2 Discussion

4.2.1 Measurement Pump Test Facility

This section summarizes and contrasts all of the previous results.

At discharge pressures of 5.5 [bar] and 23.5 [bar], Table 3 compares the opening states of the light and heavy balls. The plunger velocity at which the standing valve is fully open is referred to as the opening state. For each ball weight, the difference in discharge pressure in the completely open condition of the standing valve is 0.5 [m/min]. Furthermore, at each discharge pressure, the difference in the opening state between the two ball weights is 2.5 [m/min].

Table 3: Valve Opening State Comparison

Opening State		
$p_{\text{discharge}}$ [bar]	Light Ball [m/min]	Heavy Ball [m/min]
5,5	8,5	11
23,5	9	11,5

The flow rates for the light ball at discharge pressures of 23.5 [bar] and 30 [bar] at velocities of 7 [m/min] to 9.6 [m/min] are summarized in Table 4.

Table 4: Light Ball Flow Rate Comparison

Flow Rate Light Ball		
	flow rate [l/h]	
	$p_{\text{discharge}}$ [bar]	
velocity [m/min]	23,5	30
7	571,36	
7,2	537,8	
7,4	621,72	
7,6	607,33	
7,8	691,17	
8	719,14	
8,2	782,87	
8,4	746,38	
8,6	954,89	
8,8	998,73	481,38
9	981,91	507,26
9,2	1064,73	506,6
9,4	987,35	511,37
9,6	1022,15	550,61

The flow rates for the heavy ball are shown in Table 5. The flow rates are measured at discharge pressures of 8.5 [bar], 23.5 [bar], and 30 [bar], at plunger velocities of 11.5 [m/min] and 13 [m/min].

Table 5: Heavy Ball Flow Rate Comparison

Flow Rate Heavy Ball			
	flowrate [l/h]		
	$p_{\text{discharge}}$ [bar]		
velocity [m/min]	8,5	23,5	30
11,5	684,93	612,5	607,36
13	741,5	665,59	697,71

4.2.2 Coupled Valve Sucker Rod Pump Model

As mentioned before, the results of the simulation show a discrepancy compared to the results of the simulation model. Model enhancement studies are conducted to further analyze and reduce this deviation. These MES include the implementation of a turbulence model, transverse oscillation, swirl flow, and slippage leakage. Indeed, the model enhancement studies lead to a better match between the two data sets reducing the gap (Figure 53). The test rig data shows a critical velocity of 9 [m/min] compared to the simulation data, without model enhancement

studies, of 11 [m/min]. But with the implementation of the model enhancement studies, the critical speed of the simulation is reduced to 10.5 [m/min].

$$\rho = 9 \text{ g/cm}^3, p_{dis} = 23.5 \text{ bar}$$

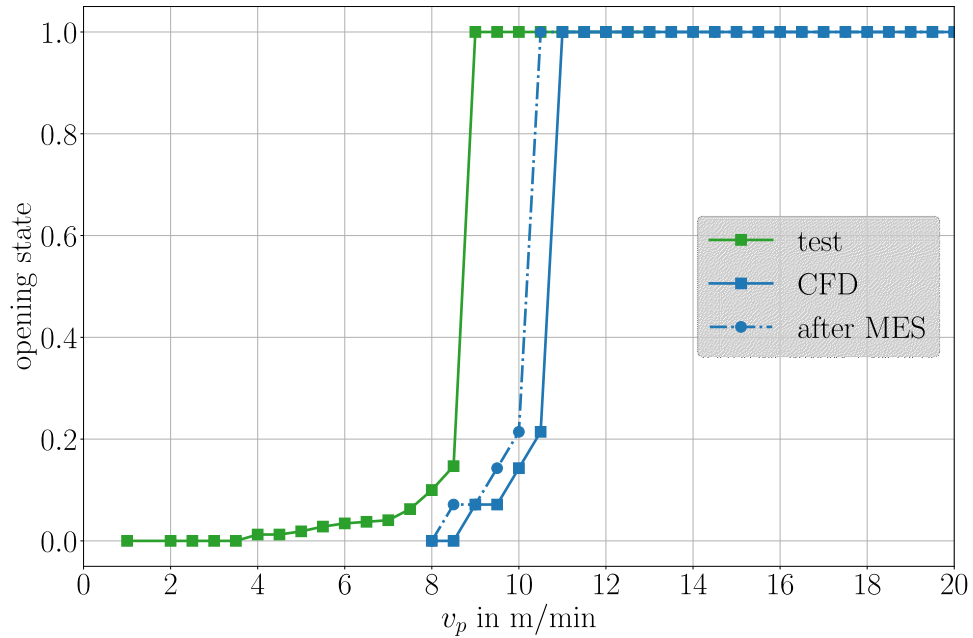


Figure 53: CV-SRP Model MES Comparison [21]

The variation of ball density shows a difference between the light and heavy ball of 2.5 [m/min] for the test rig data in terms of valve opening. The difference between the two ball weights for the simulation is 2.8 [m/min] (Figure 54).

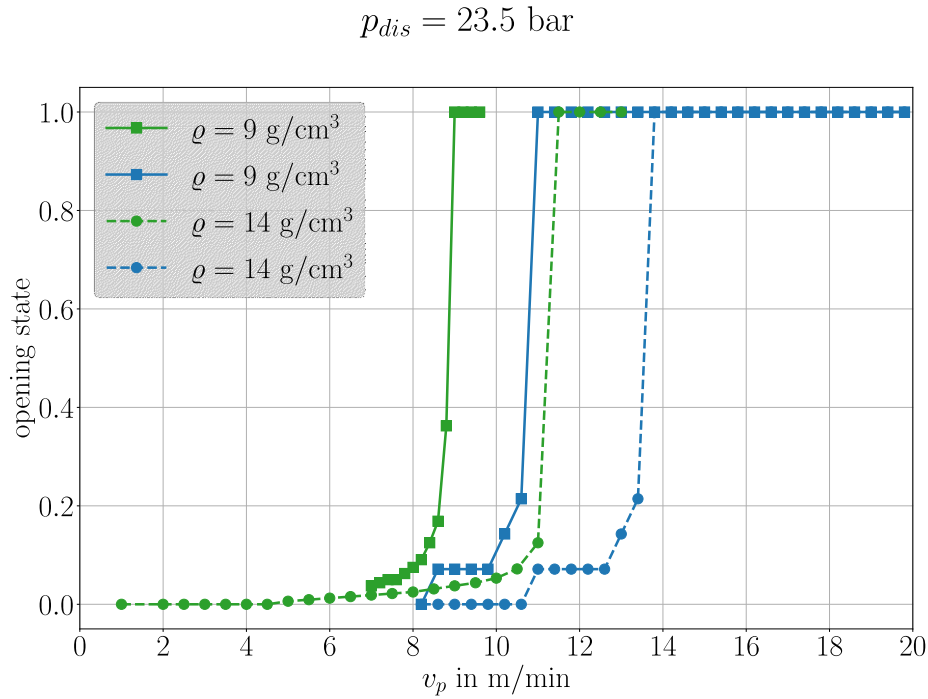


Figure 54: CV-SRP Model Effect of Ball Density [21]

In previous experiments, a valve cage with 5 holes is utilized compared to the valve cage with 4 holes used for the gathering of data for this thesis (Figure 55).

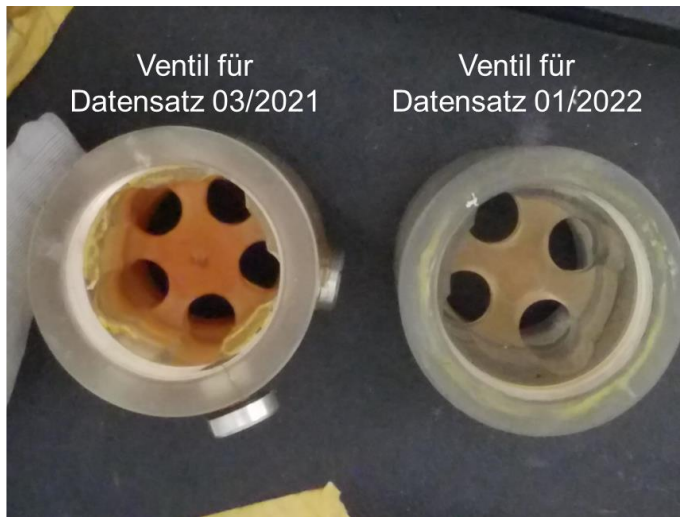


Figure 55: Valve Cage Comparison, 5 Holes (left) and 4 Holes (right) [21]

The simulation model predicts a similar increase in the critical speed as the test rig data from 4 holes to 5. The test rig data shows a difference of 4 [m/min], and the simulation model 3.5 [m/min].

The dashed green line in Figure 56 represents the test rig results for the valve cage with 4 holes, and the full green line represents the test rig results for a valve cage with 5 holes.

$$\rho = 9 \text{ g/cm}^3, p_{dis} = 23.5 \text{ bar}$$

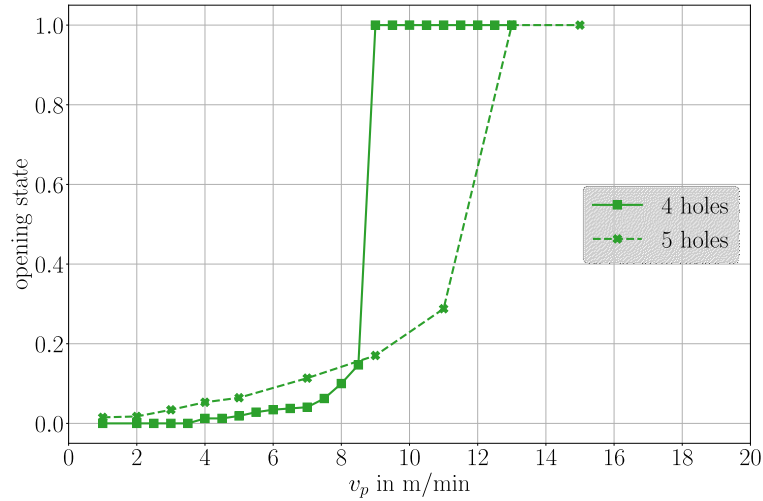


Figure 56: Test Rig Results Valve Cage Comparison [21]

Figure 57 shows the comparison between the test rig and simulation results for a valve cage with 5 holes. The green line represents the test rig and the blue line the simulation.

$$\rho = 9 \text{ g/cm}^3, p_{dis} = 23.5 \text{ bar}$$

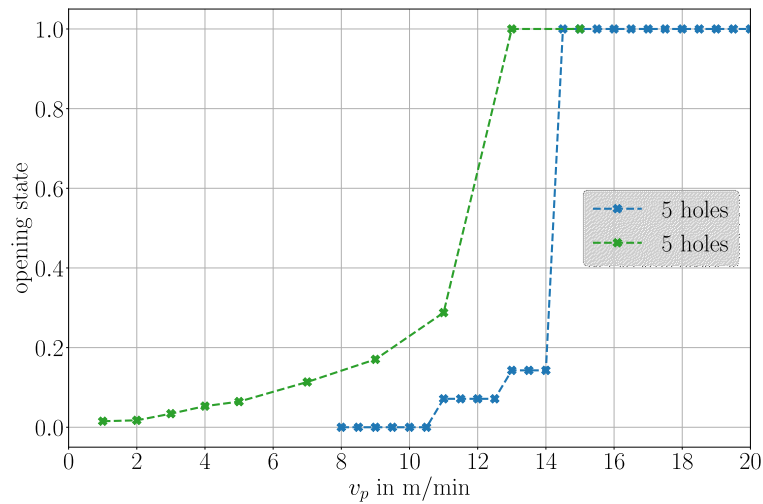


Figure 57: Test Rig and Simulation Results Comparison for Valve Cage with 5 Holes [21]

Table 6 provides a comparison between the test rig data and simulation data.

Table 6: Opening State Comparison Test Rig and Simulation

Comparison Test Rig and Simulation			
	$\Delta\rho_{\text{ball}}$: 9 and 14 [g/cm ³]	Geometry: 4 and 5 valve holes	$\Delta p_{\text{discharge}}$: 23.5 and 5 [bar]
velocity	[m/min]	[m/min]	[m/min]
Test rig	2,5	4	0,5
3D model	2,8	3,5	0,6

The simulation shows that the critical plunger speed has a square-root dependency on the ball density. Figure 58 shows that the simulations agree with the results of the simulation model. However, there is still a shift in the curve compared to the test rig data because of the 2[m/min] discrepancy of the critical plunger speed.

$$N_{omv} = \frac{8}{3} \frac{gr_b}{\rho_f} \left(\frac{\rho_b}{V_p^2} \right) \quad (38)$$

where:

g = acceleration due to gravity, $\frac{m}{s^2}$

r_b = ball radius, m

ρ_f = fluid density, $\frac{kg}{m^3}$

ρ_b = ball density, $\frac{kg}{m^3}$

V_p = plunger velocity, $\frac{m}{s}$

[21]

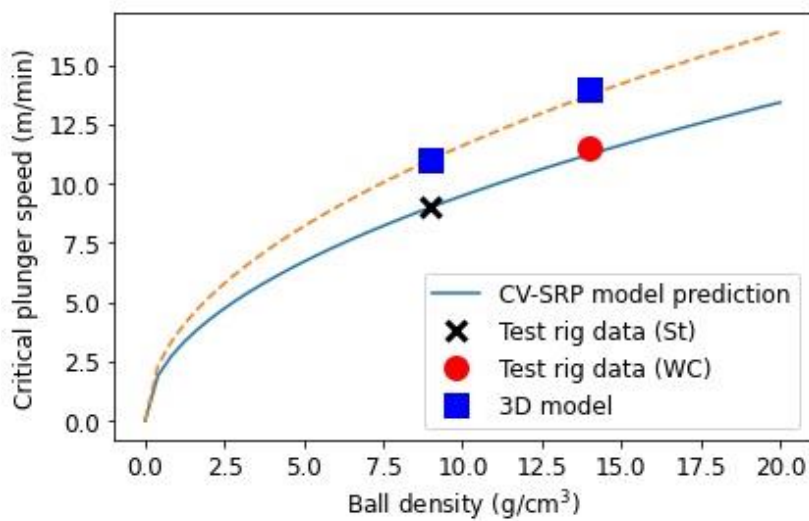


Figure 58: Square Root Dependency of Critical Plunger Speed [21]

The simulation model is capable of predicting the valve opening time. The simulation results agree reasonably well with those obtained from the test rig measurements (Figure 59). The comparison shown is at a plunger velocity of 9 [m/min], for both, the simulation and the test rig. In addition, the simulation can predict the valve opening time of any plunger velocity, represented by the green line.

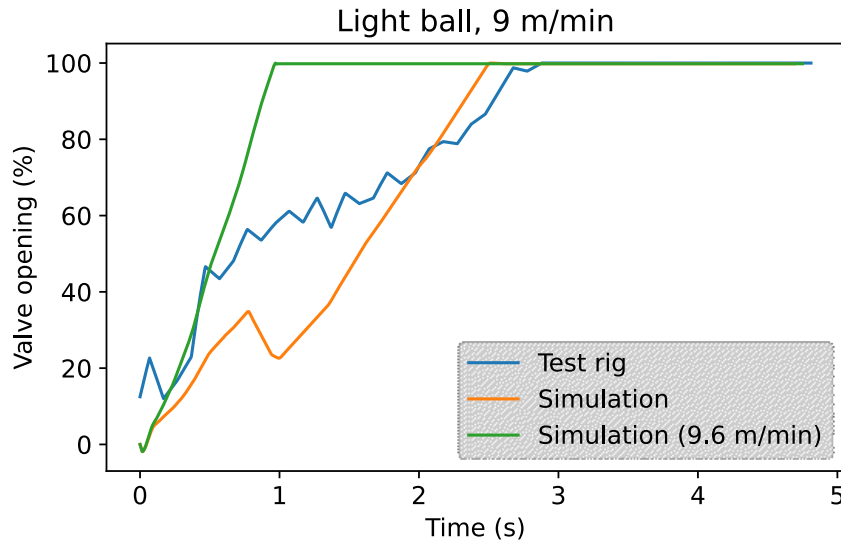


Figure 59: Valve Opening Time [21]

The CV-SRP model is capable of correctly predicting the phenomenon of mid-cycle valve closure. Therefore, an artificial pump card with fluctuations in the plunger velocity is generated. This pump card is applied to both, the test rig and the simulation. The results are shown in Figure 59.

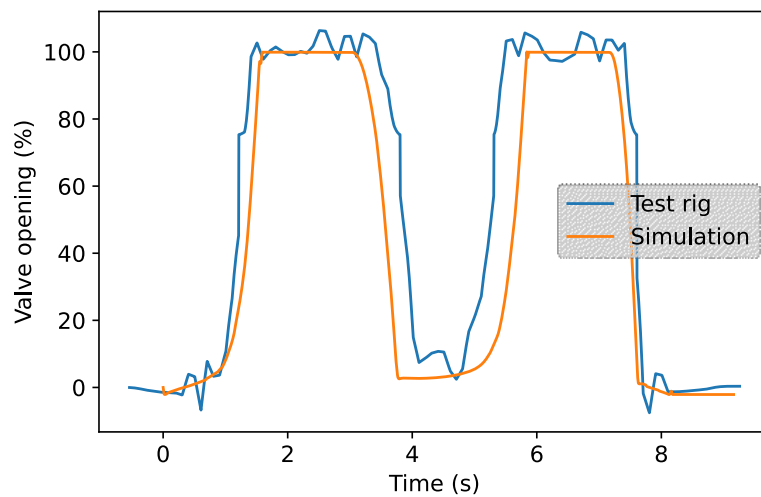


Figure 60: Mid-Cycle Valve Closure Test Rig and Simulation Comparison [21]

4.2.2.1 Summary Simulation Results

The CFD model, provided by AC2T research GmbH, is capable of predicting and capturing the behavior of the test rig, but a correction factor is needed to compensate for the difference in critical speed. The model can easily be adapted to different ball weights and valve cage geometries to generate the OMV number. The phenomenon of mid-cycle valve closure is correctly predicted by the simulation model. Furthermore, the square-root dependency of the critical plunger speed on the ball density can also be verified using the data from the pump test facility.

Chapter 5

Conclusion

5.1 Summary

One of the oldest and most extensively used artificial lift technologies are sucker rod pumps. Their actual downhole behavior, on the other hand, is difficult to predict or analyze. Field tests are expensive and have a limited range of adjustability. Test rig measurements can provide a solid foundation and additional insight into the downhole components' actual behavior.

The test results demonstrate the importance of a thorough investigation of the sucker rod pump standing valve. The standing valve's opening behavior is affected by a variety of mechanisms. Horizontal movement of the ball in the form of vibrations, ball rotation in an arbitrary direction, and mid-cycle valve closing are just a few examples. The phenomenon of mid-cycle valve closing, in particular, can cause significant valve seat and ball deterioration. The key to increasing the mean time between failure and maximizing profit is to understand and mitigate these effects.

Having a robust simulation capable of reproducing the real-world movement of a sucker rod pump's downhole components as well as real-world downhole conditions is a powerful tool for optimizing existing artificial lift systems or developing new production scenarios. The simulation is capable of accurately reproducing the standing valve ball's opening behavior, the valve opening time coincides relatively well with data from test rig measurements, and the phenomenon of mid-cycle valve closing also shows a good match. In conclusion, the combination of test rig measurements and simulation data provides detailed information on the actual downhole behavior of sucker rod pumps.

5.2 Future Work

All test rig measurements are conducted with a special Plexiglass standing valve cage. This cage does not comply with the API standards. Furthermore, all experiments are done with water only. Therefore, it is recommended to investigate the behavior of the sucker rod pump standing valve with a variety of valve cages that correspond to the API standard, and also with non-Newtonian fluids. This information can be used to enhance the capabilities of the CV-SRP model further. During the experiments, several issues and technical difficulties arose. The calibration is done manually, noise in the data is present, the inductive sensor's positioning led to a small area where neither of the two sensors could measure the actual position of the ball, and the flow measurement is more quantitative than qualitative. Therefore, it is recommended to implement an automated calibration system and a flow meter for the flow rate measurement. Furthermore, the implementation of API standard valve cages necessitates the implementation of different types of sensors to capture the position of the standing valve ball.

References

- [1] Takács G. Sucker-rod pumping handbook: Production engineering fundamentals and long-stroke rod pumping. Waltham, MA: Gulf Professional 2015.
- [2] Rod Pump Design: Available from: URL: <https://fddocuments.in/document/rod-pump-design.html> 2015 Nov 30.
- [3] Lyons WC, Plisga GJ. Standard handbook of petroleum & natural gas engineering. 2nd ed. Burlington MA, Oxford UK: Gulf Professional Pub 2005.
- [4] Robert P. Cutler and A.J. (Chip) Mansure. Fluid Dynamics in Sucker Rod Pumps: Sandia National Laboratories, Albuquerque, New Mexico.
- [5] Schlumberger. The Defining Series: Rod Pump Systems.
- [6] PetroWiki. PEH:Sucker-Rod Lift; 2020 [cited 2022 April 29] Available from: URL: https://petrowiki.spe.org/PEH:Sucker-Rod_Lift.
- [7] Fakher S, Khlaifat A, Hossain ME, Nameer H. A comprehensive review of sucker rod pumps' components, diagnostics, mathematical models, and common failures and mitigations. J Petrol Explor Prod Technol 2021; 11(10): 3815–39 [https://doi.org/10.1007/s13202-021-01270-7]
- [8] Downhole Diagnostic | Midland, TX. Sucker Rod Pumping Short Course 2014.
- [9] Andersson B. Computational fluid dynamics for engineers. Cambridge: Cambridge University Press 2012.
- [10] Sharma A. Introduction to Computational Fluid Dynamics: Development, Application and Analysis. 1. Aufl. s.l.: Wiley 2016.
- [11] Tu J, Yeoh GH, Liu C. Computational fluid dynamics: A practical approach. Third edition. Oxford, Cambridge MA: Butterworth-Heinemann 2018.
- [12] Moukalled F, Mangani L, Darwish M. The Finite Volume Method in Computational Fluid Dynamics. Cham: Springer International Publishing 2016.

- [13] Logan DL. A First Course in the Finite Element Method (MindTap Course List).
- [14] Finite Element Analysis with Error Estimators. Elsevier 2005.
- [15] Reddy JN, Gartling DK. The finite element method in heat transfer and fluid dynamics. 3. ed. Boca Raton: CRC Press 2010.
- [16] Souli M, Benson DJ. Arbitrary Lagrangian-Eulerian and fluid-structure interaction: Numerical simulation. London, Hoboken NJ: ISTE; Wiley 2010.
- [17] Sigrist J-F. Fluid-structure interaction: An introduction to finite element coupling. Chichester West Sussex United Kingdom: Wiley 2015.
- [18] Du WY. Resistive, Capacitive, Inductive, and Magnetic Sensor Technologies. CRC Press 2014.
- [19] Electrical Academia. Magnetomotive Force (MMF) Definition | Electrical Academia; 2017 [cited 2022 May 2] Available from: URL: <https://electricalacademia.com/electromagnetism/magnetomotive-force-mmf-definition-unit-formula/>.
- [20] White Star Pump Company. RSP-catalog. Cyrus Road Waller Texas.
- [21] M. Freudenberger, S. V. Jalikop, E. Badisch. Mathematical Description and Experimental Analysis of SRP Valve. Wr. Neustadt 2022 Feb 23.
- [22] Tabatabaian M. CFD module: Turbulent flow modeling. Dulles Virginia: Mercury Learning and Information 2015.
- [23] Encyclopedia Britannica. Magnus effect | Definition, Examples, & Facts; 2022 [cited 2022 May 2] Available from: URL: <https://www.britannica.com/science/Magnus-effect>.
- [24] O. Lynn Rowlan, James N. McCoy. Use of the Pump Slippage Equation to design pump clearances.

List of Figures

Figure 1: Number of Oil Well Installations and Total World's Share in Oil Production [1, pp. 4].....	15
Figure 2: Moderat-Capacity ALS Maximum Liquid Capacities [1, pp. 5]	16
Figure 3: Different ALS Approximate Efficiencies [1, pp. 6].....	17
Figure 4: SRP Basic Components [1, pp. 60].....	19
Figure 5: SRP Typical Wellhead Assembly [1, pp. 195]	21
Figure 6: Schematic Description of the Pumping Cycle	23
Figure 7: Heavy Wall Barrel with Pin End (left) and Thin Wall Barrel with Box End (right) 24	
Figure 8: Pin End Plain Metal Plunger (left) and Box End Grooved Metal Plunger (right) ...	25
Figure 9: Tubing Pump Basic Components [1, pp. 64].....	26
Figure 10: Rod Pump Basic Components [1, pp. 64].....	26
Figure 11: Valve Seat and Ball.....	27
Figure 12: Standing Valve Open API Cage [1, pp. 80].....	28
Figure 13: Standing Valve Closed API Cage [1, pp. 81]	29
Figure 14: Traveling Valve Open API Cage [1, pp. 81]	29
Figure 15: Traveling Valve Closed API Cage [1, pp. 82].....	30
Figure 16: Valve Cage HIVAC [1, pp. 82]	31
Figure 17: Dynamometer Card Explanation [8]	37
Figure 18: Cycles of Pump Card [8]	37
Figure 19: Steps of CFD Simulation [9, pp. 5].....	48
Figure 20: Eulerian, Lagrangian and Arbitrary Langrangian-Eulerian Formulations [17, pp. 16]	53
Figure 21: Inductor Types	55
Figure 22: Adjustable Inductor (a) and Variable Inductor (b).....	55
Figure 23: Self-Contained Inductive Sensor Basic Structure [18, pp. 179]	61
Figure 24: Valve Housing Plexiglass.....	68
Figure 25: Flow Rate Measurement Setup (left) and Load Cell with Tank (right)	68
Figure 26: Flow Rate Measurement Example	69
Figure 27: Valve Housing Plexiglass Calibration.....	70
Figure 28: Calibration Result Example	73
Figure 29: Calibration Polynomial Match Example	74
Figure 30: Sensor Output Unedited Example	75
Figure 31: Sensor Output Converted Example	75
Figure 32: Light Ball Trapezoid, $p_{\text{discharge}} 23.5$ [bar]	77
Figure 33: Light Ball Valve Opening State, Trapezoid, $p_{\text{discharge}} 23.5$ [bar], Stepsize 0.5 [m/min]	77
Figure 34: Light Ball Valve Opening State, Trapezoid, $p_{\text{discharge}} 23.5$ [bar], Stepsize 0.2 [m/min]	78
Figure 35: Light Ball Trapezoid, $p_{\text{discharge}} 5.5$ [bar], Part One.....	79
Figure 36: Light Ball Trapezoid, $p_{\text{discharge}} 5.5$ [bar], Part Two	79
Figure 37: Light Ball Valve Opening State, Trapezoid, $p_{\text{discharge}} 5.5$ [bar]	80
Figure 38: Light Ball Trapezoid, $p_{\text{discharge}} 30$ [bar].....	81
Figure 39: Light Ball Fourier Coefficient	82
Figure 40: Heavy Ball Trapezoid, $p_{\text{discharge}} 23.5$ [bar]	83
Figure 41: Heavy Ball Valve Opening State, Trapezoid, $p_{\text{discharge}} 23.5$ [bar].....	83
Figure 42: Heavy Ball Trapezoid, $p_{\text{discharge}} 5.5$ [bar]	84
Figure 43: Heavy Ball Valve Opening State, Trapezoid, $p_{\text{discharge}} 5.5$ [bar].....	85
Figure 44: Effect of $p_{\text{discharge}}$, Heavy Ball Trapezoid, $p_{\text{discharge}} 15$ [bar].....	86
Figure 45: Effect of $p_{\text{discharge}}$, Heavy Ball Trapezoid, $p_{\text{discharge}} 20$ [bar].....	86
Figure 46: Effect of $p_{\text{discharge}}$, Heavy Ball Trapezoid, $p_{\text{discharge}} 23.5$ [bar].....	87
Figure 47: Effect of $p_{\text{discharge}}$, Heavy Ball Trapezoid, $p_{\text{discharge}} 23.5$ [bar].....	87

Figure 48: Effect of $p_{\text{discharge}}$, Heavy Ball Trapezoid, $p_{\text{discharge}}$ 27 [bar]	88
Figure 49: Effect of $p_{\text{discharge}}$, Heavy Ball Trapezoid, $p_{\text{discharge}}$ 30 [bar]	88
Figure 50: Light Ball Flow Rate Measurement, $p_{\text{discharge}}$ 23.5 [bar].....	89
Figure 51: Light Ball Flow Rate Measurement, $p_{\text{discharge}}$ 30 [bar]	90
Figure 52: Heavy Ball Flow Rate Measurement, $p_{\text{discharge}}$ 8.5 [bar], 23.5 [bar], 30 [bar].....	91
Figure 53: CV-SRP Model MES Comparison [21].....	93
Figure 54: CV-SRP Model Effect of Ball Density [21].....	94
Figure 55: Valve Cage Comparison, 5 Holes (left) and 4 Holes (right) [21].....	94
Figure 56: Test Rig Results Valve Cage Comparison [21].....	95
Figure 57: Test Rig and Simulation Results Comparison for Valve Cage with 5 Holes [21]..	95
Figure 58: Square Root Dependency of Critical Plunger Speed [21].....	96
Figure 59: Valve Opening Time [21]	97
Figure 60: Mid-Cycle Valve Closure Test Rig and Simulation Comparison [21]	97

List of Tables

Table 1: Nominal Tubing Size API Spec 11AX [1, pp. 70].....	33
Table 2: Pump Bore Size API Spec 11AX [1, pp. 71].....	33
Table 3: Valve Opening State Comparison.....	91
Table 4: Light Ball Flow Rate Comparison.....	92
Table 5: Heavy Ball Flow Rate Comparison.....	92

Abbreviations

ALS	Artificial Lift System
SRP	Sucker Rod Pump
ESP	Electric Submersible Pump
PCP	Progressive Cavity Pump
CV-SRP	Coupled-Valve Sucker Rod Pump
API	American Petroleum Institute
HIVAC	High Volume and Compression Cage
POC	Pump Off Controller
API RP	API Recommended Practice
PTF	Pump Test Facility
CFD	Computational Fluid Dynamics
CAD	Computer-Aided Design
ALE	Arbitrary Lagrangian-Eulerian
RCIM	Resistive, Capacitive, Inductive, Magnetic
AC	Alternating Current
OMV number	Optimum Valve number
RANS	Reynolds-Averaged Navier-Stokes
Ind01	Inductive Sensor 01
Ind02	Inductive Sensor 02